DIRECTIONAL LIGHT EMISSION AND ABSORPTION BY SEMICONDUCTOR NANOWIRES

Grzegorz Grzela

The cover image is a photograph of light diffracted by semiconductor nanowires arranged in an ordered array. This photograph was taken in a dark room while the nanowire array was being illuminated with a collimated beam of a supercontinuum white light source.

ISBN: 978-90-386-3420-3

A catalogue record is available from the Eindhoven University of Technology Library.

Directional light emission and absorption by semiconductor nanowires

PROEFSCHRIFT

ter verkrijging van de graad van doctor aan de
Technische Universiteit Eindhoven, op gezag van de
rector magnificus prof.dr.ir. C.J. van Duijn, voor een
commissie aangewezen door het College voor
Promoties, in het openbaar te verdedigen op
maandag 26 augustus 2013 om 16:00 uur

door

Grzegorz Grzela

geboren te Legnica, Polen

Dit proefschrift is goedgekeurd door de promotiecommissie:

voorzitter:	prof.dr.ir. G.M.W. Kroesen	
1^e promotor:	prof.dr. J. Gómez Rivas	
2^e promotor:	prof.dr. A. Polman	(Universiteit van Amsterdam)
leden:	prof.dr. E.P.A.M. Bakkers	(Technische Universiteit Delft)
	prof.dr. W.L. Vos	(Universiteit Twente)
	prof.dr.ir. M.K. Smit	
	dr. R.W. van der Heijden	
adviseur:	dr.hab. A. Fontcuberta i Morral	(École Polytechnique Fédérale de Lausanne)

This work is part of the research program of the "Stichting voor Fundamenteel Onderzoek der Materie (FOM)", which is financially supported by the "Nederlandse organisatie voor Wetenschappelijk Onderzoek (NWO)" and is part of an industrial partnership program between Philips and FOM.

The secret of getting ahead is getting started

Contents

CHAPTER 1

INTRODUCTION

1.1 Semiconductor nanowires

Light is certainly one of the most important phenomena in our daily lives. We constantly learn how to generate, manipulate and detect it. Light generation, manipulation and detection require using structures of different materials that have certain optical properties, such as transmittance, reflectance, emittance or absorbance. For windows we use materials that transmit light, whereas materials used for mirrors should rather reflect light. The optical properties of a structure depend on its geometry and the material of which it is made. Some structures can efficiently emit light and make good light sources or absorb light and convert it into electricity making good detectors or solar cells. If a structure gets small, such that its dimensions are comparable to the wavelength of light, the optical properties of such structure change. This change can be dramatic due to the resonant response of the structure to the frequency of light. Recent developments in nanofabrication techniques allowed manufacturing novel structures with unexplored optical properties. One of such novel structures are semiconductor nanowires, whose optical properties are the subject of this thesis.

Nanowires are anisotropic nanostructures often compared to circular cylinders whose length is many times longer than their diameters. The diameter varies between few nanometers to few hundreds of nanometers. The history of nanowires made of semiconductor materials started in Bell Labs in the early 1960s, when Wagner and Ellis fabricated the first silicon nanostructures of this kind (called nanowhiskers at that time) [1]. In the years that followed, these elongated nanostructures attracted increasing interest [2]. Besides silicon [3], other semiconductor materials of groups IV [4, 5], II/VI [6–9], and III/V were used to grow nanowires [10]. In 2002 Gudiksen et al. [11], and Björk et al. [12], who showed that segments of different materials can be grown in nanowires despite the different lattice mismatch of these materials. This demonstration opened a wide range of possibilities for the development of complex nanostructures formed by different materials. Heteroepitaxial growth is possible because the cross-sectional area of nanowires is small and strain caused by crystalline lattice mismatch of two materials cannot build up in the structure. Such combination of lattice-mismatched materials is impossible at the interface of large-area thin films, where lattice mismatch introduces defects that reduce the material quality. In 2004 Bakkers et al. [13], Khorenko et al. [14] and Mårtensson et al. [15] demonstrated that it is also possible to grow nanowires of one semiconductor material on top of a substrate of semiconductor that is lattice mismatched. In this way, nanowires made of expensive groups-III/V semiconductors can be grown on top of, e.g., cheap group-IV semiconductor substrates, which could enable the integration of nanowires in semiconductor industry.

The development of the nanofabrication techniques and the possibility of homo- and/or heteroepitaxy allowed introducing nanowire-based optoelectronic devices. In 2001 Duan et al. demonstrated that single electrically-contacted indium phosphide (InP) nanowires with a p-n junction grown along the nanowire axis can work as electronic transistors and light-emitting devices [10]. The nanowires also proved to be optical waveguides in which Fabry-Pérot modes gave rise to lasing as reported by Huang et al. in 2001 for zinc oxide (ZnO) nanowires [6]. These discoveries lead to the demonstration of electrically-driven nanowire lasers by Duan et al. in 2003 [7]. Further investigations of lasing in ZnO nanowires by van Vugt et al. lead to the conclusion that the laser emission is non-directional [16]. Heteroepitaxially wrapped-around multi-quantum wells were used by Qian et al. in 2008 to tune the lasing wavelength in nanowires [17]. Ordered, low density arrays of semiconductor nanowires can also work as quasi-two dimensional photonic crystal directional light emitters as demonstrated recently by Diedenhofen et al. [18] and Fontana et al. [19]. Furthermore, nanowires surrounded by a nanowire photonic crystal can exhibit lasing due to photonic crystal cavity resonance, as pointed out by Scofield et al. [20].

The fabrication of nanowires also allows the growth of luminescent quantum dots embedded in nanowires, as shown by Panev et al. in 2003 [21]. Later, Borgström et al. demonstrated that quantum dots embedded in nanowires can be optical sources emitting single photons [22]. These light sources are of great importance for future quantum computing, where computations will be based on quantum states of particles such as photons. These achievements have stimulated the use of nanowires as optical nanoantennas that could tailor the intensity, directionality and polarization of the spontaneous emission of quantum emitters embedded in nanowires [23]. The first semiconductor nanowire nanoantenna embedding a single-photon source has been demonstrated by Claudon et al. in 2010 [24]. In this work the single-photon emission was coupled to waveguide modes of the nanowire embedding the source. The mode was then adiabatically expelled from the nanowire to the far-field by introducing tapering to the otherwise cylindrical structure. Such structure emitted single photons into a small solid angle. It has been also reported that the coupling of the spontaneous emission to waveguide modes is sensitive to nanowire diameter [25], while the polarization of the emission can be controlled by engineering the nanowire cross section [26]. The emission of single-photon sources embedded in nanowires is being consequently improved [27, 28]. Recently, the first non-deterministic electrically-driven single-photon sources embedded in semiconductor nanowires have been demonstrated by Deshpande et al. [29].

Semiconductor nanowires have been also used for photovoltaic applications [30–34]. The first solar cells based on nanowires considered combining ensembles of inorganic nanowires with conductive polymers, as in the work of Huynh et al. [35]. Due to their large surface to volume ratio, nanowires were soon employed in dye-sensitized solar cells by Baxter et al. [36]. The first single-nanowire solar cell featuring an inorganic p-n junction in nanowires was reported by Tian et al. in 2007 [30]. Since then researchers have focused on understanding and optimizing light absorption mechanisms in nanowires. Due to their anisotropic geometry, single direct band gap semiconductor nanowires have shown polarized light emission and absorption, first reported by Wang et al. [37]. Nanowires illuminated from the direction perpendicular to their axis absorb more efficiently light with a polarization vector parallel to the axis than when the polarization is perpendicular to this axis. The experimental results were explained in the electrostatic limit valid only for infinitely thin wires. The polarization anisotropy of light emission and absorption by thicker wires was suggested to originate from Mie resonances supported by nanowires in the work of van Weert et al. [38]. This theory became popular when Cao et al. used it to describe the spectrally- and polarization-dependent light absorption in single nanowires [39, 40] and is commonly used for explaining the response of nanowires to light incident perpendicular to their axes [41].

Arrays of vertically-oriented nanowires have been demonstrated as efficient light absorbers, whose absorption can be tuned by modifying the nanowire geometry [42, 43]. Optical absorption in nanowires when light is incident from the direction parallel to their axes has been found to be of different nature than Mie resonances. Seo et al. studied reflectance of arrays or vertical silicon nanowires to find that the incident light coupled to guided modes supported by each individual nanowire [44]. Soon after, the same mechanism was found to be responsible for strong light absorption in indium arsenide nanowires [45]. The nanowire diameter is important for coupling the normally incident light to waveguide modes in nanowires for increasing the absorption [46, 47]. Based on this knowledge, Wallentin et al. reported a solar cell consisting of an array of optimized InP nanowires with a single p-n junction that achieved the record efficiency of 13.8% [48]. This device has delivered 83% of the photocurrent obtained in planar photovoltaic devices based on the same semiconductor [49, 50]. Ultimately, several p-n junctions incorporated in individual nanowires are hoped to provide material- and energy-efficient nanowire-based solar cells [51–53].

Despite extensive investigations on light absorption in nanowires, the research so far has focused mostly on the spectral and polarization response of these nanostructures. Many studies have considered nanowires illuminated perpendicularly to their axis as Mie scatterers [39–41]. Finite nanowires illuminated from the direction parallel to their axis are referred to as optical nanofibers [44–46], to which the incident light can couple and be absorbed. These two limiting cases have not been unified so far and their relative influence on absorptance of nanowires is yet unknown. To understand the relative contribution of these absorption mechanisms and further optimize nanowire-based photovoltaic devices, the angle-dependent absorption of individual nanowires needs to be explored.

This thesis has been devoted to the fundamental investigation of light emission and absorption by individual and ensembles of semiconductor nanowires. In particular, we have developed new techniques to investigate the directional absorption by individual nanowires and unified the description of emission and absorption by these nanostructures. These results provide simple guidelines for the design of novel nanowire-based light-emitting devices or solar cells.

1.2 Vapor-liquid-solid growth of nanowires

Methods developed for manufacturing semiconductor nanowires are mostly assigned to two categories: the top-down approach, where nanowires are etched from bulk semiconductor [54–58], and the bottom-up approach, in which nanowires are grown on top of substrates [1, 59]. While the top-down approach usually provides structures of good crystalline quality, much material is wasted in the etching process. This approach also limits the diversity of materials that can be used for nanowire fabrication, because any junction or heterostructure needs to be incorporated in a bulk material prior to the top-down etching.

The bottom-up growth techniques offer a superior feature over top-down techniques, namely, the increased possibilities of in-situ homo- and heteroepitaxy. Among few bottom-up methods of fabricating semiconductor nanowires, the most understood and popular is the vapor-liquid-solid (VLS) technique. This is the method that Wagner and Ellis used to fabricate the first silicon nanowires. Since all nanowire samples presented in this thesis have been grown in this way, we will focus on explaining this particular method.

The VLS technique facilitates the nanowire growth by employing metal catalyst particles (usually gold) [60]. These particles are either deposited on top of the substrate prior to growth or nucleate from the gas precursors [61–65]. The growth can be conducted in chemical vapor deposition (CVD) reactors, molecular beam epitaxy (MBE) reactors or from solutions [3]. The schematic growth process is displayed in Figure 1.1. In this figure, the relevant growth steps are shown from left to right. The substrate covered with the catalyst particles (a) is thermally annealed in the presence of a vapor flow in the reactor chamber (b). This vapor contains the precursor elements used for nanowire growth. Annealing removes native oxides from the sample surface. Moreover, during the annealing step the particles thermally expand, melt and absorb the precursors for the

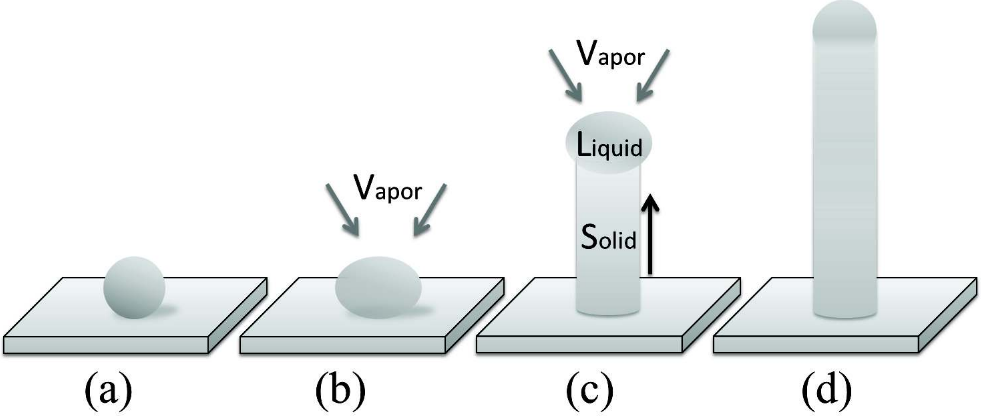

Figure 1.1: Illustration of vapor-liquid-solid (VLS) growth mechanism. (a) Catalyst particle on top a substrate before growth, at room temperature. (b) Liquid catalyst particle at the growth temperature being saturated with semiconductor material. (c) Oversaturated particle precipitates the excess of the material toward substrate and the nanowire grows. (d) Grown nanowire with the catalyst particle on top, at room temperature.

growth. Successively, upon increasing the vapor pressure in the reactor chamber, the liquid particles become supersaturated so that the excess of the semiconductor material precipitates towards the substrate and forms solid nanowires (c). This process explains the etymology of the vapor-liquid-solid method's name. In the last step of the growth process, the vapor pressure and temperature are lowered so that the particles shrink and remain on top of the grown nanowires (d). The bottom-up growth of nanowires requires less material in the form of vapor than the top-down processes, where the nanowires are etched from bulk. Therefore, the bottom-up fabrication is particularly interesting for growing nanowires from expensive semiconductors such as GaAs or InP. Homo- or heterostructures can be grown in nanowires by adding proper gas precursors in the vapor flow. For example, a temporary addition of As-containing precursor to In- and P-containing vapor flow will result in an InP-InAsP-InP heterostructure [66].

Nanowires grow typically in the [111] direction on top of the (111) plane of cubic semiconductors, if they crystallize in diamond or zincblende structures. In case of compound semiconductors (III/V), they can also crystallize in wurtzite structure with a different electronic band gap than the cubic zincblende structure [67, 68]. However, under particular growth conditions, the growth of semiconductor nanowires along the [100] direction has been also demonstrated [69, 70]. Since most of the current industrial processes are based on (100)-oriented semiconductors, the [100] growth of nanowires holds promise for simple, wafer-scale integration of those nanostructures.

The position and size of catalyst particles provides the site- and diameter-control for nanowire growth. Depending on the method of depositing catalyst particles on the

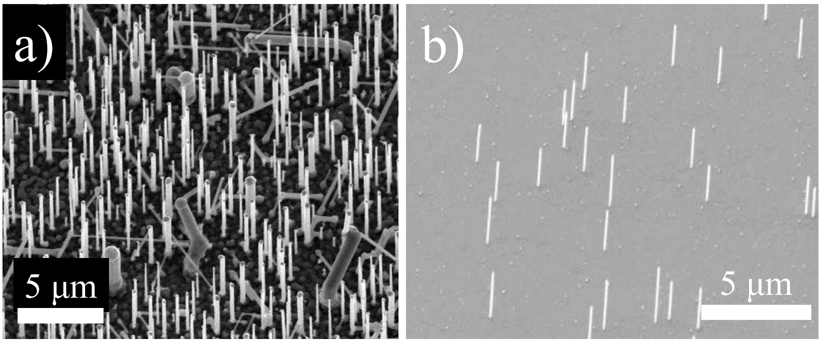

Figure 1.2: (a) Silicon nanowires grown with catalyst particle obtained from a thin gold film. The nanowires grow randomly on the surface and have a broad distribution of diameters. (b) Indium phosphide nanowires grown with spin-coated gold particles from a colloidal suspension. The uniform size of gold particles in suspension provides a minimal dispersion of nanowire diameters and random growth sites.

substrate, the growth can result in ordered or disordered ensembles of nanowires. The easiest way to obtain catalyst particles for growth is to evaporate a thin metal film on top of a substrate [3]. When this film is annealed at high temperatures, it melts and due to dewetting process the gold droplets are formed. These droplets are randomly positioned on top of the substrate and usually have a broad, log-normal distribution of diameters [71–73]. The mean of this distribution along with the surface filling fraction of these nanowires depend on the thickness of the metal film. Figure 1.2(a) shows silicon nanowires grown with catalyst particles obtained from a thin metal film. The growth results in random ensembles of size-dispersed nanowires. Instead of using a thin metal film, colloidal suspensions of metallic nanoparticles can be directly dispersed on the substrate prior to growth. Such suspensions contain particles that have a very narrow size-distribution and well-controlled particle size. Nanowires grown using such colloidal suspensions can be seen in Figure 1.2(b). Even though the nanowires are still randomly positioned on top of the substrate, their size distribution is very narrow. The average surface filling fraction of nanowires is related to the volume concentration of the metal particles in the suspension.

It has been recently demonstrated that ordered arrays of nanowires can be grown on patterned substrates [66, 74, 75]. In this case, the metal particles are deposited on the substrate by means of either electron-beam (e-beam) lithography, or nanoimprint lithography [76]. E-beam lithography provides an ultimate control over the position and size of the catalyst particles. With this method, an arbitrary pattern of particles can be created on top of a substrate for nanowire growth giving the freedom of designing the nanowire patterns on demand. Since the e-beam lithography is time consuming and expensive, the reproduction of multiple samples with a particular pattern suffers from the

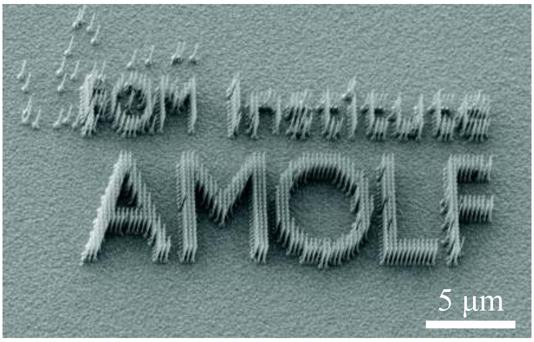

Figure 1.3: The logo of AMOLF made with InP nanowires. Catalyst particles were deposited on the substrate by means of substrate conformal imprint lithography (SCIL). A large area pattern is transferred to a polymer stamp that can be used hundreds of times to reproduce the pattern onto various substrates. This method of particle deposition provides a precise control over nanowire position and diameter.

same drawbacks. Fortunately, a wafer-scale e-beam pattern can be written on a template and transferred to a nanoimprint stamp. Such stamp can be reused numerous times allowing for growing large area nanowire patterns. Also, an unlimited number of stamps can be fabricated from the e-beam written template. An example of nanowires grown from gold particles deposited using a nanoimprint stamp is shown in Figure 1.3. This figure presents a scanning electron microscope (SEM) image of the logo of AMOLF made of InP nanowires grown on top of an InP substrate.

1.3 Outline of this thesis

In this thesis, we demonstrate and describe the directional light emission and absorption of individual semiconductor nanowires. We also investigate light propagation in ordered and random arrays of semiconductor nanowires. The thesis is organized as follows:

In Chapter 2 we give a theoretical description of light scattering and absorption by individual nanowires. Nanowires are approximated to infinitely long circular cylinders. Light scattering by such structures is explained with Mie theory. This theory is a solution of Maxwell's equations for the case of a plane wave illuminating a cylinder. On the other hand, light propagation in nanowires can be described by calculating the eigenmodes of a cylindrical waveguide. We show the comparison of these two theoretical descriptions of light-nanowire interaction.

The experimental results on the directional light emission of semiconductor nanowires were obtained using Fourier microscopy. In Chapter 3 we discuss the principles of this technique and its relevance for measuring directional light emission of nanosources.

Additionally, we show that the optical path in a Fourier microscope can be time-reversed to provide a controlled plane wave illumination of a nanostructure with a defined wave vector. Both functionalities have been combined in one experimental setup described in this chapter. We conclude Chapter 3 with the description of applications stimulated by the development of the Fourier and time-reversed Fourier microscopy in our group.

Our developed time-reversed Fourier microscope setup has been used to measure the directional light emission of individual semiconductor nanowires. These results are presented in Chapter 4. We find that individual, indium phosphide (InP) nanowires with a diameter of 100 nm are directional emitters of polarized light. The nanowires act as tiny antennas for light or optical antennas. This behavior is explained by the coupling of the emission to polarized leaky waveguide modes supported by the cylindrical geometry of nanowires. The conservation of parallel momentum of the mode at the nanowire interface provides polarized directional emission into the free space.

Using the same technique we show in Chapter 5 that the emission from ordered arrays of InP nanowires can be described as that of quasi-two dimensional photonic crystals. Such photonic crystals support Bloch modes for light originating from the interference of light propagating in the medium having a periodic modulation of the refractive index. Light emitted from the nanowires forming the photonic crystal can couple to the Bloch modes. Due to the finite length of nanowires, light coupled to these modes can leak to the free space in certain directions.

Nanowires have attracted the interest of photovoltaic research due to their efficient light absorption. Although optical absorption in individual nanowires has been widely discussed, it has never been experimentally demonstrated as a function of the angle of incident light. With the time-reversed Fourier microscope, we illuminated individually absorbing nanowires with a controlled angle of incidence under a microscope objective. Measurements of the photoluminescence intensity emitted by the nanowires demonstrate the directional absorption in individual nanowires. We find that Mie theory can be only applied for large angles of incidence with respect to the nanowire axis. For small angles, the absorption is enhanced in contrast to the predictions of Mie theory. This behavior is explained by numerical simulations that reveal the efficient coupling of incident light to waveguide modes in nanowires. Our results are the first experimental comparison of the relevance of two different absorption mechanisms in nanowires. These results are presented in Chapter 6

Photovoltaic devices based on nanowires will consist of ordered or random ensembles. The description of light propagation in such ensembles will allow to optimize the performance of nanowire solar cells. Light propagation in ordered arrays of nanowires is usually described by calculating the eigenmodes of periodic structures or by numerical simulations, while random ensembles of very thin nanowires are often described by effective medium theories assuming their optical response of the lowest order (dipolar). In Chapter 7 we demonstrate wavelength, angle and polarization-dependent light extinction in random ensembles of semiconductor nanowires with a diameter comparable to the wavelength. This light extinction was successfully described by the properties of individual nanowires forming a Mie scattering effective medium in the independent scattering approximation.

CHAPTER 2

THEORY OF LIGHT SCATTERING, ABSORPTION AND WAVEGUIDING BY INDIVIDUAL NANOWIRES

Nanowires are usually approximated to infinitely long cylinders for an analytical description of the light-nanowire interaction. The extinction, scattering and absorption of light incident on infinitely long cylinders can be quantified with Mie theory. The same cylinders support waveguide modes. These modes can propagate in the cylinder in the direction parallel to its axis or leak to the free-space. This chapter discusses Mie and waveguide theory for describing the interaction of light with nanowires and shows the similarities between the two formalisms.

2.1 Introduction

The interaction of light with semiconductor nanowires that have the diameter comparable to optical wavelengths can be described analytically in two ways. The first is Mie scattering theory, i.e, the solution of Maxwell's equations for an infinitely long circular cylinder surrounded by a homogeneous, non-absorbing medium [41, 77]. This theory describes the extinction, scattering and absorption of a plane wave incident on a cylinder. This approach has been used to study the spectrally resolved scattering and absorption in semiconductor nanowires [39–41, 78]. On the other hand, infinitely long circular cylinders can support waveguide modes. These modes can be either bound to the cylinder and propagate over large distances, or can radiate into the surrounding medium. Light coupled to bound modes (guided modes) in nanowires can lead to lasing [6–8, 16, 79]. Modes, whose energy is radiated into the surrounding medium are referred to as leaky modes. These modes have been discussed in connection with Mie theory [39, 40, 78]. Both types of waveguide modes can be used to shape the spontaneous emission and light absorption of semiconductor nanowires [23–26, 45–47, 80–83]. Although these two theories describe light interaction with the same structure, the relation between them has never been explicitly shown.

In this chapter we give the basic principles of Mie and waveguide theory for describing optical properties of nanowires. We also show the relation between those two formalisms. A more detailed description of the individual theories can be found in many textbooks, e.g, Refs. [77, 84, 85].

2.2 Mie theory of light scattering by an infinite circular cylinder

Mie theory describes the interaction of a plane wave incident on an infinitely long circular cylinder suspended in a homogeneous medium [77]. Due to the difference in refractive index of a cylinder (n_{cyl}) and that of the surrounding medium, the incident light can be scattered. This means, that energy of a beam incident on the cylinder is removed from the direction of propagation and redistributed in other directions. Light can also be absorbed if the cylinder is made of a material with a complex refractive index for the incident wavelength. Both scattering and absorption phenomena remove part of the intensity of the incident beam from the direction of its propagation. The difference between the light intensity incident on the cylinder and the intensity of light that continues propagating in the same direction after interacting with the cylinder is referred to as the extinction.

In the two simplest cases, the electric field of light incident on a cylinder can oscillate in the plane containing the axis of the cylinder and the incident k-vector, or perpendicular to this plane. We refer to these two cases as p- and s-polarized illumination, respectively. This is illustrated in Figure 2.1. In this figure, a cylinder of radius r is illuminated with a plane wave incident from the direction described by the angles θ and φ. The angle θ is measured from the axis of the cylinder to the incident wave vector and the azimuthal angle

φ is measured from the x axis of the coordinate system to the projection of the incident wave vector in the plane perpendicular to the axis of the cylinder. Due to the cylindrical symmetry of the cylinder, the incident angle is invariant of φ and can be expressed only by θ. The incident plane wave can be p-polarized ($\mathbf{E}_\mathrm{p}$, light-gray vector), or s-polarized ($\mathbf{E}_\mathrm{s}$, dark-gray vector). The wave vector of the incident light is represented in Fig. 2.1 by the red solid line.

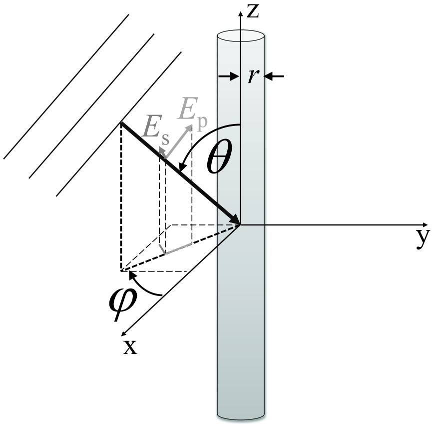

Figure 2.1: Coordinate system considered in Mie theory. An infinitely long circular cylinder of radius r is illuminated with a plane wave from a direction described by two angles (θ, φ), i.e., elevation/inclination angle and azimuthal angle of incidence, respectively.

Light extinction and scattering by an infinitely long cylinder can be described by solving Maxwell's equations in cylindrical coordinates. This solution is based on the expansion of the electric and magnetic fields of incident and scattered light into infinite series of vector cylindrical harmonics. The relation between the amplitudes of incident and scattered fields is provided by the two boundary conditions of the Maxwell's equations that must be fulfilled at the interface between the two media. These two media are characterized by their dielectric permittivities ϵ_1, ϵ_2 and magnetic permeabilities μ_1, μ_2. The first boundary condition specifies the continuity of the tangential electric ($\mathbf{E}^{\parallel}$) and magnetic ($\mathbf{H}^{\parallel}$) field components to the interface, i.e., $\mathbf{E}_1^{\parallel} = \mathbf{E}_2^{\parallel}$, $\mathbf{H}_1^{\parallel} = \mathbf{H}_2^{\parallel}$. The second boundary condition establishes that the components of the electric displacement field ($\mathbf{D}^{\perp} = \epsilon\mathbf{E}^{\perp}$) and magnetic induction field ($\mathbf{B}^{\perp} = \mu\mathbf{H}^{\perp}$) normal to the plane tangent to the interface are also conserved, i.e., $\mathbf{D}_1^{\perp} = \mathbf{D}_2^{\perp}$, $\mathbf{B}_1^{\perp} = \mathbf{B}_2^{\perp}$. Although the idea of solving Maxwell's equations in cylindrical geometry might sound simple, the actual mathematical procedure is laborious and beyond the scope of this thesis. Here, we give the expressions necessary to reproduce the results of this thesis, while the exact mathematical formalism of Mie theory can be found in Ref. [77].

Light interaction with a cylinder can be quantified by introducing the concept of optical cross section. This cross section is a measure of light intensity removed from an incident light beam and has the unit of area. The optical cross section of a particle indicates how big a non-resonant obstacle in the light path must be to block a particular fraction of incident light intensity. Since there are three possible interactions that can be taken into account, extinction, scattering and absorption cross sections can be introduced. Each of these cross sections describes the fraction of the incident light intensity that is extinct, scattered or absorbed by the object. For infinitely long cylinders considered in Mie theory, the cross sections are also infinite and should be given per unit length. To stress the resonant optical response of cylinders, these cross sections per unit length can be normalized to the geometrical cross section of the cylinder per unit length. In this way, the extinction, scattering and absorption efficiencies are obtained. A scattering efficiency of 1 means that the intensity of the incident beam removed due to scattering by a cylinder is the same as the intensity removed by a non-resonant obstacle of the same dimensions as the cylinder.

Mie theory gives the expressions for scattering (Q_{sca}) and extinction (Q_{ext}) efficiencies. For a cylinder of radius r illuminated with p-/s-polarized light of free-space wavelength λ (corresponding to $k_0 = \frac{2\pi}{\lambda}$) under an angle θ, these efficiencies are given by

$$Q^{\text{p}}_{\text{sca}} = \frac{2}{k_0 r}\left[|b^{\text{p}}_0|^2 + 2\sum_{n=1}^{\infty}\left(|b^{\text{p}}_{\text{n}}|^2 + |a^{\text{p}}_{\text{n}}|^2\right)\right], \tag{2.1a}$$

$$Q^{\text{p}}_{\text{ext}} = \frac{2}{k_0 r}\text{Re}\left(b^{\text{p}}_0 + 2\sum_{n=1}^{\infty} b^{\text{p}}_{\text{n}}\right), \tag{2.1b}$$

$$Q^{\text{s}}_{\text{sca}} = \frac{2}{k_0 r}\left[|a^{\text{s}}_0|^2 + 2\sum_{n=1}^{\infty}\left(|a^{\text{s}}_{\text{n}}|^2 + |b^{\text{s}}_{\text{n}}|^2\right)\right], \tag{2.1c}$$

$$Q^{\text{s}}_{\text{ext}} = \frac{2}{k_0 r}\text{Re}\left(a^{\text{s}}_0 + 2\sum_{n=1}^{\infty} a^{\text{s}}_{\text{n}}\right). \tag{2.1d}$$

The efficiencies are functions of the scattering coefficients, a^{p}_{n}, b^{p}_{n}, a^{s}_{n}, and b^{s}_{n}. These coefficients relate the amplitudes of scattered electric and magnetic fields to the incident fields and can be associated with the Fresnel reflection and transmission coefficients in a cylindrical geometry. Here, n indicates the order of vector cylindrical harmonics, in which the incident and scattered fields are expanded. The expressions for the scattering coefficients are

$$a_{\mathrm{n}}^{\mathrm{p}} = \frac{C_{\mathrm{n}} V_{\mathrm{n}} - B_{\mathrm{n}} D_{\mathrm{n}}}{W_{\mathrm{n}} V_{\mathrm{n}} + i D_{\mathrm{n}}^2}, \tag{2.2a}$$

$$b_{\mathrm{n}}^{\mathrm{p}} = \frac{W_{\mathrm{n}} B_{\mathrm{n}} + i D_{\mathrm{n}} C_{\mathrm{n}}}{W_{\mathrm{n}} V_{\mathrm{n}} + i D_{\mathrm{n}}^2}, \tag{2.2b}$$

$$a_{\mathrm{n}}^{\mathrm{s}} = -\frac{A_{\mathrm{n}} V_{\mathrm{n}} - i C_{\mathrm{n}} D_{\mathrm{n}}}{W_{\mathrm{n}} V_{\mathrm{n}} + i D_{\mathrm{n}}^2}, \tag{2.2c}$$

$$b_{\mathrm{n}}^{\mathrm{s}} = -i \frac{C_{\mathrm{n}} W_{\mathrm{n}} + A_{\mathrm{n}} D_{\mathrm{n}}}{W_{\mathrm{n}} V_{\mathrm{n}} + i D_{\mathrm{n}}^2}, \tag{2.2d}$$

where

$$A_{\mathrm{n}} = i\xi \left(\xi J_{\mathrm{n}}'(\eta) J_{\mathrm{n}}(\xi) - \eta J_{\mathrm{n}}(\eta) J_{\mathrm{n}}'(\xi) \right), \tag{2.3a}$$

$$B_{\mathrm{n}} = \xi \left(m^2 \xi J_{\mathrm{n}}'(\eta) J_{\mathrm{n}}(\xi) - \eta J_{\mathrm{n}}(\eta) J_{\mathrm{n}}'(\xi) \right), \tag{2.3b}$$

$$C_{\mathrm{n}} = n \cos(\theta) \eta J_{\mathrm{n}}(\eta) J_{\mathrm{n}}(\xi) \left(\frac{\xi^2}{\eta^2} - 1 \right), \tag{2.3c}$$

$$D_{\mathrm{n}} = n \cos(\theta) \eta J_{\mathrm{n}}(\eta) H_{\mathrm{n}}^{(1)}(\xi) \left(\frac{\xi^2}{\eta^2} - 1 \right), \tag{2.3d}$$

$$V_{\mathrm{n}} = \xi \left(m^2 \xi J_{\mathrm{n}}'(\eta) H_{\mathrm{n}}^{(1)}(\xi) - \eta J_{\mathrm{n}}(\eta) H_{\mathrm{n}}^{(1)\prime}(\xi) \right), \tag{2.3e}$$

$$W_{\mathrm{n}} = i\xi \left(\eta J_{\mathrm{n}}(\eta) H_{\mathrm{n}}^{(1)\prime}(\xi) - \xi J_{\mathrm{n}}'(\eta) H_{\mathrm{n}}^{(1)}(\xi) \right). \tag{2.3f}$$

In Eq. 2.3, $\xi = k_0 r \sin(\theta)$, $\eta = k_0 r \sqrt{m^2 - \cos^2(\theta)}$, $m = \frac{n_{\mathrm{cyl}}}{n_{\mathrm{med}}}$ is the refractive index of the cylinder relative to that of the surrounding medium and θ the angle of incidence. The absorption efficiencies for both polarizations can be determined by calculating the difference between the extinction and scattering efficiencies:

$$Q_{\mathrm{abs}}^{\mathrm{p,s}} = Q_{\mathrm{ext}}^{\mathrm{p,s}} - Q_{\mathrm{sca}}^{\mathrm{p,s}}. \tag{2.4}$$

In case the cylinder is illuminated with unpolarized light, the efficiencies can be averaged over polarization,

$$Q = \frac{1}{2} \left(Q^{\mathrm{p}} + Q^{\mathrm{s}} \right). \tag{2.5}$$

For a cylinder illuminated perpendicular to its axis ($\theta = 90°$) the scattering coefficients $a_{\mathrm{n}}^{\mathrm{p}} = b_{\mathrm{n}}^{\mathrm{s}} = 0$. The electric field of p-polarized excitation is parallel to the axis of the cylinder, while that of s-polarized excitation is perpendicular to this axis. Therefore, the excitations are respectively, purely transverse magnetic (TM) of transverse electric (TE). In this case, the coefficient $b_{\mathrm{n}}^{\mathrm{p}}$ is associated with a TM resonance, while $a_{\mathrm{n}}^{\mathrm{s}}$ is associated with a TE resonance. At other angles of incidence, the resonances have signatures of combined TM and TE resonances. Therefore, the scattering efficiencies are calculated by summing the coefficients that are characteristic for both types of resonances, as in Eq. 2.1.

The efficiencies given in Eq. 2.1 are infinite series of vector cylindrical harmonics. Each particular harmonic can be associated with a particular order of the cylinder's response to the incident light. In this way, scattering coefficients for n = 0 are responsible for the lowest, dipolar response of the cylinder, n = 1 for quadrupolar, n = 2 for sextupolar etc. [77, 78, 86, 87]. The resonant coupling of the incident light to the cylinder should occur when an integer number of wavelengths in the cross section of the cylinder matches the circumference of this cylinder [78]. The total efficiencies are obtained by summing all orders of the optical response. However, it is possible to illustrate the contributions of particular resonance orders to the total extinction efficiency. Figure 2.2 shows the wavelength-dependent extinction efficiency of an InP cylinder in vacuum ($n_{\text{med}} = 1$) of radius $r = 50$ nm illuminated perpendicularly to its axis ($\theta = 90°$) with p- (a) and s-polarized (b) light. The total extinction efficiency is plotted with black solid lines. The non-solid lines represent the partial extinction efficiency calculated for individual scattering coefficients that represent a particular resonance of order n. From these plots it is evident that the lowest resonant order is responsible for the high extinction at long wavelengths, while the successive orders contribute to the light extinction at shorter wavelengths. For very thin cylinders only the few lowest order resonances contribute to the extinction. If the diameter ($2r$) of the cylinder is very small compared to the wavelength of incident light, Mie theory converges to Rayleigh scattering, in which only the dipolar response of the scattering is considered.

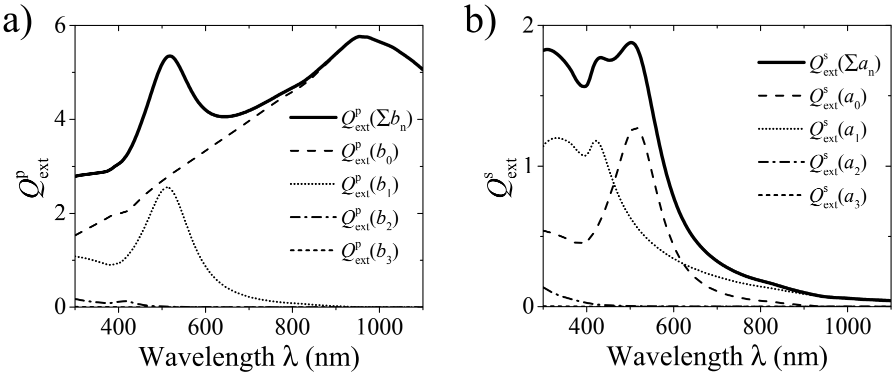

Figure 2.2: Extinction efficiency Q_{ext} for (a) p- and (b) s-polarized light incident perpendicular to the axis of an InP cylinder ($\theta = 90°$) of radius $r = 50$ nm (black solid lines). The efficiency is plotted as a function of the wavelength of the incident light. The contributions of consecutive resonant orders to the extinction efficiency are plotted for n = 0 (dashed lines), n = 1 (dotted lines), n = 2 (dash-dotted lines) and n = 3 (short-dashed lines).

The efficiencies can be calculated as a function of the cylinder's radius, wavelength and angle of incident light for p- and s-polarized excitation. Figure 2.3 shows the calculated scattering [(a) and ((b)] and absorption [(c) and (d)] efficiencies as a function of the diameter of the cylinder $d = 2r$ and the wavelength of the incident light λ for an InP cylinder surrounded by vacuum ($n_{\mathrm{med}} = 1$) illuminated perpendicular to its axis ($\theta = 90°$). The efficiencies for p-polarized excitation are plotted in (a) and (c), while the efficiencies for s-polarized excitation are plotted in (b) and (d). In this calculation the full dispersion of the complex refractive index of InP is taken into account. This figure illustrates that thicker cylinders support more Mie resonances. For a particular wavelength (top profiles in Fig. 2.3), the resonances are equidistant as a function of the diameter. This fact supports the intuitive condition that at the resonance, the integer number of effective wavelengths in the cross section of the cylinder needs to match its circumference [78].

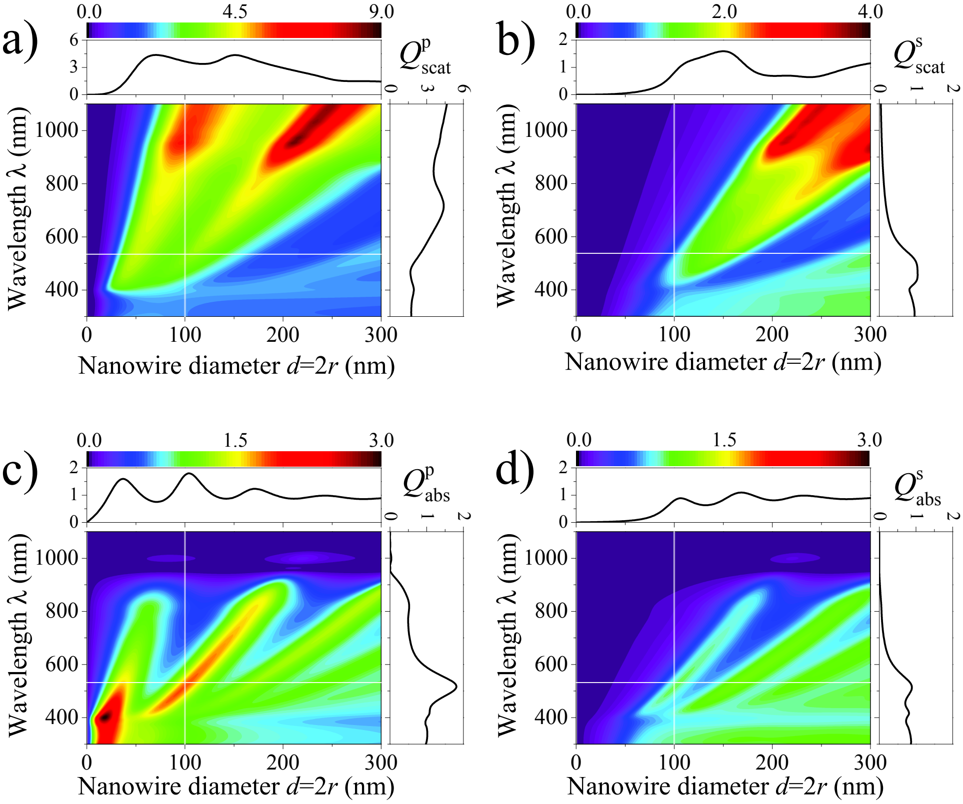

Figure 2.3: (a) Scattering efficiency of an InP cylinder in vacuum illuminated normally to its axis ($\theta = 90°$) as a function of its diameter $d = 2r$ and wavelength for p-polarized incident light. (b) Scattering efficiency as in (a), but for s-polarized incident light. (c), (d) Absorption efficiency of the same InP cylinder and under the same illumination for p- and s-polarization as in (a) and (b), respectively. Each plot is accompanied by the profiles at constant wavelength $\lambda = 532$ nm (top profiles) and constant diameter $d = 100$ nm (right-side profiles).

The absorption efficiency for both polarizations decreases abruptly at wavelengths around λ = 920 nm due to the band gap of InP that makes this material transparent for longer wavelengths. However, the scattering efficiency does not decrease. This is because the scattering depends on the real component of the complex refractive index of the material forming the cylinder relative to the refractive index of the surrounding medium. Since the real component of the refractive index of the cylinder is nearly constant at long wavelengths, the scattering efficiency does not vanish, and even increases. This increase is related to the absence of absorption.

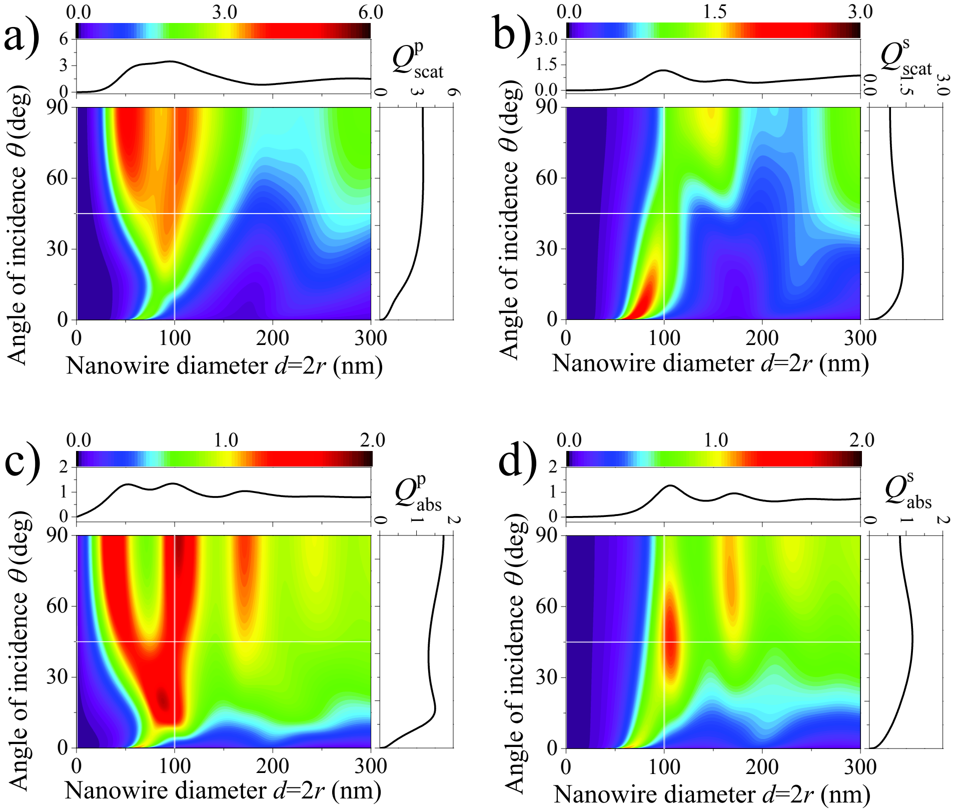

Figure 2.4: (a) Scattering efficiency of an InP cylinder in vacuum (n_{med} = 1) illuminated with p-polarized light of wavelength λ = 532 nm as a function of its diameter $d = 2r$ and angle of incidence θ. (b) Scattering efficiency as in (a), but for s-polarized incident light. (c) Absorption efficiency of the same InP cylinder under p-polarized illumination. (d) Absorption efficiency as in (c), but for s-polarized incident light. Each plot is accompanied by the profiles at constant angle of incidence $\theta = 45°$ (top profiles) and constant diameter d = 100 nm (right-side profiles).

Mie efficiencies depend also on the angle of incidence θ. In Figure 2.4 we plot the calculated scattering [(a) and ((b)] and absorption [(c) and (d)] efficiencies as a function of the diameter and the angle of incidence at fixed wavelength $\lambda = 532$ nm for an InP cylinder surrounded by vacuum. The efficiencies for p-polarized excitation are plotted in (a) and (c), while the efficiencies for s-polarized excitation are plotted in (b) and (d). Again, the full dispersion of the complex refractive index of InP is considered. Both scattering and absorption efficiencies decrease to zero for very small incident angles (illumination nearly parallel to the axis of the cylinder). For certain diameters (such as $d = 100$ nm) the absorption is not very sensitive to the angle of incidence. This is because the two lowest-order TM-like resonances can join and contribute to the absorption at nearly-parallel incidence with respect to the cylinder's axis. This is very promising for photovoltaic applications, where it is beneficial to absorb light efficiently in broad range of angles of incidence.

The calculations presented so far consider a cylinder embedded in a homogeneous medium. The effect of the inhomogeneous environment on Mie efficiencies in case of a cylinder lying on top of a substrate can be taken into account analytically by introducing an effective refractive index of the surrounding medium [88]. Otherwise it is necessary to perform numerical simulations for a specified geometry [40, 89].

2.3 Eigenmodes of a cylinder

Light propagating in any medium can be referred to as coupled to an optical mode supported by this medium. In extended homogeneous media, such as vacuum or a bulk semiconductor, there is a continuum of modes available for light propagation. As a result, light of any wavelength/frequency can travel in any direction. However, if we reduce the size of the medium to a dimension comparable to the wavelength of light, the boundaries of this medium will impose the reduction of the number of available modes and eventually, discrete eigenmodes will emerge. This situation is analogous to solid state physics, where a reduction of the material size can lead to appearance of discrete electronic states in quantum wells, quantum wires and quantum dots.

The dispersion relation of electromagnetic modes depends on the geometry of the structure. In case of planar slabs and infinitely long cylinders it is possible to derive analytical expressions for this dispersion relation. For cylinders, the derivation assumes the expansion of the electric and magnetic fields inside and around the cylinder in vector cylindrical harmonics involving Bessel and Hankel functions. These functions are the elementary wavefunctions of the wave equation in cylindrical coordinates. A detailed derivation of the electric and magnetic fields in a cylindrical structure can be found in Ref. [84]. A cylinder of radius r composed of a material of dielectric permittivity ϵ_{cyl} and magnetic permeability μ_{cyl} (refractive index $n_{\mathrm{cyl}} = \sqrt{\epsilon_{\mathrm{cyl}}\mu_{\mathrm{cyl}}}$), surrounded by a medium of ϵ_{med} and μ_{med} ($n_{\mathrm{med}} = \sqrt{\epsilon_{\mathrm{med}}\mu_{\mathrm{med}}}$) such that $n_{\mathrm{cyl}} > n_{\mathrm{med}}$ supports waveguide modes. Since here we consider nonmagnetic materials, $\mu_{\mathrm{cyl}} = \mu_{\mathrm{med}} = 1$. The dispersion relation of waveguide modes supported by a cylinder can be found by solving the characteristic transcendental equation for the propagation constant k_{z} which is obtained by imposing the electromagnetic boundary conditions to the fields in the cylindrical geometry.

$$\begin{aligned}\left[\frac{\mu_{\text{cyl}}}{u}\frac{J'_{\text{n}}(u)}{J_{\text{n}}(u)}-\frac{\mu_{\text{med}}}{v}\frac{H'_{\text{n}}(v)}{H_{\text{n}}(v)}\right]\left[\frac{\epsilon_{\text{cyl}}}{u}\frac{J'_{\text{n}}(u)}{J_{\text{n}}(u)}-\frac{\epsilon_{\text{med}}}{v}\frac{H'_{\text{n}}(v)}{H_{\text{n}}(v)}\right]&\\ =\pm\text{n}^2\frac{(k_{\text{z}})^2}{(k_0)^2}\left(\frac{1}{v^2}-\frac{1}{u^2}\right)^2,&\end{aligned}\tag{2.6}$$

In the equation, the variable n is an integer defining the order of the cylindrical Bessel (J_{n}) and first kind Hankel (H_{n}) functions, $k_0=\frac{2\pi}{\lambda}$ is the free-space wavenumber, $u=k_{\text{cyl}}r$, and $v=k_{\text{med}}r$. The variables u and v contain the transverse components of the mode wave vector given by

$$k_{\text{cyl}}^2=\epsilon_{\text{cyl}}k_0^2-k_{\text{z}}^2,\tag{2.7a}$$

$$k_{\text{med}}^2=\epsilon_{\text{med}}k_0^2-k_{\text{z}}^2.\tag{2.7b}$$

Every value of the propagation constant k_{z} that fulfills Eq. 2.6 describes an eigenmode of the cylinder. This propagation constant can be associated with the effective wavelength of a mode propagating along the cylinder, $k_{\text{z}}=\frac{2\pi}{\lambda_{\text{eff}}}$. Depending on the contributions of the orthogonal components of the electric/magnetic field, the eigenmodes can be referred to as transverse magnetic (TM), transverse electric (TE), magnetoelectric (HE) or electromagnetic (EH). TM modes are characterized by the magnetic field oriented perpendicular to the axis of the cylinder. For TE modes it is the electric field that is perpendicular to the axis of the cylinder. Pure TM and TE modes exist only for n = 0. In this case Eq. 2.6 can be separated into two independent equations:

$$\left[\frac{\epsilon_{\text{cyl}}}{u}\frac{J'_0(u)}{J_0(u)}-\frac{\epsilon_{\text{med}}}{v}\frac{H'_0(v)}{H_0(v)}\right]=0\tag{2.8}$$

for the TM_0 modes, and

$$\left[\frac{\mu_{\text{cyl}}}{u}\frac{J'_0(u)}{J_0(u)}-\frac{\mu_{\text{med}}}{v}\frac{H'_0(v)}{H_0(v)}\right]=0\tag{2.9}$$

for TE_0 modes.
In HE modes, the magnetic field is dominant over the electric field, contrary to the field in EH modes. HE modes are obtained by solving Eq. 2.6 with a '+' sign on the right hand side of the equation, while the EH modes emerge from solving the same equation with a '-' before the term on the right hand side of the equation.

All eigenmodes can be labeled with two numbers: the azimuthal mode number n, that describes the number of field maxima in the azimuthal direction, and the radial mode number l, that refers to the number of field maxima in the radial direction. The concept of numbering the modes becomes obvious after examining the transverse electric field profiles of particular modes. These profiles are shown in 2.5. For TE_{01} and TM_{01} modes the electric field component in the cross section of the cylinder is axially-symmetric. The mode profiles of large azimuthal mode orders n resemble that of so-called whispering

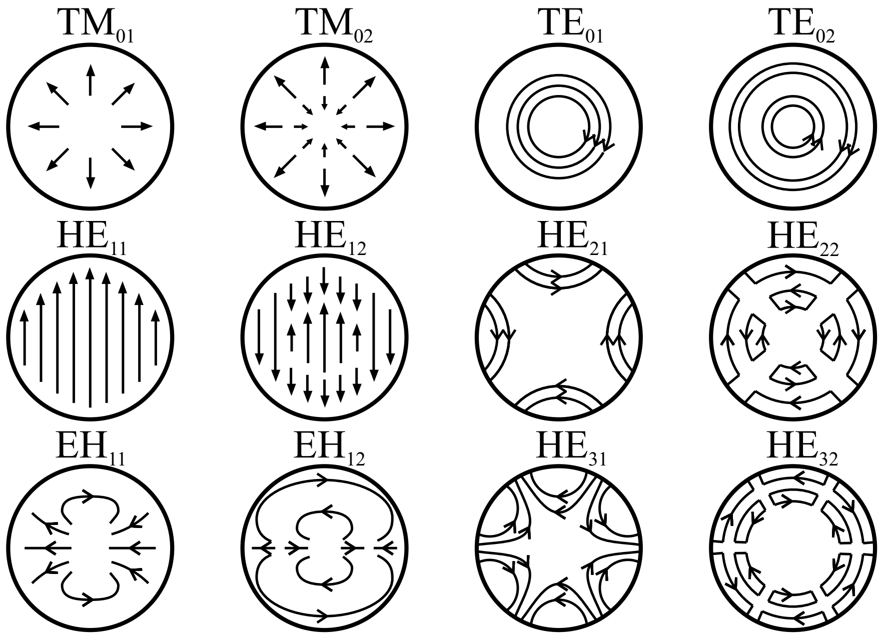

Figure 2.5: Plots of the in-plane electric field lines of several low-order eigenmodes in the cross section of an infinitely long cylinder. These field profiles have been reproduced based on Ref. [90–92].

gallery modes [93–95]. In this case, the electric field of the modes is guided close to the circumference of the cylinder's cross-section, analogically to sound waves in a whispering gallery [96].

The propagation constant k_z for which Eq. 2.6 is solved can have either purely real values, or complex values. The purely real values of k_z such that $k_z > n_{\text{med}} k_0$ characterize guided modes that are bound to the cylinder. The amplitude of the fields outside the cylinder decays exponentially. In a perfectly straight, uniform non-absorbing cylinder these guided modes propagate over very large distances without any attenuation. Such modes find application in,e.g., optical fibers used for telecommunication. If k_z has an imaginary component, the fields decay exponentially as they propagate along the cylinder's axis. These modes lose energy, which 'leaks' out of the cylinder [97, 98]. The decay length of these modes(L_d) is defined as the length at which $I/I_0 = 1/e$. Therefore, it is related to $\mathrm{Im}(k_z)$ by

$$I = I_0 e^{-2\mathrm{Im}(k_z)L_d}, \tag{2.10a}$$

$$L_d = \frac{1}{2\mathrm{Im}(k_z)}. \tag{2.10b}$$

The real component of the propagation constant of leaky modes is such that $\mathrm{Re}(k_z) < n_{\mathrm{med}} k_0$. Leaky modes find application in designing directional electromagnetic antennas at radio frequencies radiating efficiently to the far field [99].

Figure 2.6 shows the dispersion relation ($k_0 r$ plotted as a function of $k_z r$) of the eigenmodes of a cylindrical waveguide calculated by finding the real and complex roots of Eq. 2.6. The cylinder is assumed to be made of a non-absorbing medium of refractive index $n_{\mathrm{cyl}} = 3.7$. The modes are found for a fixed frequency that corresponds to the free-space wavelength of $\lambda = 532$ nm, and for varying the radius of the cylinder from 1 to 100 nm. The light cone in vacuum is indicated by the gray area in the plot. Leaky modes with complex k_z such that $\mathrm{Re}(k_z) < n_{\mathrm{med}} k_0$ are found in the light cone. Guided modes with purely real $k_z > n_{\mathrm{med}} k_0$ can be found below the light line, which delimits the light cone. The black area in the plot represents the forbidden cone, where no modes can exist. Each leaky mode originates from a guided mode that extends beyond the light line. For very small diameters only the fundamental HE_{11} mode is supported. This mode is guided but its dispersion approaches the light line, which makes it very weakly confined to the cylinder as the diameter is reduced.

2.4 Relation between Mie resonances and leaky eigenmodes of a cylinder

Mie and waveguide theories for infinitely long cylinders are closely related. Both formalisms are based on the expansion of the electric and magnetic fields into cylindrical harmonics, followed by imposing the same boundary conditions. By examining the resonance condition in the Mie scattering coefficients, we can obtain the characteristic equation for the cylindrical waveguide. In the case of a perfect resonant coupling of an incident plane wave to Mie resonances, the amplitudes of the fields scattered by a cylinder (the Mie scattering coefficients) become infinite. This occurs when the common denominator of the Mie scattering coefficients in Eq. 2.2 equals zero, i.e., $W_n V_n + iD_n^2 = 0$. If the angle of incidence θ is measured from the axis of the cylinder, the z-component of the incident wave number $n_{\mathrm{med}} k_0$ is $k_z = n_{\mathrm{med}} k_0 \cos(\theta)$. After this substitution, the resonance condition becomes a characteristic equation (Eq. 2.6) of a cylindrical waveguide. The roots of this equation (k_z) represent the eigenmodes of the cylinder. Therefore, we can state that by estimating the scattering coefficients, Mie theory quantifies the coupling of incident plane waves to eigenmodes of the cylinder.

The eigenmodes of a cylinder are characterized by the wave number (propagation

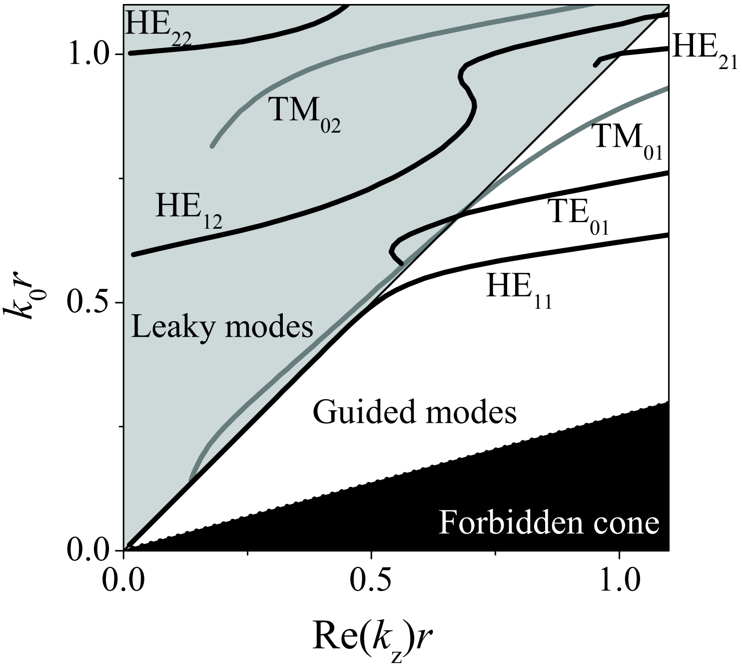

Figure 2.6: Dispersion relation of guided and leaky modes supported by an infinitely long cylinder. The cylinder has a refractive index $n_{\text{cyl}} = 3.7$ and it is surrounded by vacuum. In this plot, the frequency of the modes is fixed at the value corresponding to the free-space wavelength $\lambda = 532$ nm and the radius of the cylinder r is varied. The different modes are labeled in the plot. The light cone of vacuum is indicated by the gray-shaded area. The white area is the light cone in InP that supports guided modes, while the black area is the forbidden cone, where no modes can exist.

constant) k_z along the axis. In order to efficiently couple to a mode from the free-space, this wave number needs to be phase-matched to the excitation. Guided modes have a purely real propagation constant that is always larger than the wave number in the surrounding medium at the same frequency, $k_z > n_{\text{med}}k_0$. A plane wave incident on a cylinder from the free-space also has a purely real value of the wave number, with a z-component given by $k_z = n_{\text{med}}k_0\cos(\theta)$. Due to the fact that cylinders considered in Mie theory are infinitely long, the scattering problem for parallel incidence at $\theta = 0°$ in undefined. For any other angle of incidence, the z-component of an incident wave number is always smaller than that of any guided mode. This means that Mie theory can not account for the coupling of free-space plane waves to guided modes in cylinders.

Leaky modes are characterized by a complex wave number, with a real component $\text{Re}(k_z) < n_{\text{med}}k_0$. Therefore, an incident plane wave can couple to them. Since the wave number of leaky modes is complex, also the Im(k_z) needs to be matched for a resonant coupling of a plane wave to a leaky mode. [100–102] However, the wave number of the incident plane wave is purely real. In order to phase-match an incident plane wave to a leaky mode, we can introduce a complex frequency of the excitation. The real component of this complex frequency is related to the wavelength of incident light ($\mathrm{Re}(\omega) = k_0 c = \frac{2\pi c}{\lambda}$, where c is the speed of light in vacuum). The imaginary frequency ($\mathrm{Im}(\omega)$) can be understood as the optical retardation between the electric field of the incident plane wave and the electric field of the leaky mode. If now, we solve Eq. 2.6 for purely real $k_z = k_0 \cos(\theta)$ and $\mathrm{Im}(\omega)$ for a fixed $\mathrm{Re}(\omega)$, r and material constants, we will obtain pairs of (k_z, $\mathrm{Im}(\omega)$) defining the Mie resonance condition for an incident plane wave. We will call these eigenvalues of Eq. 2.6 the Mie resonance conditions.

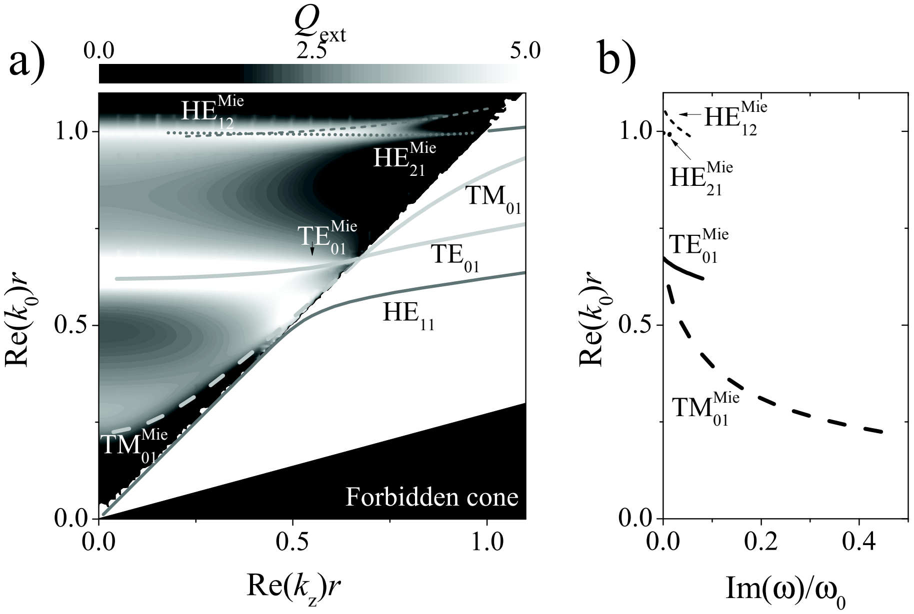

Figure 2.7: (a) Dispersion relation of guided modes (solid lines labeled with black-fonts) supported by an infinitely long cylinder and Mie resonance conditions (lines in the light cone of vacuum, labeled with white-fonts). The cylinder has a refractive index $n_{\mathrm{cyl}} = 3.7$ and it is surrounded by vacuum. In this plot, the real frequency component of the modes is fixed at the value corresponding to the free-space wavelength of light incident on a cylinder λ = 532 nm and the radius of the cylinder r is varied. The modes and Mie resonance conditions are labeled in the plot and have a unique line style. The contour plot shows the polarization-averaged extinction efficiency calculated for the same cylinder using Mie theory. The values of the extinction efficiency is represented by the gray scale shown above the dispersion relation. (b) Imaginary frequency component of the Mie resonance conditions shown in (a). The imaginary frequency is normalized to the frequency of the excitation and plotted with the same line styles as the corresponding Mie resonance conditions in (a).

Figure 2.7(a) shows the calculated Mie resonance conditions for coupling of free-space plane waves to leaky modes of a cylindrical waveguide compared to the unpolarized Mie extinction efficiency of the same cylinder. The cylinder surrounded by vacuum ($n_{\text{med}} = 1$) is assumed to be lossless and to have a refractive index of $n_{\text{cyl}} = 3.7$. For the eigenmode calculations, the variable is the radius of the cylinder in the range 1 to 100 nm. The unpolarized Mie extinction efficiency is also calculated as a function of the radius of the cylinder and the angle of incidence θ or $k_z = k_0 \cos(\theta)$ and represented as a contour plot in Fig. 2.7. The free-space wavelength for all the calculations is fixed at $\lambda = 532$ nm.

Generally, the calculated Mie resonance conditions (lines in the light cone of vacuum in Fig. 2.7(a)) coincide with the maxima of the Mie extinction efficiency (appearing as white areas in the same figure). However, it is evident that the dispersion relation of the Mie resonance conditions in Fig. 2.7(a) is different from that of the leaky modes in Fig. 2.6. This is because the introduction of the imaginary frequency for calculating the Mie resonance conditions results in a different k_z. However, both, Mie resonance conditions and their respective leaky modes (see Fig. 2.6) exist for the same cylinder radii and overlap at the light line (e.g. TM_{01} and $\text{TM}_{01}^{\text{Mie}}$ or TE_{01} and $\text{TE}_{01}^{\text{Mie}}$ modes and Mie resonance conditions converge to the same point in the light line). For Mie resonance conditions, this is the case when the cylinder is illuminated nearly parallel to its axis ($\theta = 0°$, $k_z = k_0$). This convergency can be explained as the decreasing phase mismatch between the k_z of an incident plane wave and that of a leaky mode having low values of $\text{Im}(k_z)$ close to the light line [97, 98]. The imaginary component of the complex frequency, which is a measure of the phase mismatch, can be appreciated in Fig. 2.7(b). In this figure, the imaginary frequency is plotted with the same line styles as the corresponding Mie resonance conditions in Fig. 2.7(a). Typically, for small values of the imaginary frequency ($\text{Im}(\omega)/\omega_0 < 0.1$), the Mie extinction efficiency associated with a particular Mie resonance condition has high values and narrower linewidth of the resonance. Strong Mie resonances occur when incident light can couple to several modes, as for $k_0 r \sim 0.6$ or 1.0.

2.5 Conclusions

We have presented two theoretical formalisms used for describing the interaction of light with semiconductor nanowires. Mie theory gives the extinction, scattering and absorption efficiencies of infinitely long cylinders to which nanowires are typically approximated. Waveguide theory allows finding optical eigenmodes supported by nanowires/cylinders. Light coupled to these eigenmodes can be either guided or leak to free-space depending on the propagation constant of a particular mode. Finally, we have demonstrated that Mie theory actually quantifies the plane wave excitation of leaky modes supported by nanowires/cylinders.

CHAPTER 3

TIME-REVERSED FOURIER MICROSCOPY: PRINCIPLES, APPLICATIONS AND OUTLOOK

In this chapter we explain the principles of Fourier microscopy. This technique is based on the property of lenses that focus plane waves incident from different directions on unique positions in their back focal plane. Fourier microscopy is used in this thesis for measuring the directional emission of semiconductor nanowires. We also show that the light path in a Fourier microscope can be reversed so that a sample under an objective lens can be illuminated with a plane wave with a controlled angle of incidence. We call this technique time-reversed Fourier microscopy and it can be used to investigate the angle-dependent scattering and absorption of single nanostructures. Finally, we suggest the applications of Fourier and time-reversed Fourier microscopy for designing more efficient optoelectronic devices.

3.1 Measurements of directional light emission and absorption at the nanoscale

Directional optical properties of large-area samples are typically measured by using precise rotation stages (goniometers) [18, 43, 103–105]. In this case, the control of the angle of incidence is attained by rotating the sample with respect to a collimated light beam incident from a fixed direction. Light that is emitted or scattered by the sample in a particular direction can be collected by a detector which can be rotated around the sample. The larger the distance between the detector and the sample, the smaller solid angle of emitted/scattered light is recorded. This solid angle determines the angular resolution of the detection. In most cases, such experimental setups are equipped with a detector that can rotate only in one plane, usually the plane of incidence onto the sample. This means, that nearly all light emitted/scattered into a large solid angle is not analyzed. Also, the signal available to the detector decreases as $\frac{1}{R^2}$, where R is the distance between the detector and the sample. Considering the emission/scattering efficiencies of individual nanostructures, measurements of their directional photonic properties are impossible using rotation stage-based techniques. This type of measurements requires microscopy.

The simplest microscope is formed by a single lens that allows to form a magnified real image of the object placed in front of it. This image can be retrieved by placing a screen/detector in the image plane, behind the lens. To achieve large magnifications and minimize imperfections of the optical imaging, standard optical microscopes are based on complex optical systems consisting of many lenses. These microscopes are generally used for imaging the surface of a sample, or for spectroscopy measurements, such as microphotoluminescence (μ−PL).

Fourier microscopes can also consist of only one lens, but they do not aim to form the image of the object. Instead, the lens can decompose the incident light into plane waves and focus each of them at the back focal plane (BFP). This BFP contains the information about light intensity scattered/emitted in particular directions. A screen/detector placed in the BFP reveals an intensity map of the directional scattering/emission referred to as Fourier image. Fourier microscopy has been used for imaging the directional emission of fluorescent beads [106], dye-molecules coupled to plasmonic gratings [107], surface plasmon polariton waveguides [108], quantum dots coupled to plasmonic antennas [109] or single plasmonic nanowires [110, 111]. This technique can be applied to measure the directional emission of any nanostructure. Using Fourier microscopy, we reported the first measurements of the directional emission of individual semiconductor nanowires [82].

Besides directional emission, understanding the angle-dependent absorption by individual nanostructures is of great importance for modern photovoltaics. New designs of efficient solar cells are based on nanostructures such as semiconductor nanowires [31, 48, 52, 112]. To fully optimize the performance of new generation photovoltaic devices it is important to understand the directional absorption of their individual building blocks. The spectrally resolved absorption in single nanowires has been reported recently [39, 113–115]. However, the angular absorption by individual nanowires is experimentally unexplored because it is challenging to measure. By time-reversing the light path in a Fourier microscope it is possible to attain an angle-controlled plane wave illumination of a sample placed under a microscope objective. Utilization of a microscope objective for illumination and collection allows the investigations of the properties of individual nanowires.

The development of the experimental setup capable of measuring directional light emission and absorption was part of this research. We have combined Fourier imaging and plane wave illumination capabilities in one experimental setup. This setup was used to measure the directional emission and absorption of individual nanowires. In the following sections we explain the principles of Fourier microscopy and describe the experimental configuration, as well as the methodology applied to calibrate this optical setup.

3.2 Principles of Fourier imaging microscopy

The principle of Fourier microscopy stems from the phase-transforming properties of spherical lenses. This phase transformation is described by the transmittivity of the lens, giving the relation between an incoming plane wave with an arbitrary amplitude distribution $U_i\left(\xi,\eta\right)$ and the transmitted spherical wave with an amplitude distribution $U_t\left(\xi,\eta\right)$ where $\left(\xi,\eta\right)$ are the coordinates in the plane of the lens. This relation between the incident and transmitted field amplitude is given by

$$U_t\left(\xi,\eta\right) = t\left(\xi,\eta\right)\cdot U_i\left(\xi,\eta\right), \tag{3.1}$$

where the transmittivity of a converging spherical lens $t\left(\xi,\eta\right)$ is given by

$$t\left(\xi,\eta\right) = \mathrm{e}^{(ikn\Delta_0)}\mathrm{e}^{\left(-i\frac{k}{2f}\left(\xi^2+\eta^2\right)\right)}, \tag{3.2}$$

where k is the wave number $\left(k=\frac{2\pi}{\lambda}\right)$, Δ_0 is the maximum thickness of the lens and f is its focal length [116]. The transmitted field amplitude can be approximated by the Fresnel diffraction integral. This amplitude at a distance f from the lens is given as a function of the incident field amplitude $U_i\left(\xi,\eta\right)$ by

$$U_f\left(\mathrm{x},\mathrm{y}\right) = \frac{\mathrm{e}^{\left(i\frac{k}{2f}\left(\mathrm{x}^2+\mathrm{y}^2\right)\right)}}{i\lambda f}\iint\limits_{-\infty}^{+\infty} U_i\left(\xi,\eta\right)\mathrm{e}^{\left(-i\frac{2\pi}{\lambda f}\left(\xi\mathrm{x}+\eta\mathrm{y}\right)\right)}\mathrm{d}\xi\mathrm{d}\eta \tag{3.3}$$

where x and y are the coordinates in the plane perpendicular to the optical axis of the lens at a distance f (back focal plane, BFP). This expression has the form of a 2D Fourier transform for light incident on the lens from a sample. This is illustrated in Figure 3.1. Light originating from a sample is decomposed by the lens into individual plane waves. Every plane wave with a unique k-vector (describing the direction of propagation) is focused on a unique point in the BFP of the lens. Hence, by imaging the Fourier plane of the objective on a CCD camera it is possible to record the emission pattern of any emitter. The exact derivations of the Fourier transform properties of lenses can be found in Ref. [116].

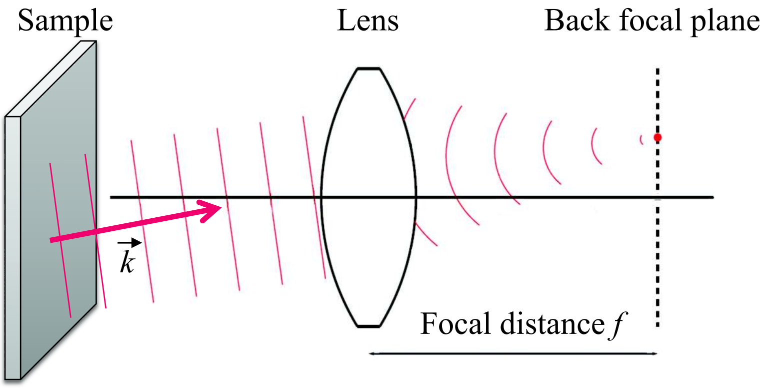

Figure 3.1: Fourier transform properties of lenses. A plane wave incident on a lens is focused into a spot with unique spatial coordinates on the back focal plane of the lens. The back focal plane is defined as the plane perpendicular to the optical axis of the lens at a focal distance.

A remarkable feature of Fourier imaging, as compared to real-space imaging, is the shift invariance property: the spatial coordinates on the Fourier plane depend only on the directionality of the emission and are independent of the distance between the source and the lens. For this reason, even if the emitter is placed out of the front focal plane of the lens, its emission pattern in the Fourier image will remain unchanged within the shift invariance range of the measurement apparatus [117]. To study the directional emission of individual nanosources we need to use microscopy techniques. In this case, the lens described above becomes a high-magnification microscope objective having the same Fourier transform properties.

3.3 Time-reversed Fourier microscopy for oblique plane wave illumination

Fourier microscopy can be used not only for studying the light emission from individual nanosources, but also for investigating their angular-dependent absorption. The basic principles of Fourier imaging microscopy presented in the previous section can be reversed by applying the reciprocity theorem [118]. Instead of imaging the BFP of the lens, we can create a point source of monochromatic light in this BFP and let the emission of this point source be transmitted through the lens. Such transmission transforms the spherical wavefronts of a point source into a plane wave. The direction of propagation of this plane wave (k-vector) depends on the position of the point source in the BFP, reciprocally to Eq. 3.3. The point source in the BFP of the lens can be created by focusing a laser beam to a spot. The control over the location of the spot in the BFP leads in a well-controlled incident angle on the sample placed in front of a microscope objective. This principle is illustrated in Figure 3.2.

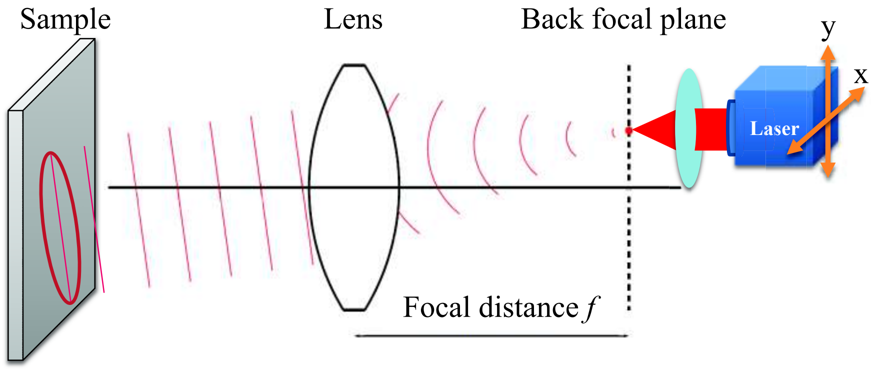

Figure 3.2: Working principle of time-reversed Fourier microscopy. A laser beam is focused to a spot at a particular position in the back focal plane of a lens, effectively creating a point source in this plane. The spherical wavefronts of the point source are transformed by the lens upon transmission into a plane wave. The direction of propagation of this plane wave, i.e., the angle of incidence on the sample, is determined by the position of the point source in the back focal plane. By controlling this position we achieve the control over the angle of incidence of the plane wave onto the sample.

The control over the angle of incidence in an optical microscope opens new fields of research. Time-reversed Fourier microscopy allows measuring angle-dependent absorption in individual nanostructures like nanowires (as shown in Chapter 6), emitters coupled to individual plasmonic nanoantennas or angular absorption enhancement in arrays of plasmonic particles for novel plasmonic-enhanced light emitting structures (discussed in Section 3.5).

3.4 Experimental realization of Fourier microscopy

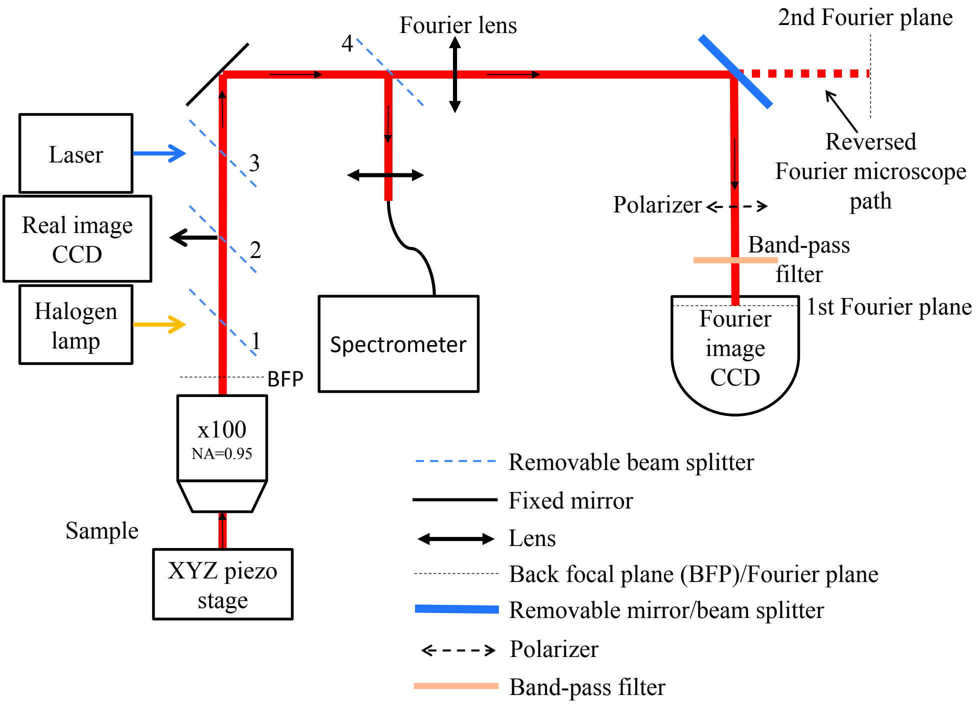

Figure 3.3: Fourier microscope setup scheme.

We succeeded in implementing the two concepts of Fourier microscopy described in the previous sections into one experimental setup. The schematic diagram of this setup is shown in Figure 3.3. As a base for the setup we used a Leica DMLM optical microscope from which we removed the ocular module. This allowed us to image the back focal plane of an objective mounted in the microscope. Instead of using the standard microscope stage, we implemented a NanoMax TS piezostage. This stage enables a precise manipulation of the sample under a microscope objective. The stage is decoupled from the body of the microscope and fixed to the optical table. The body of the microscope is supported on metal-plate spacers and fixed to the optical table with clamps. Such fixing eliminated the instability caused by the standard rubber footing of the microscope. In this way we achieved high stability necessary to perform accurate measurements on single nanostructures.

In the experiments we typically use a high numerical aperture (NA = 0.95) 100× apochromatic objective. The NA is a crucial factor for Fourier imaging as it indicates the largest possible angle of emission $\theta_{\max}$ that can be picked up by a microscope objective in a medium of refractive index n_{med},

$$\mathrm{NA} = n_{\mathrm{med}} \sin(\theta_{\mathrm{max}}). \tag{3.4}$$

The higher NA, the larger the solid angle of the emission that can be analyzed with a Fourier microscope.

For real-space imaging of the sample surface we use illumination from a halogen lamp. The light of the lamp is coupled to the microscope objective by a removable beam splitter (beam splitter 1 in Figure 3.3). Real-space images are recorded with a QImaging MicroPublisher RTV CCD camera mounted on the microscope imaging module. Light reflected from the surface of the sample can be directed to this camera with a removable beam splitter 2. For local excitation of the samples we use various laser lines coupled to the microscope objective with a removable beam splitter 3. In this way, the laser light can be focused to a diffraction-limited spot onto the sample.

Light reflected or emitted from the sample is picked up by the same microscope objective used for illumination/excitation of the sample. This light can be directed to a fiber-coupled spectrometer by the beam splitter number 4 in order to analyze the reflected/emitted spectrum.

The imaging of the back focal plane (BFP) of the microscope objective is done with the help of a lens (Fourier lens) of focal length f placed at a distance $2f$ from the BFP and $2f$ from a CCD camera. With this configuration a $1:1$ image of the BFP is projected onto the Fourier plane (1^{st} Fourier plane in Figure 3.3). This magnification ratio can be easily changed by modifying the distances between the BFP, Fourier lens and the CCD camera. The images of the Fourier plane (Fourier images) are recorded with the Andor Luca S EMCCD detector (marked in Figure 3.3 as Fourier image CCD). This detector has 468 pixels in vertical direction and 658 pixels in the horizontal direction. The pixel size is $8\mu\mathrm{m}\times 8\mu\mathrm{m}$. The size of the Fourier image for 100× objective is less than 250 × 250 pixels. The integration time is adjusted according to the intensity of excitation and the emission of the sample. In case of the basic Fourier imaging, we typically use a mirror to direct light to the Fourier camera (see Figure 3.3, 'Removable mirror/beam splitter').

To isolate the desired emission from the excitation wavelength, the Fourier images were measured after being transmitted through a band pass filter. Due to the chromatic aberrations of the Fourier lens and other optical components, the position of the Fourier lens needs to be readjusted for different band pass filters. In practice, this readjustment is done by obtaining the sharpest possible Fourier image, e.g. from a diffraction grating. The same procedure holds when a polarizer is used to determine the polarization of light emitted from the sample. The polarization analysis of Fourier images is explained in detail in Section 3.4.2.

The mirror used to direct light into the Fourier camera ('Removable mirror/beam splitter' in Figure 3.3) can be replaced by a beam splitter or removed opening the path of time-reversed Fourier microscopy for plane wave illumination. In our experimental setup we create a point source in the 2^{nd} Fourier plane by focusing a laser beam to a spot in this plane. The 2^{nd} Fourier plane is then imaged by the Fourier lens on the BFP of the microscope objective, which results in plane wave illumination of the sample placed under this objective. The laser and the lens focusing the beam on the 2^{nd} Fourier plane are mounted on a computer-controlled scanning stage. This stage provides a precise control of the position of the laser in two dimensions in the Fourier plane. Therefore, we can easily change the location of the spot focused in the Fourier plane and thus control the angle of incidence on the sample. The emission of the sample excited in this way can be analyzed by all means described above, including Fourier imaging when a beam splitter is used to direct light into the Fourier camera.

3.4.1 Emission angle in Fourier images

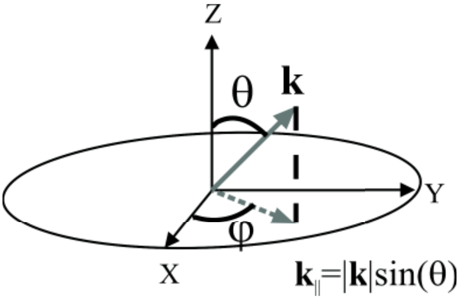

Figure 3.4: Coordinate system of the directional emission. The circle represents the emitting surface of the sample lying in x-y plane. Light is picked up by the optical system in z-direction. The wave vector **k** (red arrow) indicates a plane wave emitted in a particular direction, described by angles θ and φ. The red dashed line indicates the component of **k** in plane of the sample ($\mathbf{k}_\parallel = |\mathbf{k}|\sin(\theta)$).

Each wave vector of emission **k**, is characterized by two angles of the emission: the elevation angle θ and the azimuthal angle φ. The definition of these angles is illustrated in Figure 3.4. The sample area is represented by the circle in the x-y plane. Light emitted out of this plane toward positive z is coupled to a microscope objective and Fourier-transformed onto its BFP that we image on a CCD camera.

A raw Fourier image is an intensity map of the directional emission from the sample. This means that each pixel in the Fourier CCD camera corresponds to a unique $k-$vector of the emission. Since we project the $k-$vectors emitted in 3D space on the BFP of the objective, the coordinates (x, y) in the BFP are proportional to the parallel component of the wave vector $\mathbf{k}_\parallel$:

$$rA = \mathbf{k}_\parallel = |\mathbf{k}|\sin(\theta) = n_{\text{med}}\frac{2\pi}{\lambda}\sin(\theta), \tag{3.5}$$

where $r = \sqrt{x^2 + y^2}$ is the distance from the center of the Fourier image, A is a proportionality factor between r and $\mathbf{k}_{\parallel}$, λ is the wavelength of the emitted light and n_{med} is the refractive index of the medium surrounding the sample and the objective. To display the Fourier images in terms of the emission angles θ and φ we apply the following transformation. The BPF of the objective recorded by the Fourier camera appears as a disc. The center of this disc corresponds to light emitted from the sample along the z-axis in Figure 3.4 ($\mathbf{k}_{\parallel} = 0$, $\theta = 0°$). The edge of the disc corresponds to the maximum collected elevation angle of the emission θ_{max} determined by the NA of the objective according to Eq. 3.4. The proportionality factor A in Eq. 3.5 is then

$$A = \frac{|\mathbf{k}|}{r_{\text{max}}} \sin(\theta_{\text{max}}) = \frac{k_0}{r_{\text{max}}} \text{NA}, \tag{3.6}$$

where $k_0 = \frac{2\pi}{\lambda}$. After substituting A into Eq. 3.5 we obtain the following expression for the elevation angle of the emission

$$\theta = \arcsin\left(r \frac{\frac{k_0}{r_{\text{max}}} \text{NA}}{n_{\text{med}} k_0} \right) = \arcsin\left(r \frac{\text{NA}}{r_{\text{max}} n_{\text{med}}} \right). \tag{3.7}$$

The azimuthal angle of the emission is given by

$$\varphi = \arctan\left(\frac{k_{\text{y}}}{k_{\text{x}}} \right) = \arctan\left(\frac{y}{x} \right). \tag{3.8}$$

Equations 3.7 and 3.8 relate the spatial coordinates in the Fourier plane to the emission angles.

Figure 3.5(a) presents the Fourier image of light reflected from a two-dimensional diffraction grating. This grating is formed by a square array of gold particles spaced with a pitch of $a = 500$ nm. We illuminated the grating with the white light of the halogen lamp in the microscope. Such illumination provides the full range of incident angles supported by the NA of the objective. To record sharp diffraction features in the Fourier image we placed a band-pass filter in front of the Fourier camera. The transmission band of this filter was centered at $\lambda = 532$ nm and had a bandwidth of 10 nm. The bands of low reflection (dark bands) in Figure 3.5(a) arise from the coupling of the incident light to diffracted orders in plane of the grating ($\theta_{\text{out}} = 90°$), that is, Rayleigh anomalies. The angles at which the incident light couples to Rayleigh anomalies can be calculated from the grating equation:

$$\mathbf{k}_{\text{out}} = \mathbf{k}_{\text{in}} + m_{\text{x}} \mathbf{G}_{\text{x}} + m_{\text{y}} \mathbf{G}_{\text{y}}, \tag{3.9}$$

where $\mathbf{k}_{\text{out}}$ and $\mathbf{k}_{\text{in}}$ are the out- and incoming plane wave $k-$vectors, m_{x} and m_{y} are the integers defining the order of the diffraction in the two lattice directions and $\mathbf{G}_{\text{x}}$ and $\mathbf{G}_{\text{y}}$ are the reciprocal lattice vectors given by

$$\mathbf{G}_{\text{x}} = \frac{2\pi}{a_{\text{x}}} \hat{\mathbf{e}}_{\text{x}} \tag{3.10}$$

$$\mathbf{G}_{\text{y}} = \frac{2\pi}{a_{\text{y}}} \hat{\mathbf{e}}_{\text{y}} \tag{3.11}$$

where a_x and a_y are the lattice constants and $\hat{\mathbf{e}}_x$, $\hat{\mathbf{e}}_y$ unit vectors in the x and y directions, respectively.

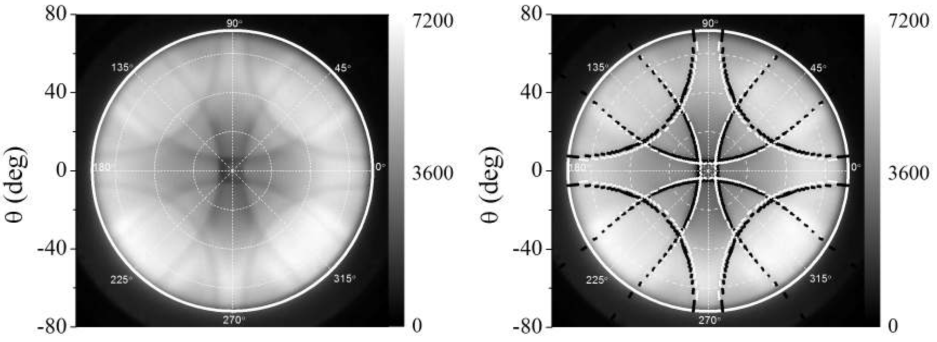

Figure 3.5: (a) Fourier image of light diffracted by a two-dimensional grating formed by an array or gold particles. The nominal pitch of this grating is $a = 500$ nm. The grating was illuminated with a standard halogen lamp illumination of an optical microscope providing all incident $k-$vectors supported by the NA of the objective. The image was recorded with a band-pass filter, whose transmission band was centered at $\lambda = 532$ nm and had a bandwidth of 10 nm. The reciprocal space linear coordinates of a raw image were transformed to (θ, φ) according to the procedure described in the text. Therefore, the image is a color polar plot in which radius represents elevation angle of emission θ and the azimuthal angle is the azimuthal angle of emission φ. The white thick circle indicates the maximum angle θ_{max} that can be collected by the microscope objective of a particular NA. Color scale represents the intensity in counts per second per pixel. (b) The same as (a), but with calculated Rayleigh anomalies of the diffraction grating with a pitch of $a = 500$ nm (white points) and $a = 490$ nm (black points).

The Rayleigh anomalies for $\lambda = 532$ nm are plotted as white points in Figure 3.5(b). The calculated angles are superimposed on top of the measured diffraction pattern of the grating. Since lattice constant of the grating is usually 2% smaller than the nominal value[1] we also plot the Rayleigh anomalies for a grating with a pitch of $a = 490$ nm (black points). The calculations are in perfect agreement with the measured diffraction pattern.

3.4.2 Polarization analysis in Fourier microscope

The Fourier microscope is equipped with a polarizer in front of the Fourier imaging CCD camera. This polarizer makes it possible to distinguish between s- and p-polarized emission. Figure 3.6 describes the polarization analysis in the Fourier setup. The electric field vector of the p-polarized emission (green arrows) lies in the plane containing the wave vector of the emission (single red arrows) and the normal to the sample surface. The s-polarized emission is characterized by the electric field vector perpendicular to that plane (blue arrows). After reaching a microscope objective, the electric field

---

[1] The grating was made by substrate conformal imprint lithography [76]

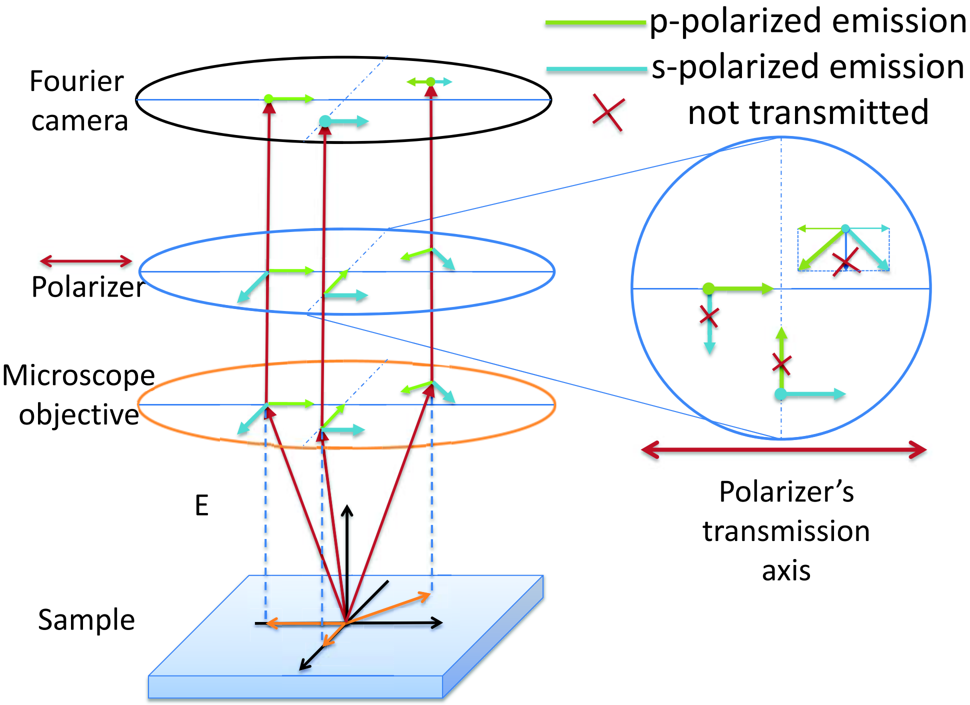

Figure 3.6: Polarization of the emission in the Fourier microscope. A linear polarizer placed in front of the Fourier camera provides that the profile of the image along the diameter that is parallel to the transmission axis of the polarizer contains purely p-polarized emission. The diameter profile of the same image that is perpendicular to the transmission axis of the polarizer contains purely s-polarized emission. All other diameter profiles contain a superposition of s- and p-polarized emission. The same principle holds for the polarization of light focused in the BFP for plane wave illumination.

vectors of the emission are projected on the plane perpendicular to the sample surface normal. By using a linear polarizer, the electric field component perpendicular to the transmission axis of the polarizer (double red arrow) is not transmitted. The only light transmitted along the diameter parallel to the transmission axis is p-polarized, while along the diameter perpendicular to the transmission axis of the polarizer only s-polarized emission is transmitted. The transmitted light along every other azimuthal direction, is a superposition of the s- and p-polarized emission. The images for unpolarized light are the sum of the images taken with two orthogonal polarizations.

Similarly, we can control the polarization of an incident plane wave in the time-reversed Fourier microscope. If we use a linear polarizer to polarize the laser beam focused onto the BFP of the objective, the spot focused on the diameter of the BFP parallel to the polarizer's transmission axis will result in a p-polarized plane wave incident on the sample. If the laser light is focused on a diameter perpendicular to the transmission axis of the polarizer, the resulting plane wave illuminating the sample will be s-polarized.

3.4.3 Intensity recorded in Fourier images

Due to the polarization-dependent transmission of the optical components used in the time-reversed Fourier microscope, the p- and s-polarized emission in the Fourier images of an azimuthally-isotropic source show different intensities. An example of such source is a Lambertian emitter, whose azimuthally-isotropic intensity emitted in direction θ is proportional to $\cos(\theta)$. This is a good approximation for the emission of a flat, high-refractive index semiconductor material such as InP, as it is derived in Ref. [119]. We reproduce here this derivation. As light is generated in a high-refractive index material, such as InP, it refracts upon transmission through InP/air interface according to Snell's law,

$$n_{\mathrm{InP}} \sin(\theta_{\mathrm{InP}}) = \sin(\theta_{\mathrm{air}}), \tag{3.12}$$

where $\theta_{\mathrm{InP/air}}$ are the incident angle in InP and the refracted angle in air measured from the normal to the interface. Due to the high refractive index mismatch at the InP/air interface, only light incident from the InP side at angles $\theta_{\mathrm{InP}} < \arcsin(\frac{1}{n_{\mathrm{InP}}})$ can be transmitted. Larger angles undergo total internal reflection and are trapped in InP. The critical angle for total internal reflection in InP is $\theta^{c}_{\mathrm{InP}} \approx 0.292$ radians (17°). Therefore, in Eq. 3.12 we can approximate $\sin(\theta_{\mathrm{InP}}) \approx \theta_{\mathrm{InP}}$. After differentiating Eq. 3.12 with respect to θ_{air} we obtain

$$\mathrm{d}\theta_{\mathrm{air}} = \frac{n_{\mathrm{InP}}}{\cos(\theta_{\mathrm{air}})} \mathrm{d}\theta_{\mathrm{InP}}. \tag{3.13}$$

Energy conservation requires that the optical power emitted into the angle $\mathrm{d}\theta_{\mathrm{InP}}$ in InP equals the optical power emitted into angle $\mathrm{d}\theta_{\mathrm{air}}$ in air, as pictured in Figure 3.7,

$$I_{\mathrm{InP}}\, \mathrm{d}S_{\mathrm{InP}} = I_{\mathrm{air}}\, \mathrm{d}S_{\mathrm{air}}, \tag{3.14}$$

where $I_{\mathrm{InP/air}}$ are is light intensity (measured in units of $\frac{\mathrm{W}}{\mathrm{m}^2}$) in InP/air and $S_{\mathrm{InP/air}}$ is the surface area element corresponding to $\mathrm{d}\theta_{\mathrm{InP/air}}$ illustrated in Figure 3.7. The surface area element in air is given by

$$\mathrm{d}S_{\mathrm{air}} = 2\pi r \sin(\theta_{\mathrm{air}}) r \mathrm{d}\theta_{\mathrm{air}}. \tag{3.15}$$

By substituting Eq. 3.13 into Eq. 3.15 we obtain

$$\mathrm{d}S_{\mathrm{air}} = 2\pi r^2 \frac{n^2_{\mathrm{InP}}}{\cos(\theta_{\mathrm{air}})} \theta_{\mathrm{InP}} \mathrm{d}\theta_{\mathrm{InP}}. \tag{3.16}$$

The corresponding surface area element in InP is

$$\mathrm{d}S_{\mathrm{InP}} = 2\pi r \sin(\theta_{\mathrm{InP}}) r \mathrm{d}\theta_{\mathrm{InP}} \approx 2\pi r^2 \theta_{\mathrm{InP}} \mathrm{d}\theta_{\mathrm{InP}}. \tag{3.17}$$

The intensity emitted in InP at a distance r from the light source equals the total emitted power of the light source P_{source} normalized to the surface area of a sphere with radius r,

$$I_{\mathrm{InP}} = \frac{P_{\mathrm{source}}}{4\pi r^2}. \tag{3.18}$$

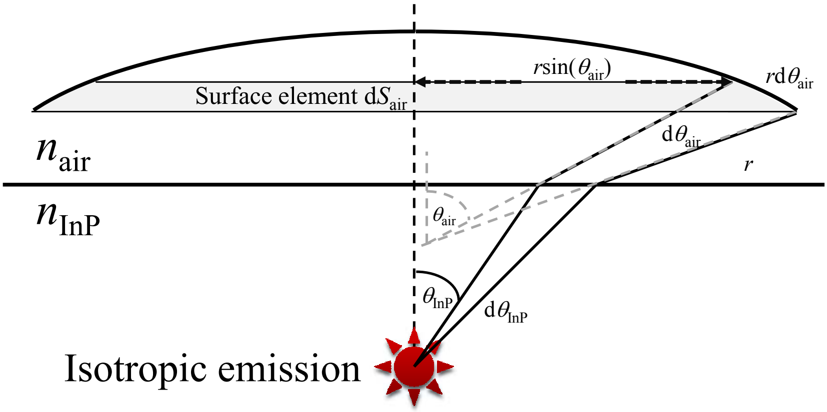

Figure 3.7: Geometry of light refraction at InP/air interface and the illustration of the surface element $\mathrm{d}S_{\mathrm{air}}$ discussed in the text. The figure is reproduced from Ref. [119].

Combining Eqs. 3.14, 3.16, 3.17 and 3.18 gives the expression for the Lambertian emission pattern measured in air,

$$I_{\mathrm{air}} = \frac{P_{\mathrm{source}}}{4\pi r^2}\frac{n_{\mathrm{air}}^2}{n_{\mathrm{InP}}^2}\cos(\theta_{\mathrm{air}}) \tag{3.19}$$

Measured polarized Fourier images of InP emission for two orthogonal orientations of the polarizer are displayed in Figures 3.8(a) and (b). The white double arrows in these images indicate the orientation of the transmission axis of the polarizer. The emission was recorded using a $\lambda = 920$ nm band-pass filter (bandwidth of 10 nm FWHM) in front of the Fourier camera. Horizontal and vertical coordinates in these images refer to pixels in the camera, whose position is related to the reciprocal space of the emission. The plots on top and on the right side of the images are their horizontal and vertical profiles, respectively. The profiles parallel to the transmission axis of the polarizer show p-polarized emission, while the profiles perpendicular to the transmission axis of the polarizer show s-polarized emission (as explained in Section 3.4.2).

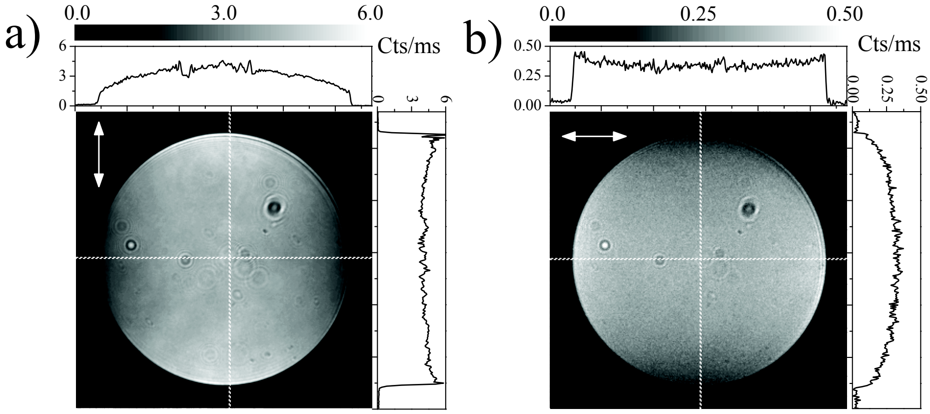

Figure 3.8: (a) An unprocessed Fourier image of the photoluminescence of an InP substrate taken using a polarizer with the transmission axis in the vertical direction. (b) A similar image recorded using a polarizer with the transmission axis in the horizontal direction. Both images were taken using a bandpass filter with a central wavelength of λ = 920 nm (bandwidth of 10 nm at FWHM). The direction of the transmission axis of the polarizer is depicted by the white double arrow. The graphs on the top and right side of the figure show the profiles of the Fourier images along the horizontal and vertical directions crossing at the center of the images.

The intensity of the emission in Fig. 3.8(a) is approximately 12 times larger than in (b). Also, the p-polarized emission is qualitatively different from the s-polarized emission. The difference between the images taken with orthogonal orientations of the polarizer varies depending on the number of beam splitters used in the setup, the alignment of the setup and the wavelength. To correct for this effect we normalize the intensities of two images to their respective maxima. After normalizing the images, we correct them such that their sum gives a Lambertian emission profile for both polarizations. The result of this correction can be appreciated in Figure 3.9(a). This figure shows the sum of two corrected, orthogonally-polarized Fourier images of the directional emission of an InP wafer (Figures 3.9(b) and (c)). In the profiles of Figure 3.9(a) we added a Lambertian emission profile that is plotted with the red dashed lines.

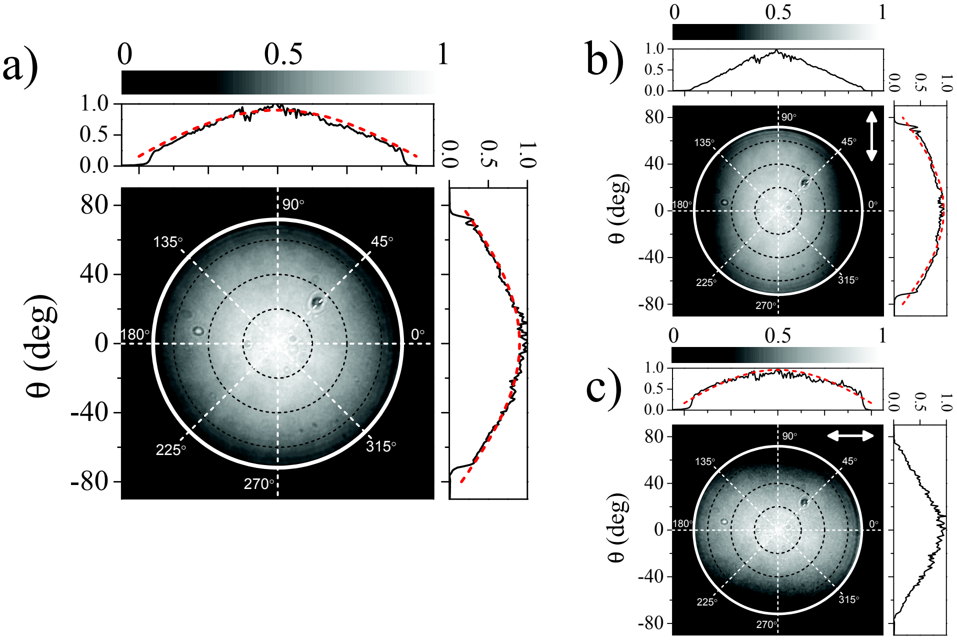

Figure 3.9: (a) Fourier image of the unpolarized photoluminescence of an InP substrate at λ = 920 nm taken using a bandpass filter with a central wavelength of λ = 920 nm (bandwidth of 10 nm at FWHM). (b) Directional emission from InP substrate taken using a polarizer with the transmission axis in the vertical direction (φ = 90° and 270°). (c) Directional emission from InP substrate taken using a polarizer with the transmission axis aligned along the horizontal direction (φ = 0° and 180°). The direction of the transmission axis of the polarizer is depicted by the white double arrow. The graphs on the top and right side of the figure show the profiles of the Fourier images along the horizontal and vertical directions crossing at the center of the images. The gray dashed lines in the profiles represent the emission of a Lambertian source. The intensity in all images was normalized to the maximum.

The intensity of Fourier images needs to be calibrated for each alignment of the setup and wavelength. This means that for measurements of the directional emission of nanowires done with a particular band-pass filter, the intensity of Fourier images is calibrated by measuring the emission of the InP wafer with the same filter.

3.4.4 Angle and intensity of illumination in time-reversed Fourier microscope

Time-reversed Fourier microscopy offers the unique possibility of illuminating individual nanostructures with a well-defined angle of incidence. As explained in Sections 3.3 and

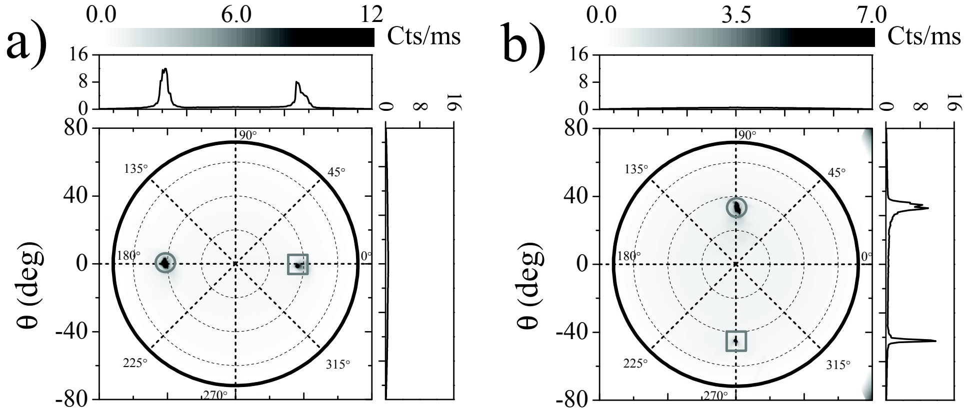

Figure 3.10: (a) Fourier image of light scattered from a square diffraction grating (pitch $a = 340$ nm) illuminated with a laser ($\lambda = 450$ nm) at $(\theta_{\text{in}}, \varphi_{\text{in}}) = (45°, 0°)$. (b) Fourier image of light scattered from the same grating illuminated at $(\theta_{\text{in}}, \varphi_{\text{in}}) = (35°, 270°)$. The specular reflection is marked with circles, whereas the (-1, 0) order in (a) and (0, -1) order in (b) are marked with squares.

3.4, to obtain a plane wave illumination with a controlled angle of incidence, we focus a laser beam on a Fourier plane of the microscope objective used in the experiment. Such a plane wave reflected from a flat surface at the sample position should result in a small spot in the Fourier image. That spot represents the Fourier transform of a beam reaching the BFP of the objective. The size of this spot is determined by the size of the laser spot focused at the Fourier plane giving rise to a small range of angles of incidence. A plane wave incident on a diffraction grating will result in diffracted orders in the Fourier image. To demonstrate this response we illuminated a square diffraction grating made by substrate conformal imprint lithography [76] (pitch $a = 340$ nm) with a laser ($\lambda = 450$ nm) at two different angles. Figures 3.10(a) and (b) show the Fourier image of light scattered from the grating illuminated at $(\theta_{\text{in}}, \varphi_{\text{in}}) = (45°, 0°)$ and at $(\theta_{\text{in}}, \varphi_{\text{in}}) = (35°, 270°)$, respectively. The zeroth order of diffraction (specular reflection) are marked with red circles, whereas the (-1, 0) order in (a) and (0, -1) order in (b) are marked with green squares. Those angular positions of diffracted orders were calculated using Eq. 3.9 and show good agreement with the measurements.

Since for obtaining a plane wave illumination we focus laser light in the Fourier plane, the position (x,y) of the focused spots is proportional to the magnitude of the $\mathbf{k}_{\parallel,\text{in}}$ (see Eq. 3.5). We apply the following alignment procedure to properly correlate the coordinates (x,y) in the Fourier plane with the angle of incidence (θ, φ).

- At normal incidence ($\theta_{\text{in}} = 0°$), light reflected from a flat InP wafer should be located in the center of the Fourier image in the CCD camera. Since in the properly aligned setup the plane wave reflected from an InP wafer appears as a small spot in the Fourier image. In this case it is helpful to use the standard halogen lamp illumination together with the plane wave illumination. The light of the halogen lamp reflected from the wafer reveals the whole NA of objective in the Fourier camera placed in the 1st Fourier plane (see Figure 3.3). In this way it is straightforward to align the normal incidence of the plane wave illumination in the center of the Fourier image of the reflected light of the halogen lamp.
- Additionally, the plane wave illumination is supposed to produce an illumination with a Gaussian profile under the microscope objective only if the focus of the laser beam in the BFP at the optical axis of the objective is symmetric with respect to this optical axis. The alignment of the setup needs to be adjusted such that the maximum intensity of the Gaussian profile is located at the optical axis of the objective and be symmetric with respect to this axis. This maximum is conveniently visible on the real space image of a photoluminescence (PL) of flat layer of emitting material excited with a plane wave.

At normal incidence these two conditions should be fulfilled simultaneously. In practice, this requires the observation of images with the real space and the Fourier cameras while adjusting the alignment of the experimental setup.

The intensity of light that propagates in the time-reversed Fourier microscope is influenced by the polarization-dependent transmission of beam splitters. If a linear polarizer is placed on the way of a circularly-polarized laser beam before it is focused to a spot in the central point of the time-reversed Fourier plane (2nd Fourier plane in Figure 3.3), the intensity of the resulting plane wave normally-incident on the sample is different for different orientations of the transmission axis of this polarizer. Additionally, another effect occurs that strongly modifies the intensity of the incident light in the center of the field of view of the microscope objective. As can be deduced from Figure 3.2, plane waves that are incident on the sample at different angles illuminate different areas of the sample. This displacement of the illumination spot as a function of the angle of incidence is illustrated in Figure 3.11. This figure shows real-space images of the PL of a flat InP wafer excited at three different angles of incidence, namely, ($\theta_{\text{in}} = 30°$, $\varphi_{\text{in}} = 0°$), ($\theta_{\text{in}} = 8°$, $\varphi_{\text{in}} = 180°$) and ($\theta_{\text{in}} = 29°$, $\varphi_{\text{in}} = 180°$). The sample was excited with a $\lambda = 532$ nm laser whose light was filtered out from the real space image by using a $\lambda > 550$ nm long-pass filter in front of the CCD camera. The maximum of the PL emission is assumed to be at the same location as the maximum intensity of the Gaussian beam that excites the InP wafer.

The PL spectrum can be analyzed in the spectrometer. Upon the proper alignment of the experimental setup, this spectrometer integrates the emission originating from a small area around the center of the field of view of the microscope objective. Because of the illumination area, the PL intensity detected by the spectrometer always decreases for

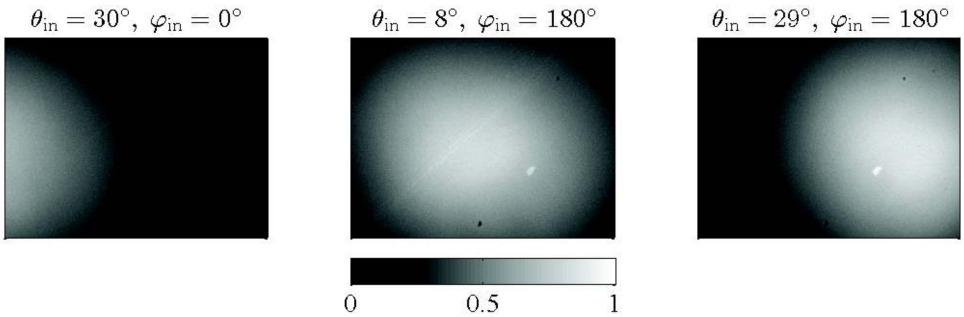

Figure 3.11: Example of the illuminating spot displacement as function of the angle of incidence. Figures show real space images of PL if a flat InP wafer illuminated at three different angles of incidence indicated above each image. The wafer was excited with a diode-pumped laser emitting at $\lambda = 532$ nm. The excitation was filtered with a $\lambda > 550$ nm long-pass filter. The color scale represents the intensity of the PL emission.

increasing angle of incidence θ_{in}. Figure 3.12(a) shows the measured intensity of the PL emission of the InP wafer (centered at $\lambda \approx 920$ nm) as a function of the angle of incidence θ for p- and s-polarized excitation (red and blue lines respectively). The PL intensity is normalized to the value at $\theta_{\text{in}} = 0^\circ$. We chose to scan the position of the laser spot in the Fourier plane along x direction (see Figure 3.2). To provide p- and s-polarized incidence, we polarized the incident light parallel and perpendicularly to the direction of the scan, respectively. Since the coupling of light to a flat InP layer is independent of φ_{in}, we plot only the results for $\varphi_{\text{in}} = 0^\circ$.

The angle of incidence- (θ_{in}) and polarization-dependent absorptance of a thick, flat InP wafer (with refractive index n_{InP}) illuminated from air ($n_{\text{air}} = 1$) can be derived from the transmittance calculated using Fresnel equations [120]

$$r_{\text{s}} = \frac{\cos\theta_{\text{air}} - n_{\text{InP}}\cos\theta_{\text{InP}}}{\cos\theta\text{air} + n_{\text{InP}}\cos\theta_{\text{InP}}} \tag{3.20}$$

$$t_{\text{s}} = \frac{2\cos\theta\text{air}}{\cos\theta\text{air} + n_{\text{InP}}\cos\theta_{\text{InP}}} \tag{3.21}$$

$$r_{\text{p}} = \frac{n_{\text{InP}}\cos\theta_{\text{air}} - \cos\theta_{\text{InP}}}{\cos\theta_{\text{InP}} + n_{\text{InP}}\cos\theta_{\text{air}}} \tag{3.22}$$

$$t_{\text{p}} = \frac{2\cos\theta_{\text{air}}}{\cos\theta_{\text{InP}} + n_{\text{InP}}\cos\theta_{\text{air}}}. \tag{3.23}$$

where θ_{air} and θ_{InP} are the angles or incidence and transmission in air and InP, respectively, related by the Snell's law (Eq. (3.12)). The transmittance and reflectance for p- or s-polarization of incident light are given by

$$T_{\mathrm{p,s}} = \frac{n_{\mathrm{InP}} \cos\theta_{\mathrm{InP}}}{\cos\theta_{\mathrm{air}}} |t_{\mathrm{p,s}}|^2, \tag{3.24}$$

$$R_{\mathrm{p,s}} = |r_{\mathrm{p,s}}|^2. \tag{3.25}$$

Due to material properties, all light with a wavelength of $\lambda = 532$ nm coupled to a thick InP wafer is completely absorbed. Therefore, the absorptance of an InP wafer equals the transmittance of air/InP interface. This calculated absorptance is shown in Figure 3.12(b) for p- and s-polarized excitation as a function of θ_{in}. The absorptance of s-polarized light is supposed to decrease with the increasing angle of incidence due to the increasing reflectance from air/InP interface. However, the absorptance of p-polarized light shows opposite behavior. This is expected for p-polarized light as the angle of incidence approaches the Brewster's angle, at which nearly all incident light of this polarization is transmitted through the interface.

The expected angle-dependent absorptance of an InP wafer calculated using Fresnel equations (Figure 3.12(a)) is qualitatively different from the measured angle-dependent excitation of the PL emission of the InP wafer (Figure 3.12(b)). This difference originates from the aforementioned polarization-dependence in the experimental setup. However, the ratio of the normalized PL emission intensity excited with s- and p-polarized light for the same scanning direction should cancel artifacts related to the polarization-dependent transmittance of the optical elements in the experimental setup. This ratio can be appreciated as black open circles in Figure 3.12(c) and it can be used to calibrate the angle of incident plane wave. The top axis in the figure indicates the position of the focused laser spot in the 2nd Fourier plane. Knowing that the maximum of the PL ratio corresponds to normal incidence, we can fit this experimental ratio with the ratio of s- and p-polarized light absorptance calculated from the Fresnel equations. The fitted theoretical ratio of s- and p- polarized absorptance in InP as a function of the angle of incidence is represented by the black solid line in Figure 3.12. Upon this fitting we can relate the positions of the laser spot in the 2nd Fourier plane to the angle of incidence by Eq. 3.7 and find the proportionality factor A. The determination of this factor allows us to associate each position of the focused laser spot in the 2nd Fourier plane to an angle of incidence.

To calibrate the incident intensity, for each scan direction and incident polarization we develop an instrument response function $C_{\mathrm{(s,p),(x,y)}}(\theta_{\mathrm{in}})$ that accounts for the difference between the theoretical ($A^{\mathrm{Fresnel}}_{\mathrm{(s,p)}}(\theta_{\mathrm{in}})$) and measured ($I^{\mathrm{Measured}}_{\mathrm{(s,p),(x,y)}}(\theta_{\mathrm{in}})$) values.

$$C_{\mathrm{(s,p),(x,y)}}(\theta_{\mathrm{in}}) = \frac{A^{\mathrm{Fresnel}}_{\mathrm{(s,p)}}(\theta_{\mathrm{in}})}{I^{\mathrm{Measured}}_{\mathrm{(s,p),(x,y)}}(\theta_{\mathrm{in}})} \tag{3.26}$$

This instrument response function is used to correct the measurements of samples with an unknown response.

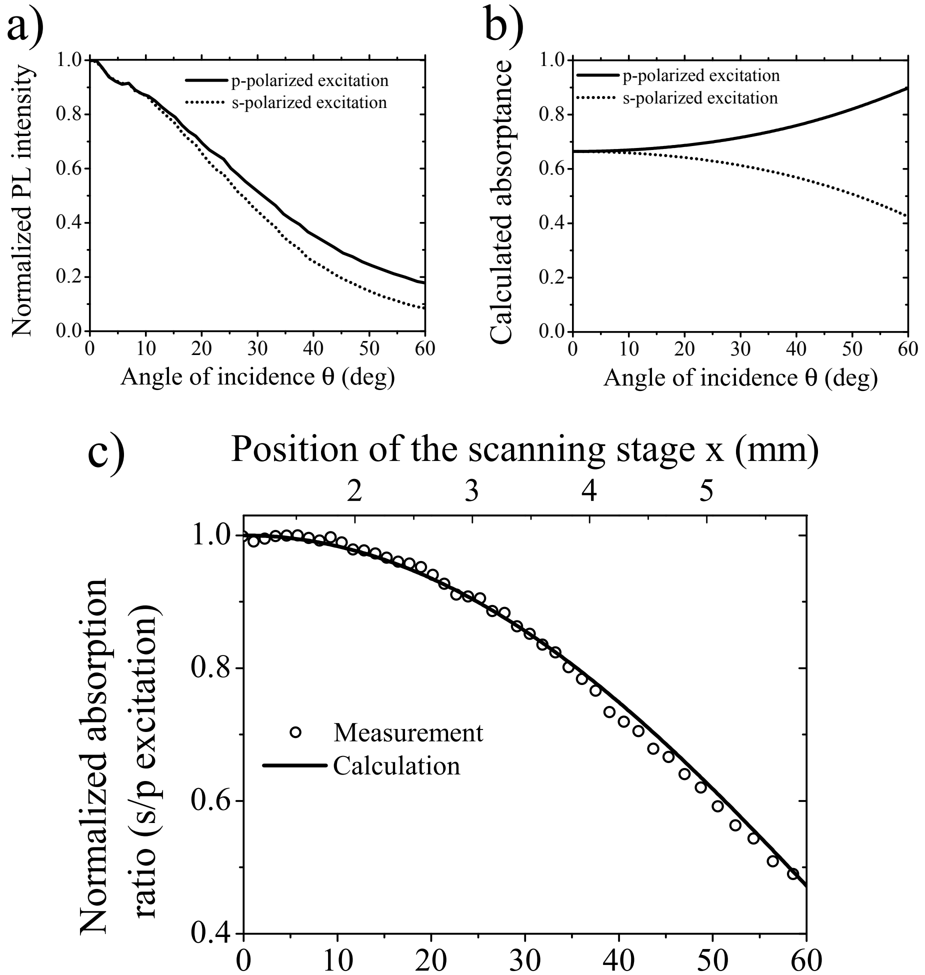

Figure 3.12: (a) Measured PL intensity of an InP wafer emitting at λ = 920 nm excited with a laser (λ = 532 nm) as a function of the angle of incidence for p- and s-polarized excitation (solid and dotted lines, respectively). The PL intensity is normalized to the values at $\theta_{\text{in}} = 0°$ (b) Calculated absorptance of an InP wafer illuminated with λ = 532 nm light as a function of the angle of incidence for p- and s-polarized excitation (solid and dotted solid lines, respectively). (c) Ratio of the measured PL intensity from InP excited with s- and p-polarized light (black open circles) compared to the ratio of the calculated absorptance of s- and p-polarized light in InP (black solid line). The upper axis in this plot represents the position of the focused laser spot in the time-reversed Fourier plane.

3.5 Applications and outlook

Fourier microscopy is applied in this thesis to investigate the angle-dependent light emission from semiconductor nanowires (Chapters 4 and 5). Naturally, the technique can be also used to study the directional emission of other nanoscale or even extended objects. The development of Fourier microscopy in our group stimulated studies of the directional emission of luminescent materials for solid-state lighting applications. In Section 3.5.1 we use Fourier imaging for a fast characterization of a large solid angle of the directional emission from luminescent materials coupled to plasmonic particle arrays. Fourier microscopy might decrease the cost of fabrication and characterization of prototypes of nanostructured light-emitting diodes (LEDs) in industrial research.

While the Fourier imaging has been a known technique (as mentioned in Section 3.1), the time-reversed Fourier microscopy that we have introduced is a new technique. Chapter 6 of this thesis discusses the use of the time-reversed Fourier microscopy for studying the angle-dependent light absorption in individual semiconductor nanowires. Besides the application to nanowire photonics, the ability of controlling the angle of incidence in an optical microscope opens many possibilities for nanophotonics in fundamental and applied research. In Section 3.5.2 we demonstrate the characterization of angle-dependent light absorption in nanostructured luminescent materials and solar cells. Based on our findings, we also propose a concept for increasing the efficiency of LEDs and solar cells.

Finally, we combine our studies on the directional emission of semiconductor nanowires with the properties of plasmonic particles array to propose the design of a highly-directional electrically-driven nanowire single-photon source. Directionality of single-photon sources can improve the collection efficiency of single photons in optoelectronic circuits which is of great interest for quantum computing.

3.5.1 Fourier microscopy for the directional characterization of light emitting devices prototypes

Directional emission is one of the key parameters to optimize the efficiency of LEDs. Commercial white LEDs consist of GaN blue LEDs that excite a luminescent material that emits light of a longer wavelength. The emission of the luminescent material combined with the blue light of GaN LEDs appears white to the human eye. Improving the emission of luminescent materials could increase the efficiency of LEDs and could reduce the amount of material necessary to provide a desired emission power in a small solid angle. The emission of luminescent material can be improved by coupling it to arrays of plasmonic nanoparticles. Each particle in such an array supports a localized surface plasmon resonance (LSPR) at optical wavelengths. The light scattered collectively by the particles in an ordered array can couple to diffraction orders supported by the periodicity of the structure. Such hybridization of a LSPR with diffraction orders in the plane of the particle array is called a surface-lattice resonance (SLR) and leads to a directional optical response of the particle array [121, 122]. While the electric field of the LSPR is concentrated in the close proximity to the plasmonic particle, the field of the SLRs extends in the volume between the particles [123]. If such particle array is close to a luminescent material, the light emitted by this material can excite the SLRs in the array. These SLRs radiate into free-space at the directions determined by the periodicity of the array and the size of the particles. In this way, the intensity emitted from the luminescent material in particular directions can be 20-fold enhanced compared to the emission of similar planar layers without plasmonic arrays [124].

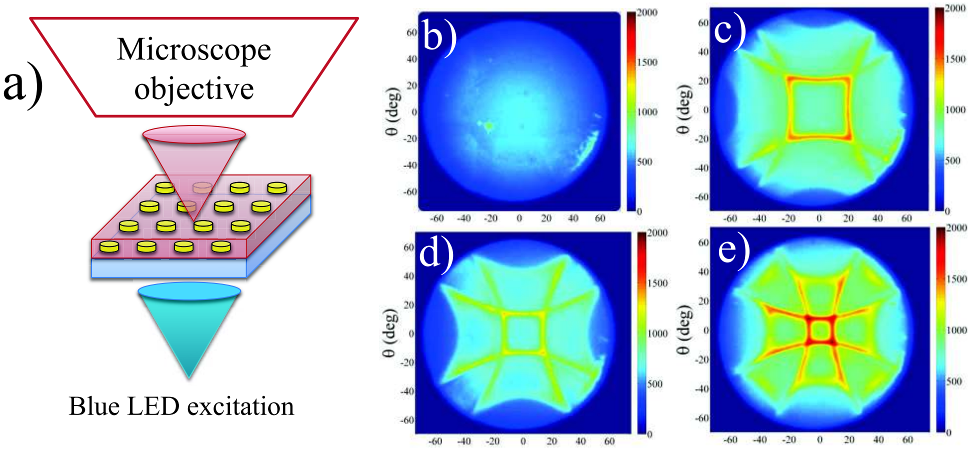

Figure 3.13: (a) Schematics of the experimental configuration. A light-emitting material is excited with a blue LED (λ = 450 nm) from below. The emission of the light-emitting material is collected by a microscope objective in a Fourier microscope. (b) The unpolarized Fourier image of the directional emission of a planar layer of a luminescent material (Lumogen F Red 305 dye). (c), (d), and (e) show the Fourier images of the emission of the same luminescent material on top of square arrays of Al plasmonic particles with a pitch of 330 nm, 350 nm and 370 nm, respectively. The emission was collected with a 100× microscope objective with the NA of 0.95 providing the maximum collected emission angle of $\theta = 72°$. All the Fourier images were recorded with a band-pass filter centered at $\lambda = 600$ nm and the transmission band of 10 nm at FWHM.

The directional emission can be controlled by the geometry of the plasmonic particle array. Optimization of this emission requires fabrication of particle arrays with different particle size, shape and pitch. Standard techniques used for the characterization of the directional emission, such as rotation stage technique, require at least few-millimeters large samples. Large-area particle arrays can be fabricated either by the electron-beam lithography (e-beam), or by the nanoimprint lithography (see Section 1.2). While the nanoimprint lithography reduces the replication cost of large-area particle arrays, any new array design requires a separate nanoimprint template made by the e-beam lithography. However, measuring the directional emission using Fourier microscopy does not require large-area samples. Even particle arrays smaller than the field of view of a high-magnification microscope objective (about $100 \times 100\ \mu\text{m}^2$) can be used for characterization of nanostructured LEDs. Therefore, Fourier microscopy is potentially interesting for the design and optimization of novel nanostructured LEDs.

To demonstrate the usefulness of the Fourier microscope for industrial applications, we have measured the directional emission of luminescent materials enhanced by a plasmonic array. Figure 3.13(a) shows the schematics of the measurements. In this figure, a layer of a luminescent material (Lumogen F Red 305 dye suspended in a polymer matrix) deposited on top of an array of plasmonic particles is excited with a blue light of a GaN LED ($\lambda = 450$ nm) located below the array. The light emitted by the luminescent material is then collected by an objective in the Fourier microscope to produce the Fourier images of the directional emission. The Fourier image of the unpolarized directional emission of a planar layer of the luminescent material without any particle array is shown in Figure 3.13(b). This Fourier image was taken with a band-pass filter centered at $\lambda = 600$ nm and a transmission band of 10 nm at FWHM. This emission resembles a Lambertian emission profile, where the maximum intensity is emitted normally to the surface of the layer. The emission of the same layer of the luminescent material on top of a square array of Al plasmonic particles with a diameter of $d = 100$ nm and a pitch of 330 nm can be appreciated in Figure 3.13(c). Clearly, the Fourier image is different from the Lambertian emission and shows a fourfold symmetry attributed to the symmetry of the particle array. This emission pattern can be further modified by changing the pitch of the particle array. Figures 3.13(d) and (e) display the Fourier images of the luminescent material emission coupled to particle arrays of pitch 350 nm and 370 nm, respectively. As the pitch of the array increases, the light is emitted at smaller angles and the emission becomes more intense. All Fourier images in Figure 3.13 have been recorded with the same band-pass filter and share the same color scale. The microscope objective used in the experiments had a magnification of 100× and the NA of 0.95 providing the maximum collected emission angle of $\theta = 72°$. The different particle arrays have been fabricated by means of nanoimprint lithography on the same substrate. Recording the Fourier images of the emission required only translating the sample under the microscope objective. In this way, the fast characterization of a large-solid-angle emission of different particle arrays was enabled.

We have shown that Fourier microscopy can be used for a convenient and fast characterization of the directional emission of light-emitting materials. Due to the use of high-magnification microscope objectives, the size of the samples can be kept small, reducing the cost of designing and optimizing nanophotonic structures.

3.5.2 Time-reversed Fourier microscopy for the optimization of absorption in luminescent materials and solar cells

The efficiency of light absorption is important for novel LEDs and solar cells. Optimization of the light absorption will allow using less expensive materials to attain the same device efficiency and, therefore, will lead to the reduction of the cost of the devices. The most common optoelectronic devices are based on planar structures with a directional response that is azimuthally-symmetric. However, novel designs for solid-state lighting and photovoltaics employ nanostuctures, such as ordered arrays of nanoparticles, that can break the azimuthal symmetry of the devices. In this case, investigations of the angle-dependent light absorption can provide a valuable knowledge for increasing the performance of such devices. This section presents the application of the time-reversed Fourier microscopy to study the directional light absorption in luminescent materials on top of arrays of metallic particles. Based on our findings, we suggest the way to increase the absorptance of these materials.

Ordered arrays of plasmonic particles can support SLRs, as pointed out in Section 3.5.1. The SLRs are able to shape the directional emission of luminescent materials. However, the plasmonic particle arrays can also enhance the directional absorption of the same materials by coupling the incident light to SLRs [122]. Using the time-reversed Fourier microscope we have measured the angle-dependent light absorption in a layer of luminescent material (Lumogen F Red 305 dye suspended in a polymer matrix) enhanced with an array of Al plasmonic particles (diameter d = 100 nm, pitch of 340 nm). The absorption is probed by analyzing the emission intensity that is directly proportional to the absorptance in the luminescent material, similar as in Chapter 6. The material is excited with a polarized diode-pumped laser (λ = 532 nm) through a 100× microscope objective with the NA of 0.95 (see Figure 3.14(a)). The emission of the material is dispersed in a spectrometer and integrated between λ = 645 and 655 nm for each angle of the excitation. Figure 3.14(b) shows the map of the directional excitation of the luminescent material normalized to the directional excitation map of the material without plasmonic particles. This map shows absorption features attributed to the SLRs. The asymmetry in these features origins from the polarization-dependent response of the array. This measurement reveals that for certain angles of excitation (especially close to the normal incidence on the sample - center of the map), the absorption is up to 4 times more efficient than in the same layer of the material without the plasmonic particles. Therefore, the performance of the devices based on similar plasmonic arrays (or any materials showing the angle-dependent absorption) can be optimized by matching the excitation to the response of the sample. This concept is represented in Figure 3.14(c). In this figure a standard LED excitation of a luminescent material is altered by an optical element. This element, e.g. a diffraction grating, is supposed to provide the angular redistribution of the excitation to obtain the maximum absorption in the sample.

The implementation of electrical probes and a source meter unit in the time-reversed

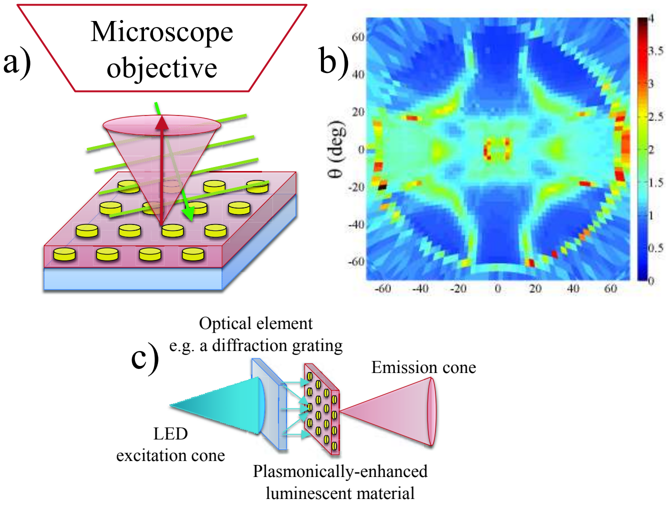

Figure 3.14: (a) Schematic representation of the experimental configuration. A light-emitting material is excited with a plane wave using a time-reversed Fourier microscope (diode-pumped laser, λ = 532 nm, represented by the green wavefronts and the green arrow). The emission of the light-emitting material is collected by a microscope objective in a Fourier microscope and coupled to a spectrometer. (b) The photoluminescence intensity of the plasmonically-enhanced luminescent material as a function of the angle of excitation. For each angle of excitation (each pixel in the image), the photoluminescence of the sample is analyzed by a spectrometer and integrated between λ = 645 and 655 nm. The results are normalized to the emission of the same material without the plasmonic particles. Therefore, the color scale represents the photoluminescence enhancement due to directional absorption enhancement. The emission was excited and collected with a 100× microscope objective with the NA of 0.95 providing the maximum excitation angle of $\theta = 72°$. (c) The concept of increasing the performance of luminescent material. The excitation of a plasmonically-enhanced luminescent material is shaped by an optical element that redistributes the excitation intensity in particular directions. These directions match the angular response of the luminescent material leading to an increased absorption when compared to the standard excitation.

Fourier microscope could also allow the measurements of the angle-dependent photocurrent. The photocurrent can be used to characterize the angle-dependent absorption in novel photovoltaic devices, such as solar cells based on arrays of semiconductor nanowires. Similarly, the light absorption in nanowire solar cells could be improved by shaping the angular range of light incident on a device.

In conclusion, we have demonstrated that the time-reversed Fourier microscopy is a novel powerful technique to study the angle-dependent absorption in nanophotonic systems.

3.5.3 Highly-directional electrically-driven nanowire single-photon-sources

The work on Fourier microscopy and the directional emission of nanostructures inspired us with ideas related to solid state single-photon sources based on nanowires. Since the actual single-photon emitters are of the size of nanometers and very localized in space, their emission is isotropic and needs to be channeled in order to optimize the collection efficiency of single photons in optical circuits. It has been shown that semiconductor nanowires can work as optical antennas to tailor the spontaneous emission of single-photon sources embedded in nanowires [24], can be electrically-driven nanowire lasers [7], LEDs [125] or even sources of surface plasmons [126]. Very recently, the first electrically-driven single-photon sources embedded in semiconductor nanowires have been demonstrated [29]. In view of these advances, we propose a design combining such source of single photons with arrays of plasmonic particles supporting the SLRs (as discussed in Section 3.5.1). It has been shown that the spontaneous emission of semiconductor nanowires can be coupled to surface plasmons [127]. However, the propagating surface plasmons suffer from the Ohmic losses in a metal. The coupling of single-photon emission generated in semiconductor nanowire-based sources to SLRs could reduce the Ohmic losses. As a result, the system of nanowire-based single-photon source coupled to an array of plasmonic particles could work as a delocalized source of single photons. Figure 3.15 displays the concept of such integrated system. In this figure, the electrically-driven emission of a single-photon source embedded in the nanowire is guided in the nanowire. When this emission reaches the end facets of the nanowire, it can couple to particle arrays that support the SLRs and provide directional redistribution of single photons. The directionality of the light emission of such a delocalized single-photon source can be controlled by tuning the geometry of the particle array, as demonstrated in Section 3.5.1. This concept might lead to obtaining highly directional sources of single photons for quantum computing.

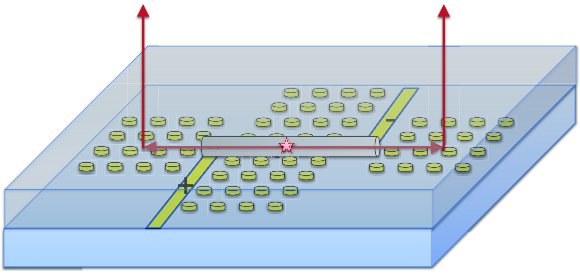

Figure 3.15: The illustration of an electrically-driven single-photon source embedded in a semiconductor nanowire coupled to arrays of plasmonic particles. The red arrows represent the direction of the light propagation. The emission of a single-photon source is guided in the nanowire to its end-facets and there it couples to arrays of plasmonic particles. The SLRs supported by the particle arrays provide the angular redistribution of the single-photon emission.

3.6 Conclusions on Fourier microscopy

In this chapter we have described the principles of Fourier imaging microscopy and the time-reversed Fourier microscopy. We have also presented a successful implementation of both concepts of Fourier microscopy in one, self-developed experimental setup and thoroughly discussed the calibration of this setup. Our Fourier microscope is a unique instrument that allows the investigation of the directional light emission and absorption of individual nanostructures. The described features of the setup were used to obtain the experimental results presented in the next chapters of this thesis.

CHAPTER 4

NANOWIRE ANTENNA EMISSION

We experimentally demonstrate the directional emission of polarized light from single semiconductor nanowires. The directionality of this emission has been directly determined with Fourier microphotoluminescence measurements of vertically oriented InP nanowires. Nanowires behave as efficient optical nanoantennas, with emission characteristics that are not only given by the material but also by their geometry and dimensions. By means of finite element simulations, we show that the radiated power can be enhanced for frequencies and diameters at which leaky modes in the structure are present. The radiated power can be also inhibited at other frequencies or when the coupling of the emission to leaky modes is not favored. We anticipate the relevance of these results for the development of nanowire photon sources with optimized efficiency and/or controlled emission by the geometry.

4.1 Introduction

The directionality of the light emission plays a key role in the design of efficient light sources [128–131]. The angular redistribution of light emitted by, e.g, a Lambertian source can increase the radiance of such source defined as the power emitted in a certain direction into unit solid angle and normalized to the area of the emitting surface. As a result, the optical power of a source can be used more effectively by directing it into a desired solid angle. Therefore, the control of the directionality of the emission will improve the performance of devices such as light emitting diodes, nanolasers or single photon sources. In this regard, recent progress in nanofabrication techniques has led to an increased interest in the optical properties of novel structures with the dimensions comparable to the wavelength of visible and near-infrared light. Structures of these dimensions can exhibit strong light-matter interaction that helps to control light. Among those nanostructures, semiconductor nanowires have shown vast possibilities to enhance light absorption and to control the polarization and the wavelength of the light emission. The bottom-up fabrication process has enabled the growth of semiconductor nanowires on top of various materials despite of a mismatch in the crystal lattice parameter [13, 15]. This property brought interesting heterostructures to life, such as superlattices [11], radially stacked quantum wells [132], individual nanowire lasers [79, 133], nanowire photonic crystal lasers [20] or single photon emitters embedded in nanowires [24, 27]. Due to their geometry, nanowires show anisotropic optical properties. The evidence of such behavior was found in the polarization-dependent absorption cross section and the light emission from nanowires [37]. Those phenomena have been described in the context of guided modes in finite nanowires, [44] and Mie resonances in infinitely long cylinders [77, 134, 135]. The same properties enable the increase of the absorption by nanowires and their potential use as solar light absorbers in photovoltaic applications [39, 41]. This resonant response in the absorption of nanowires has been ascribed to a nanoantenna-like response in the nanostructures. However, an antenna behavior implies not only a resonant behavior but also a directional response. Due to their finite length, semiconductor nanowires can form cavities in which guided modes can lead to lasing [8]. By analyzing the interference pattern of the emission from the end-facets of nanowires, the highly diffractive emission from the subwavelength facets was established [16]. Waveguide modes are also responsible for shaping the emission from luminescent nitrogen-vacancy centers in diamond nanowires [136]. The directionality of the emission from nanowires has been theoretically studied [80, 137].

In this chapter, we present the first demonstration of the directional photoluminescence emission from vertical nanowires. The measurements have been done on individual InP nanowires using Fourier microscopy. Semiconductor nanowires behave as true nanoantennas with a directional emission of polarized light. As in RF antennas, the directionality is determined by the geometry and dimensions of the radiating structure [138, 139]. Simulations of the emission of an oriented dipole in the nanowires reveal its coupling to leaky modes, giving rise to the directional far-field emission pattern. We also show that a dipole oriented perpendicular to the axis of the nanowire produces a qualitatively and quantitatively different emission pattern than the one produced by a dipole oriented parallel to the axis. Besides of the directionality, the nanowire modifies the local density of optical states (LDOS) to which the radiating dipole can decay. This leads to an increased emission efficiency of a dipole oriented parallel to the axis of the nanowire compared to the emission of a dipole in free space. These results are of relevance for the design of single photon sources where a controlled directionality and polarization of the emission will play a key role in their integration in optoelectronic circuits.

4.2 Sample description and experimental details

We have studied individual indium phosphide (InP) nanowires grown on top of a (111) InP substrate using the vapor-liquid-solid technique in a metal-organic vapor-phase epitaxy (MOVPE) reactor [1].[1] Arrays of separated nanowires were grown by defining the positions of the gold catalyst particle using electron beam lithography. To ensure that the emission from single nanowires is not affected by their neighbors, the distance between the gold catalyst particles was set to 10 μm. The substrate with the gold particles on top was annealed at temperature $T = 660°$ for 10 minutes prior to the growth to remove the native oxide layer and the remaining organic materials from the surface of the sample. Nanowires were grown at $T = 500°$ for 25 minutes under trimethylindium (TMIn) and phosphine (PH_3) flow.

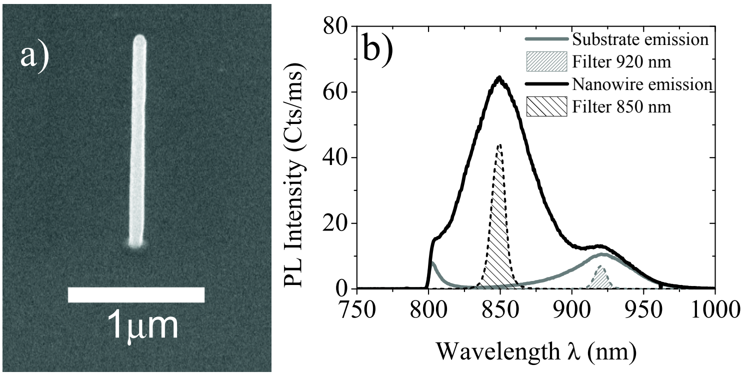

Figure 4.1: a) Scanning Electron Microscope image taken at an inclination of 30° of an InP nanowire grown on top of an InP substrate . The nanowire is 3.13 μm long and has a diameter of 100 nm. b) Photoluminescence spectra of the nanowire (black line) and the substrate (gray line), where a long-pass filter with a cut-off wavelength of 800 nm is used to filter out the scattered light from the pump laser ($\lambda = 785$ nm). The photoluminescence transmitted through a band pass filter with a central wavelength of $\lambda = 850$ nm (10 nm at FWHM) and $\lambda = 920$ nm (10 nm at FWHM) are represented by the black and gray dashed lines, respectively.

---

[1] The nanowire were grown by T. Zehender under supervision of E.P.A.M. Bakkers at Philips Research Laboratories in Eindhoven.

To ensure that the diameter of the grown nanowires is uniform along their height, a small additional flow of hydrogen chloride (HCl) was introduced together with TMIn and PH_3. The HCl provided an in situ etching of the nanowire material preventing it from forming a significant tapering [140]. As can be appreciated in the scanning electron microscopy (SEM) image shown in Figure 4.1(a), the nanowires have an average diameter of about d = 100 nm and a length of l = 3.13 μm. InP nanowires grow preferentially in a wurtzite structure on top of the zincblende InP substrate [68]. Since the electronic bandgap of InP in the wurtzite phase is larger by around 50 meV than that of zincblende, the emission peak of wurtzite nanowires is blue-shifted compared to that of the substrate [67].
A λ = 785 nm diode laser was used to excite the photoluminescence of nanowires and the substrate. The laser beam was focused to a diffraction limited spot with a ×100, NA= 0.95 objective. The photoluminescence was collected by the same objective and sent into a fiber coupled spectrometer (see Figure 3.3). Figure 4.1(b) shows the emission spectra of a nanowire and the substrate. The emission of the substrate is centered at λ = 920 nm, while the emission from the nanowires has a peak at λ = 850 nm. For the Fourier imaging measurements described next, we used bandpass filters with a center wavelength of λ = 850 nm and λ = 920 nm and a bandwidth of 10 nm to separate the emission from the nanowires from the emission from the substrate.

4.3 Directional emission of individual nanowires.

4.3.1 Measured Fourier images of nanowire emission

We have resolved the directional emission of individual nanowires using Fourier imaging microscopy (see Chapter 3). The large numerical aperture of the microscope objective (NA = 0.95) allows collecting large angles of emission limited by a marginal ray at θ_{max} = 72° from the normal to the sample.

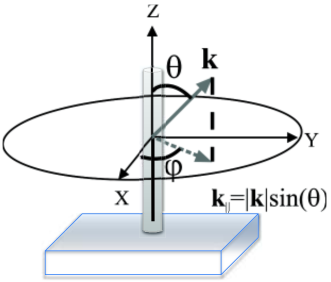

Figure 4.2: Explanation of coordinate system for nanowire antenna emission. Direction of light emission from a vertical nanowire (particular wave vector **k** depicted by gray solid arrow) can be described by two angles: elevation angle of emission θ and azimuthal angle of emission φ. In Fourier camera the $k_{\|}$ is recorded.

The Fourier images are plotted in polar coordinates, where the radius represents the elevation angle of emission θ, and the azimuthal angle φ corresponds to the azimuthal angle of the emission (see Figure 4.2). We have also analyzed the polarization of the directional emission using a linear polarizer placed on the light path just before the Fourier camera. Along the transmission axis of the polarizer only the p-polarized emission is recorded, while along the direction perpendicular to this transmission axis we detect the s-polarized emission. A detailed explanation of the polarization analysis is given in Section 3.4.2.

Figure 4.3(a) shows the Fourier images, in units of counts per second per pixel, of the unpolarized emission from a nanowire at λ = 850 nm. The Fourier images are accompanied by line plots above and on the right, that represent the profiles of the directional emission along the φ = 0° and 180° and φ = 90° and 270° directions, respectively. The measurement reveals a strong directional feature, namely, a circular emission pattern with a peak at θ = 49° for all the azimuthal angles φ. Figure 4.3(b) displays the polarized directional emission pattern. The transmission axis of the polarizer

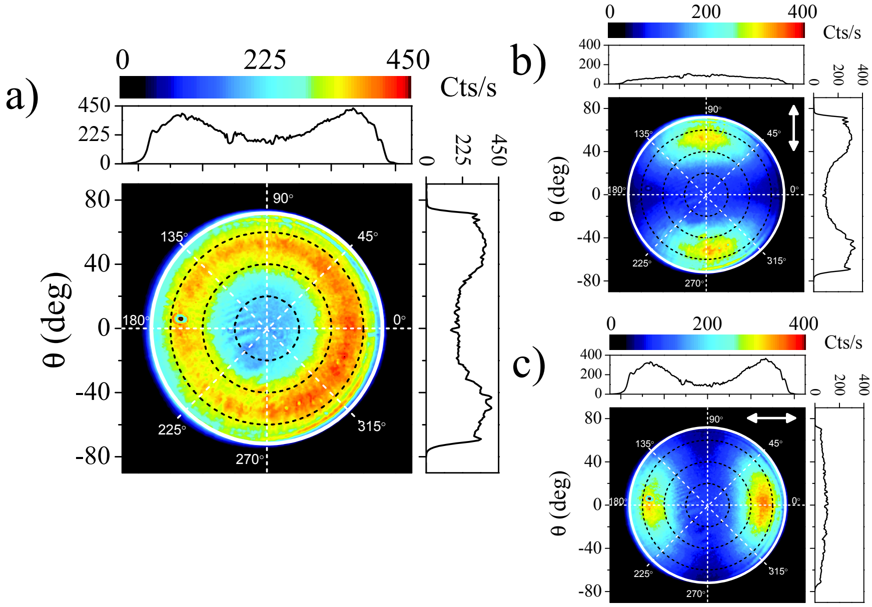

Figure 4.3: Fourier images of the emission from InP nanowires at λ = 850 nm taken using a bandpass filter with a central wavelength of λ = 850 nm (bandwidth of 10 nm at FWHM). (a) Fourier image of the unpolarized emission, (b) Fourier image taken with a polarizer with the transmission axis along the vertical direction (φ = 90° and 270°). (c) Fourier image taken with a polarizer with the transmission axis along the horizontal direction (φ = 0° and 180°). The alignment of the transmission axis of the polarizer is indicated by the white double arrow in (b) and (c). The graphs on the top and right side of each figure show the profiles of the Fourier images along the horizontal and vertical directions crossing at the center of the images.

is indicated in the figure by a white double arrow. The dominant contribution to the directional emission intensity is along the transmission axis of the polarizer, revealing that this emission is p-polarized.

The direction and polarization of the emission from nanowires is pronouncedly different from that of Lambertian emitters. To illustrate this difference, we have measured the emission from the flat InP surface by exciting it locally with the focused diode laser. We have collected the emission with the same objective and used a λ = 920 nm band pass filter to isolate this emission in the Fourier camera. As shown in Figure 4.4a, the emission pattern from the InP surface shows no particular directional features. This is expected for Lambertian sources where the emitted light is distributed equally in all directions. Also, the emission is not preferentially polarized as displayed in Figures 4.4(b) and (c). The pronounced difference between the emission of a flat surface and the emission of a nanowire, together with the directional emission of the latter, justifies the term of semiconductor nanoantennas when referring to nanowires.

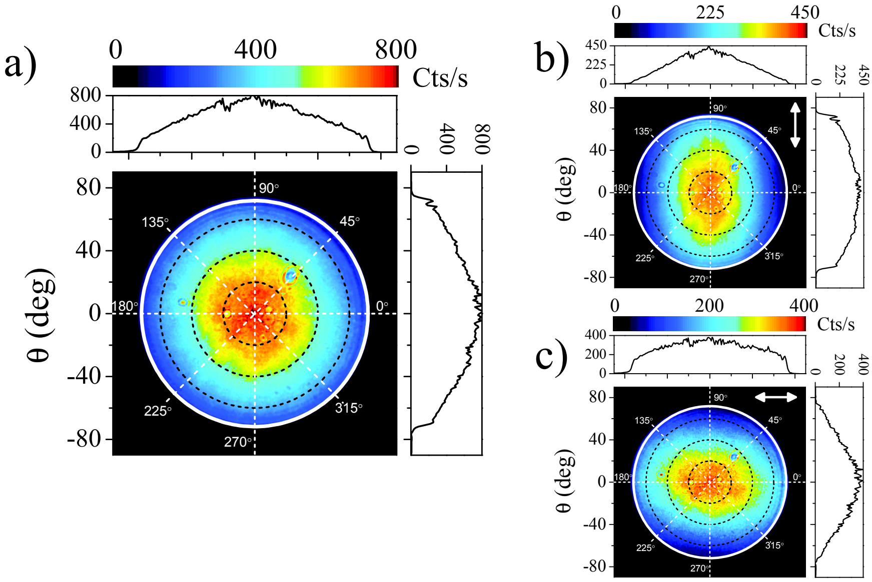

Figure 4.4: (a) Fourier image of the unpolarized photoluminescence of an InP substrate at λ = 920 nm taken using a bandpass filter with a central wavelength of λ = 920 nm (bandwidth of 10 nm at FWHM). (b) Directional emission from InP substrate taken using a polarizer with the transmission axis in the vertical direction (φ = 90° and 270°). (c) Directional emission from InP substrate taken using a polarizer with the transmission axis aligned along the horizontal direction (φ = 0° and 180°). The direction of the transmission axis of the polarizer is depicted by the white double arrow. The graphs on the top and right side of the figure show the profiles of the Fourier images along the horizontal and vertical directions crossing at the center of the images.

4.3.2 Numerical modeling of the directional emission of individual nanowires

To gain physical insight into the emission process from semiconductor nanowires, we have carried out a theoretical analysis including numerical calculations. First, we aim at reproducing the emission characteristics as close as possible to the experimental results using finite element method (FEM) simulations in the frequency domain. A cylindrical InP nanowire of diameter $d = 100$ nm and length $l = 3.13$ μm standing on top of a flat InP substrate is considered. To simulate the nanowire photoluminescence, we place three point electric dipoles with orthogonal dipole moments at the center of the nanowire and radiating at $\lambda = 850$ nm. The Fourier images are calculated by projecting the far field power emitted within a polar angle of 72° with respect to the z axis (nanowire axis) on a plane, as depicted in Figure 4.5(a).

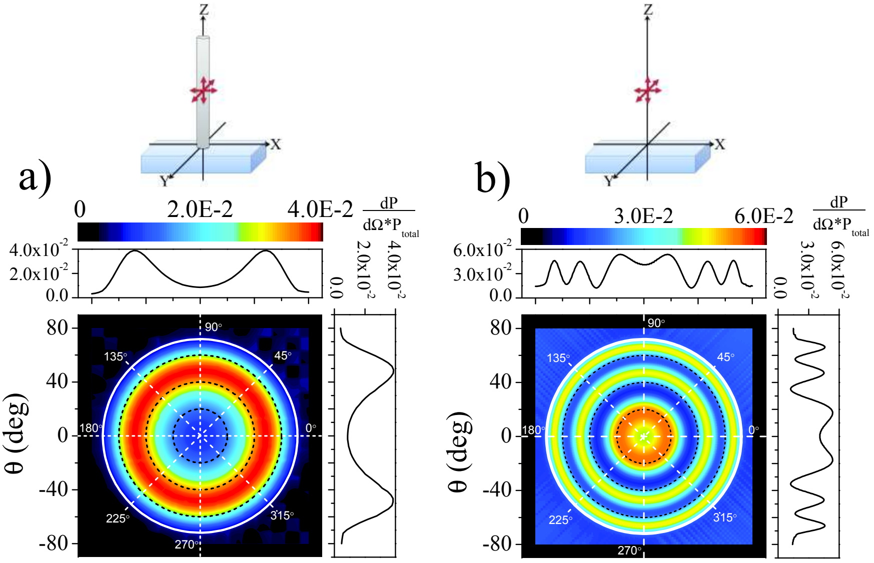

Figure 4.5: (a) FEM simulations of the unpolarized directional emission from 3 orthogonal dipoles located in the middle of the 3.13 μm nanowire standing on top of an InP substrate. The dipoles radiate at a wavelength of $\lambda = 850$ nm. (b) Simulations of the directional emission from 3 incoherently radiating orthogonal dipoles placed 1.565 μm above the InP substrate without the presence of a nanowire. On the top are schematic representations of the simulated configurations.

The calculated Fourier images represent the radiated power per unit solid angle, $\frac{dP}{d\Omega}$, normalized by the total power P_{total} emitted by a dipole in a homogeneous InP environment. The simulated Fourier image shows a ring pattern that closely reproduces the experimental result (Figure 4.3(a)). For comparison we have also calculated analytically the averaged emission pattern of three incoherently radiating point electric dipoles with orthogonal orientations at a height of 1.565 μm above the substrate, that is, without the nanowire [117]. This calculation is displayed in Figure 4.5(b). We observe an entirely different pattern consisting of few concentric fringes with a maximum at $\theta = 18°$.

We study the origin of such distinct behavior through a detailed analysis of the polarization of the emission. Figure 4.6 displays the simulations of the emission patterns for each dipole orientation. Figures 4.6(a) and (b) represent the unpolarized and polarized emissions, respectively, of the dipole oriented parallel to the nanowire axis, while (c) and (d) are the emission of the dipole oriented perpendicular to this axis.

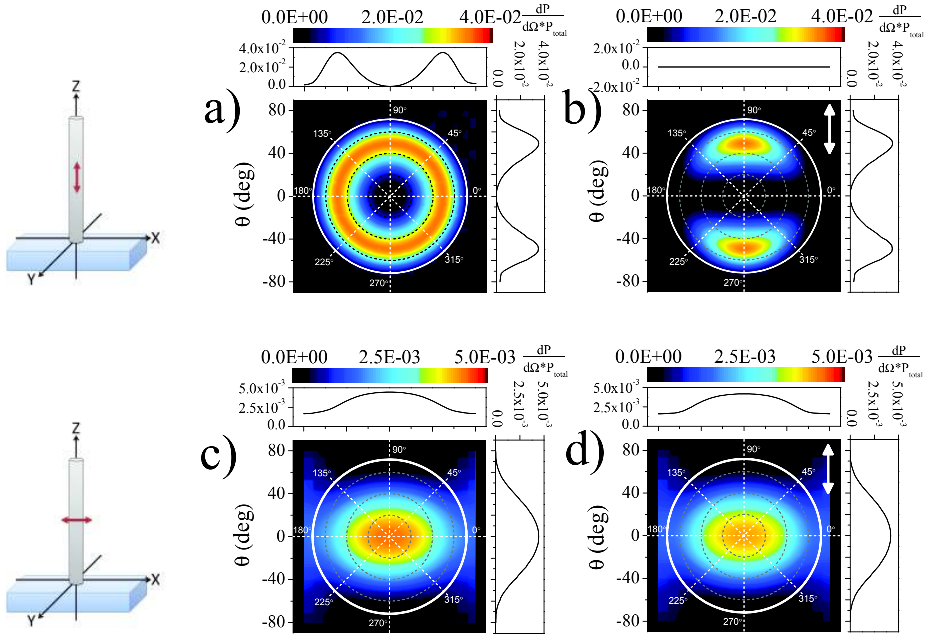

Figure 4.6: Simulations of the directional emission from a dipole located in the middle of the nanowire standing on top of an InP substrate. The dipole radiates at a wavelength of $\lambda = 850$ nm. On the left: schematics of the simulated configuration: an InP nanowire with a diameter of $d = 100$ nm and length of $l = 3.13$ μm containing a dipole with a dipole moment parallel to the long axis of the nanowire (top) and perpendicular (bottom). (a) Unpolarized directional emission pattern from the dipole oriented parallel to the axis of the nanowire. (b) Polarized directional emission of the dipole parallel to the axis of the nanowire with a polarization along the vertical direction on the image ($\varphi = 90°$ and $270°$, indicated by the white double arrow). (c) Unpolarized directional emission pattern from the dipole oriented perpendicular to the long axis of the nanowire. (d)Polarized directional emission of the dipole perpendicular to the axis of the nanowire with a polarization along the vertical direction on the image ($\varphi = 90°$ and $270°$, indicated by the white double arrow).

We observe that the ring-like emission pattern is characteristic of the emission from a dipole moment parallel to the nanowire axis, yielding indeed the largest contribution to the total Fourier image. Although weaker, the contributions from the two other dipole moments perpendicular to the nanowire axis, with the emission pattern of a single elongated lobe along the nanowire axis, are also present. This is evidenced by the plots of the cross cuts through the images in Figures 4.3(a) and 4.5(a), in which it can be appreciated a significant emission at the center of the Fourier image, that otherwise would be zero.

The excellent agreement between the simulations and the measurements can be appreciated in Figure 4.7. This agreement sheds much light onto various aspects of the emission process.

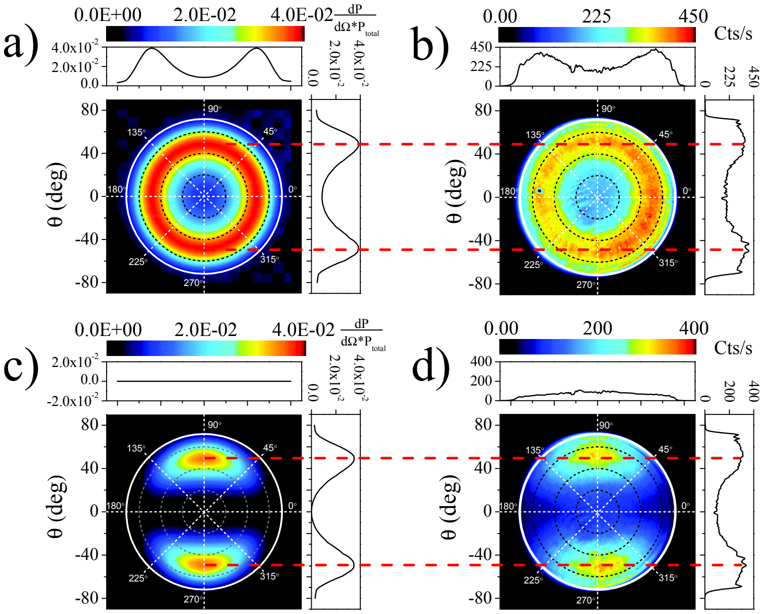

Figure 4.7: Direct comparison of the (a) simulated and (b) measured unpolarized directional emission of the nanowire standing on top of an InP substrate. In the simulations, the dipole radiates at a wavelength of $\lambda = 850$ nm, while the measurement is done using a $\lambda = 850$ nm bandpass filter (bandwidth of 10 nm at FWHM). (c) Simulated polarized directional emission compared to (d) measured polarized directional emission of the same nanowire and for the same wavelength as in (a) and (b), respectively. The corresponding features in simulations and measurements are pointed out with red dashed lines.

Since all dipole orientations contribute to the emission with the same relative weight, photoluminescence excitation in this configuration leads to essentially unpolarized emission [141]. The exact location of the emission within the nanowire is not crucial to the directionality of this emission with the excitation conditions used in the experiments, that is, uniform along the nanowire. To confirm this point, in the simulations we have varied the position of the dipoles along the nanowire axis, leading to very similar results unless emitting from the end facets of the nanowire. Incidentally, by spatially averaging the dipole emission, such edge contributions to the Fourier images would be irrelevant. Despite the inferred uniform excitation and fairly uniform spatial photoluminescence from the whole nanowire, the emission is strongly directional with a preferred polarization. This is fully supported by our numerical calculations, which reveal that the emission of the three orthogonal dipoles are governed by the environment, namely, the nanowire, through its local density of electromagnetic states (LDOS). The nanowire plays thus the role of a nanoantenna, controlling the emission of the dipole by its geometry and dimensions.

To study the antenna properties of the emission in more detail, we have investigated the modes associated to an infinitely long cylinder described by the corresponding dispersion relation (see Section 2.3). Figure 4.8 displays the dispersion relation of a lossless InP cylindrical waveguide for the fixed wavelength of $\lambda = 850$ nm ($k_0 d = 0.74$) and varied the diameter of the cylinder. The cylinder has a refractive index $n_{\mathrm{InP}} = 3.42$ and is surrounded by vacuum. The vertical axis in this figure indicates the free-space wavenumber (corresponding to the fixed wavelength of $\lambda = 850$ nm) multiplied by the diameter of the cylinder. The horizontal axis defines the real component of the propagation constant $\mathrm{Re}(k_z)$ of eigenmodes in the cylinder multiplied by its diameter. The eigenmodes are labeled in the plot. The dispersion relation is divided in three different zones, depending on the kind of the supported waveguide modes. The modes with a complex propagation constant and such that $k_z < k_0$ can leak to the light cone in air, that is indicated by the gray area in Fig. 4.8. The white area is the light cone in InP and contains the guided modes with a purely real propagation constant such that $k_0 < k_z < n_{\mathrm{InP}} k_0$. The black area in the figure shows the part of the dispersion relation where no modes can exist (the forbidden cone). The dashed horizontal line in the figure indicates the cylinder with a diameter of 100 nm. Our results in Figure 4.8 show that there is the TM_{01} leaky mode with a real component of the propagation constant $\mathrm{Re}(k_z)d = 0.65$, that can be excited. From the imaginary component of the propagation constant $\mathrm{Im}(k_z)$ (not shown in the plots), the decay length of 0.75 μm for this mode is inferred. Although the hybrid fundamental guided mode HE_{11} (having no cut-off frequency) is present, its propagation constant coincides with the light line for small cylinder diameters. The proximity to the light line implies that at the wavelength of InP emission ($\lambda = 850$ nm) and for a nanowire diameter of $d = 100$ nm, no coupling of the emission to the HE_{11} mode occurs. We support this claim by comparing the electric field intensity of the leaky TM_{01} mode and the guided HE_{11} mode supported by the nanowire. The insets in Figure 4.8 show the profiles of electric field intensity of the TM_{01} and HE_{11} modes in the cross section of a 100 nm-thick cylinder. While the intensity of the TM_{01} mode in the cylinder is non-zero with a relative maximum in the center, the HE_{11} mode intensity is localized into the surrounding medium [25, 142]. This means that there is no significant coupling of light generated inside the cylinder into the weakly guided HE_{11} mode.

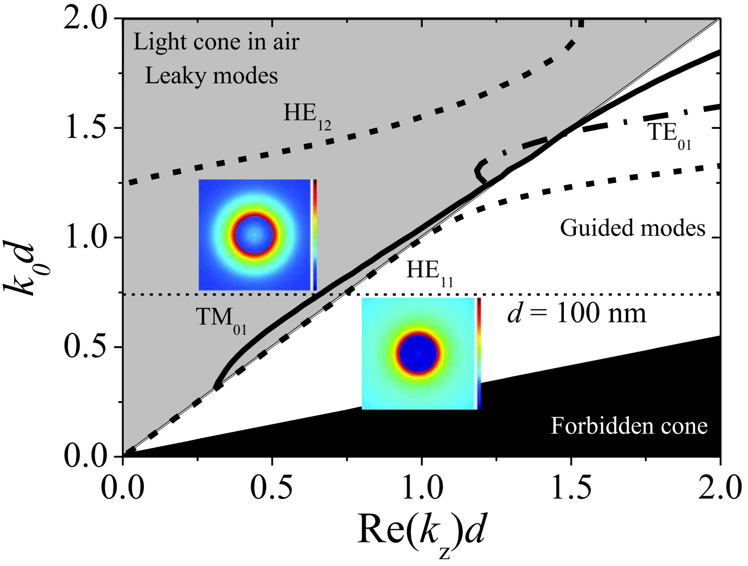

Figure 4.8: Dispersion relation of the eigenmodes supported by an infinite InP cylinder (fixed wavelength at 850 nm, $n_{\mathrm{InP}} = 3.42$, with varying diameter d). Leaky modes are inside the light cone indicated by the shaded area, while guided modes are outside this cone. The respective modes and their orders are indicated in the graph. The horizontal dotted line indicates the particular diameter $d = 100$ nm. The insets display the profiles of total intensity of TM_{01} and HE_{11} modes for $d = 100$ nm-thick cylinder in the plane of its cross-section.

Figures 4.9(a) and (b) show the unpolarized, normalized emitted power as a function of the angle of emission for dipoles oriented parallel and perpendicular to the axis of the nanowire, respectively. The angle-dependent emitted power is normalized by the total emitted power. The black-solid curves represent the emission of a dipole embedded in the nanowire, while the black-dashed curves illustrate the emission of a dipole in the free space. The dipole radiates in a medium of refractive index of $\mathrm{Re}(n_{\mathrm{InP}}) = 3.42$. As can be appreciated in Figure 4.9(a), due to the coupling to the leaky mode, the emission of a vertical dipole in the nanowire of diameter $d = 100$ nm is enhanced or inhibited in certain directions (e.g. enhanced ~ 3.4 times at $\theta = 49°$) with respect to that of a dipole in free space with the same orientation. This is in agreement with the leaky mode symmetry, where the maximum of the electric field parallel to the nanowire axis is located at the center of the cross section of the nanowire. The fact that such a leaky mode is excited contributes through an enhanced local density of optical states (LDOS) to an increased photoluminescence, as the LDOS of the nanowire supporting a single mode is basically governed by the mode local electromagnetic field. At the same time, the symmetry of the leaky mode efficiently suppresses the emission of a dipole perpendicular to the axis of the nanowire, as displayed in Figure 4.9(b).

The efficiency of the emission can be tailored by modifying the diameter of the nanowire. To illustrate that, we have calculated the emission pattern of a nanowire with a diameter of 25 nm, for which no leaky modes are supported at $\lambda = 850$ nm, as evidenced in Figure 4.8. As mentioned above, the weakly guided mode HE_{11} is present, but no appreciable coupling of the emission into it takes place [142]. The gray dash-dotted curves in Figures 4.9(a) and (b) illustrate the emission from a dipole parallel and perpendicular to the axis of the nanowire, respectively. While the thin nanowire can still enhance the emission of a parallel dipole with respect to a dipole in free space, this enhancement is significantly lower than for the $d = 100$ nm nanowire. The emission of a perpendicular dipole in 25 nm-thick nanowire is further suppressed compared to the nanowire with a diameter of 100 nm.

The directional emission of nanowires is important for the design and optimization of nanowire-based light-emitting diodes and single photon sources. The design of efficient light sources needs to consider the dimensions of the nanowires that determine the solid angle of the emission. By reciprocity, the optical absorption efficiency of semiconductor nanowires strongly depends on the angle of incidence of light. The directional absorption by individual nanowires is described in Chapter 6 of this thesis. The antenna-like behavior of nanowires will have an impact on the design of nanowire-based solar cells.

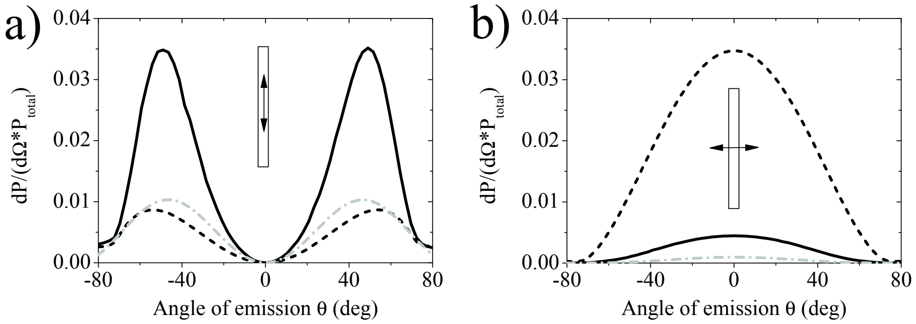

Figure 4.9: Emitted power as a function of the emission angle emission, normalized by the total emitted power P_{total}, calculated for (a) a dipole oriented parallel to the axis of the nanowire, and (b) a dipole with perpendicular orientation with respect to the axis of the nanowire. The substrate is included in these calculations. The calculations are made for two nanowire diameters, $d = 100$ nm (black-solid curves) and $d = 25$ nm (gray dash-dotted curves), both with a length of 3.13 μm. The black dashed curves correspond to a calculation of the emitted power of a dipole in homogeneous InP medium.

4.4 Conclusions

In conclusion, by measuring the directional and polarized emission of single nanowires using Fourier microscopy, we have demonstrated the antenna-like emission of these nanostructures. Finite element simulations of a dipole source embedded in a nanowire provided an excellent agreement with the measurements. Similar to RF linear antennas, semiconductor nanowires exhibit a directional and an enhanced emission due to resonances in the structure. The directional emission is ruled by the leaky modes supported by nanowires. These modes are also responsible for a modification of the local density of optical states and for the enhancement of the emission of dipoles with a certain dipole moment relative to the nanowire orientation and the inhibition of the emission for other orientations. This demonstration of nanoantenna emission from semiconductor nanowires is of relevance for designing novel nanowire light emitting diodes and single photon sources with tailored emission characteristics.

CHAPTER 5

QUASI-2D NANOWIRE PHOTONIC CRYSTALS AS DIRECTIONAL EMITTERS

Controlling the dispersion and directionality of the emission of nanosources is one of the major goals of nanophotonics research. This control will allow the development of highly efficient nanosources even at the single-photon level. One of the ways to achieve this goal is to couple the emission to Bloch modes of periodic structures. In this chapter, we present the first measurements of the directional emission from semiconductor nanowire photonic crystals by using Fourier microscopy. The light emission from a heterostructure grown in each nanowire is governed by the photonic (Bloch) modes of the photonic crystal. We also demonstrate that the directionality of the emission can be easily controlled by infiltrating the photonic crystal with a high refractive index liquid.

5.1 Introduction

Among the most promising structures for light emission are photonic crystals (PhCs), that is, periodic structures of two or more dielectrics or semiconductors with different refractive indices [143], where the periodicity is comparable to the wavelength of light. PhCs have become a broad field of research over the past years. The propagation of electromagnetic waves in such a medium is described by Bloch modes. Typically, the dispersion relations of Bloch modes in PhCs reveal photonic stop-gaps, that is, frequency ranges in which there are no Bloch modes available for light propagation along certain directions. A photonic band gap is formed when propagation is forbidden along all directions. In a perfect PhC with a band gap, the spontaneous emission of an excited state can be fully inhibited. These properties have been extensively studied to achieve control over the spontaneous light emission of nanophotonic sources [144, 145]. PhCs have been proven to confine and manipulate light [146, 147], modify the density of optical states [148, 149], create high quality factor cavities leading to lasing [150], and increase the outcoupling efficiency of light sources [130, 151, 152].

Semiconductor nanowires are potentially interesting building blocks for two dimensional (2D) PhCs. Nanowires grown by the vapor-solid-liquid (VLS) method have become a major field of research due to their unique optical properties [7, 39, 44, 153, 154]. The bottom-up approaches that are used to grow nanowires allow the combination of different semiconductors in single nanostructures despite the mismatches of the crystal lattice constant. This property has opened new opportunities to design a large variety of heterostructures. Some examples of these structures are wrapped-around quantum wells [17, 132], superlattices [11, 155], quantum dots embedded in nanowires showing single-photon emission [21, 22, 24, 27], and zincblende-wurtzite phase homostructures [156, 157]. Furthermore, it is possible to grow III-V semiconductor nanowires on top of silicon substrates, combining the high-end properties of III-V material with well-developed and cheap silicon technology [15]. It has been recently demonstrated that ordered arrays of nanowires can be grown on patterned substrates [66, 74, 75]. These ordered arrays of nanowires behave as 2D PhCs, modifying the nanowire emission [18], and even leading to lasing [20].

In this chapter, we demonstrate the directional emission of heterostructures embedded in semiconductor nanowires forming a quasi-2D PhC using Fourier microscopy. This technique allows us to image the emission in the reciprocal space in which each coordinate corresponds to one direction of emission (see Chapter 3.2. The directional emission arises from the coupling of the emission from heterostructures in individual nanowires to Bloch modes in the PhC [151, 158]. The investigated samples can be described as a quasi-2D PhC due to the periodic arrangement of the nanowires and their finite length [143]. This finite length allows an efficient coupling of the photoluminescence of heterostructures into free space at certain directions. We also demonstrate that it is possible to efficiently control the directionality of the emission by changing the refractive index of the medium surrounding the nanowires. This change is achieved by infiltration of the nanowire array with a liquid.

5.2 Ordered arrays of heterostructured nanowires

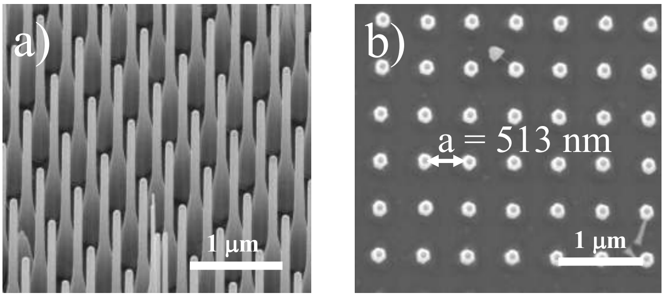

Figure 5.1: (a) Scanning electron micrograph of the array of InP nanowires taken at an inclination angle of 30°. Each nanowire in the array has a length of 3 μm and contains a 20 nm InAsP segment located at 1 μm from the top. (b) Top view of the nanowire array showing the high quality of the periodic arrangement of the nanowires. The wires are organized in a square lattice with a pitch of $a = 513$ nm.

The nanowire arrays investigated in this chapter are grown on top of a thick (111)B InP substrate by gold-catalyzed vapor-liquid-solid (VLS) mechanism in a metalorganic vapour phase epitaxy (MOVPE) reactor [1].[1] This fabrication method is described in Chapter 1.2. The exact position of the nanowires is defined by the position of the gold particles catalyzing the growth. These particles were deposited by using substrate conformal imprint lithography [76]. The complete fabrication process of this particular sample is discussed in details elsewhere [66]. The array is formed by InP nanowires embedding an $InAs_{0.1}P_{0.9}$ heterostructure. The incorporation of the As in InP narrows the semiconductor's electronic band gap and red-shifts the photoluminescence. The nanowires have an overall length of 3 μm, with a tapered base (1 μm-long) and straight upper part (2 μm-long). This structure can be appreciated in the tilted scanning electron microscope image of the sample shown in Fig. 5.1(a). The InAsP heterostructure, with a length of 20 nm, is located at 1 μm from the top of the wires. The diameters at the bottom of the base and of the straight part are 270 nm and 90 nm, respectively. The nanowires are arranged in a square lattice with a pitch of $a = 513$ nm. The lattice is evident in Fig. 5.1(b) that shows scanning electron microscope image in which the sample is viewed from the top of the wires.

Defects in the periodic structure consist of slightly tilted and missing nanowires. These

---

[1] The nanowires were grown by A. Pierret, M. Hocevar and W.G.G. Immink under supervision of E.P.A.M. Bakkers at Philips Research Laboratories in Eindhoven

defects do not have a significant influence on the optical measurements presented in this chapter and they are not considered further. Defects in the crystallographic structure of individual nanowires may influence the intensity of the emission and broaden the emitted spectrum, which is irrelevant for the directional emission of the periodic lattice of nanowires.

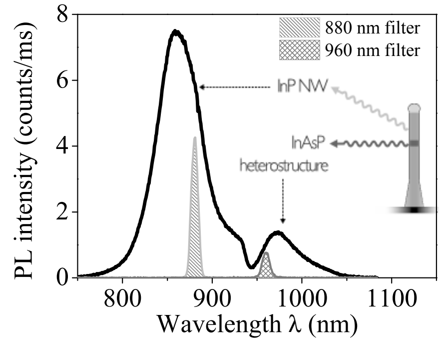

Figure 5.2: Photoluminescence spectrum of the InP nanowire array. The broad peak centered at λ = 860 nm is the emission from the wurtzite InP that forms the nanowires. The peak centered around λ = 970 nm is the emission from the InAsP segment located 1 μm from the top of each nanowire (as represented in the inset). Directionality of the emission was investigated using two different band pass filters: λ = 880 nm and λ = 960 nm, both with a transmission band of 10 nm (FWHM). The PL spectra of the nanowire array measured with the filters are displayed in the graph with light-gray and dark-gray dashed areas, respectively.

The photoluminescence (PL) spectrum of the nanowire array is shown in Fig. 5.2. The peak centered at λ = 870 nm can be attributed to the PL from the InP in the wurtzite phase. InP nanowires grow preferentially in wurtzite phase in contrast to bulk zincblende InP (as in the case of the substrate) that is expected to emit at around λ = 922 nm [67]. The broader, red-shifted peak centered at λ = 970 nm, corresponds to the PL from the 20 nm-thick InAsP heterostructure incorporated in the nanowires. This heterostructure provides a light source embedded in the periodic array and with a well-defined position. The large size of the InAsP heterostructure prevents any noticeable quantum confinement for the electrons and its electronic band structure, as well as the emission properties, is assumed to be that of bulk InAsP.

5.3 Experimental configuration

For measuring the directional emission of the nanowire array we used a Fourier microscope (as described in Chapter 3) with focused excitation. The Fourier microscope was equipped with a 100× objective of numerical aperture NA = 0.95 and a 100×, NA =

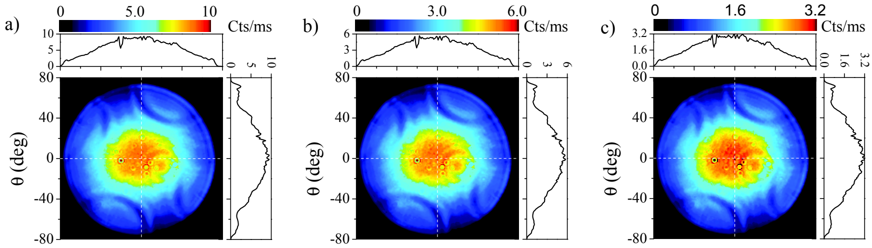

Figure 5.3: Fourier images of the directional photoluminescence of an InP nanowire array obtained with a band pass filter λ = 880 nm and taken for three different polarizations of the pumping beam. The polarization of the pump in (a) was set to achieve the highest possible photoluminescence intensity in the Fourier camera. To illustrate that the polarization of the pump affects only the emission intensity and not the pattern, it was rotated by 45° and 90° with respect to the optimum direction and the corresponding Fourier images are displayed in (b) and (c).

1.3 objective for the measurements in respectively air and immersion oil (n_{Oil} = 1.52). The array was optically pumped through the same objective used to collect the PL. We have used a continuous wave diode laser with an emission wavelength centered at 785 nm to excite the nanowire array. This wavelength allows us to efficiently pump the heterostructure, avoiding a strong decrease of the pump intensity by absorption in the top section of the InP nanowires [43]. The excitation used in the measurements described in section 5.5 is linearly polarized along the square lattice axis. In order to rule out any influence of the pump polarization on the emission pattern, several measurements with the plane of polarization oriented in three different directions (every 45°) were performed. These measurements did not reveal any differences between the emission patterns, as can be appreciated in Fig. 5.3. The only differences were on the emission intensities.

The emission into the solid angle collected by the microscope objective appears as a disc in the Fourier image. Each point in this disc corresponds to one direction of emission, e.g., a spot located at the edge of the Fourier image represents the emission at a large angle, given by the NA of the objective, relative to the normal to the sample surface. The center of the image corresponds to the emission normal to the sample surface. For the measurements of the nanowire PhC in air, the maximum collection angle associated with the objective with a NA of 0.95 is 72°. The maximum collection angle of the oil immersion objective used for measurements of the infiltrated PhC (NA = 1.3 in n_{Oil} = 1.52) is 59°. The Fourier microscope is also equipped with a polarizer in front of the CCD camera, that is, in the detection path. This polarizer makes it possible to distinguish between $s-$ and $p-$polarized emission along the diameter of the Fourier image parallel ($p-$polarized) and perpendicular ($s-$polarized) to the transmission axis of the polarizer, respectively. The transmission through the polarizer in other directions is a superposition of $p-$ and $s-$polarized emission (see Fig. 3.6 in Section 3.4.2).

The Fourier images were recorded on a CCD camera (Andor Luca S). Integration times were of the order of 50 ms for the InP emission and 1 s for the InAsP emission. In order to distinguish the emission from the wurtzite InP nanowires from the emission of the InAsP heterostructures embedded into the nanowires, the Fourier images were measured after transmission through a band pass filter. The nanowire emission was measured after a filter with a central wavelength of 880 nm and a bandwidth of 10 nm at FWHM, while the emission from the heterostructures was measured after a filter with a central wavelength of 960 nm and a bandwidth of 10 nm at FWHM. The transmission of these filters is illustrated in the spectrum of Fig. 5.1(b), where the cyan area corresponds to the sample PL after the 880 nm filter and the red area represents the PL after the 960 nm filter.

The images for unpolarized emission are the sum of the images taken with two orthogonal polarizations. In the unpolarized images, the intensity along the horizontal direction appears lower. This effect is not the feature of the directional emission, but it is attributed to the polarization dependent transmission through a beam splitter used in the setup. Although we correct the Fourier images for this effect in other chapters, the data presented here had been collected before the correction procedure was developed.

The measurements described in section 5.6 were done as follows: immersion oil was pipetted on top of the array in order to cover the whole sample. To force the infiltration of the voids in between nanowires, the sample was placed into a vacuum tube during 5 minutes under a pressure on the order of 0.02 atm. The optical measurements were performed after this procedure and within 5 hours. A second set of measurements was realized 24 hours later and no significant changes were noticed. The PL of both InP and InAsP was not quenched by the contact with the immersion oil.

5.4 Photonic crystals

Photonic crystals are inhomogeneous media with a periodic refractive index [143] of the periodicity comparable to the wavelength of light. Depending on the number of dimensions for which the periodicity of refractive index is defined, they are one-dimensional [159], two-dimensional [160] or three-dimensional [161, 162]. The propagation of electromagnetic waves in such medium is similar to the propagation of electronic waves in an atomic crystal. In atomic crystals, the periodicity of the Coulomb potential is in the order of Angströms. Electronic waves, whose wavelengths are of the same order propagate only in particular directions in form of Bloch modes, or cannot propagate at all. The latter case can result in a, so-called, electronic band gap, a forbidden energy range in the crystal band structure. In a photonic crystal, the periodic modulation of refractive index plays the role of a periodic potential for electromagnetic waves. To form photonic Bloch modes, the periodicity of the refractive index needs to be in the order of the wavelength of electromagnetic waves. This means that at optical and near-infrared frequencies the lattice constant of PhCs is in the order of hundreds of nanometers to

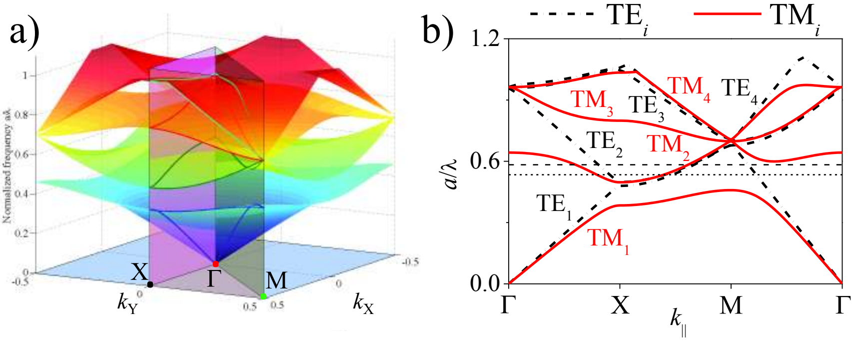

Figure 5.4: (a) Calculated full dispersion relation of TM eigenmodes of a 2D photonic crystal consisting of 90 nm-thick lossless InP cylinders in air. The cylinders are arranged in a square lattice with the pitch of a = 513 nm (n_{InP} = 3.37, n_{Air} = 1). (b) Simplified photonic band structure of a 2D photonic crystal with the same lattice parameters as in (a) showing the TM (solid lines) and TE Bloch (dash-dotted lines) modes between high symmetry points of the first Brillouin zone in the reciprocal space. The dashed and dotted horizontal lines indicate the wavelengths of λ = 880 and 960 nm, respectively. These are the emission wavelengths of InP and InAsP discussed in Section 5.5

few micrometers. In such structure, the scattering and interference of light lead to Bloch modes, which represent the electromagnetic eigenstates of the PhC.

The eigenvalues associated with the Bloch modes define the PhC band structure or the dispersion relation of the light propagating in the periodic structure. Photonic modes exist only for light propagating in the directions where it encounters a periodic modulation of the refractive index. In case of a two-dimensional array of vertical dielectric cylinders, Bloch modes are defined in the plane perpendicular to the long axis of those cylinders. Light can propagate in this plane with two orthogonal polarization states. For the coordinate system defined in Fig. 5.5, the transverse electric (TE) Bloch modes correspond to a polarization perpendicular the elongation of the cylinders (parallel to the plane of propagation, $E_z = 0$), while the transverse magnetic (TM) modes have a polarization parallel to the cylinders (perpendicular to the plane of propagation, $E_x = E_y = 0$). Figure 5.4(a) shows the calculated full dispersion relation of TM eigenmodes of a 2D photonic crystal consisting of 90 nm-thick lossless InP cylinders in air ($n_{\text{InP}} = 3.37$, $n_{\text{Air}} = 1$). [2] The cylinders are arranged in a square lattice with the pitch of $a = 513$ nm. In this figure, the photonic bands are represented as surfaces. Each point in these surfaces corresponds to the normalized frequency of light $\left(\frac{a}{\lambda}\right)$ that can propagate in a particular direction described by the parallel wave vector $\mathbf{k}_{\|} = \mathbf{k}_x + \mathbf{k}_y$. The unit of k_x and k_y in the plot is $\frac{\pi}{a}$.

---

[2] The eigenmodes of Maxwell's equations in the periodic dielectric structure were computed in the frequency domain by the plane wave expansion method, using the freely available software package MIT Photonic Bands [163].

Due to the complexity of the full band structure and its symmetry, usually the dispersion relation is given only at the edges of the irreducible Brillouin zone. The Brillouin zone in the smallest element in the reciprocal space ($k_\parallel$-space) preserving the symmetry of the whole band structure. This zone is marked in Fig. 5.4(a) by three vertical planes and delimited by the Γ ($k_\parallel = 0$), X ($k_{\mathrm{x}} = \frac{1}{2}\frac{\pi}{a}, k_{\mathrm{y}} = 0$) and M ($k_{\mathrm{x}} = k_{\mathrm{y}} = \frac{1}{2}\frac{\pi}{a}$) points. The intersections of the vertical planes with the full photonic band structure that are marked in the graph represent the simplified band structure shown in Fig. 5.4(b). In this figure we have also plotted the TE bands. The different bands in Fig. 5.4(b) are labeled depending on the polarization of the electromagnetic wave in the structure.

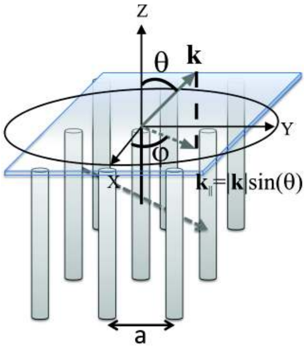

Figure 5.5: Schematic representation of the directional emission of photonic crystals. Light coupled to a Bloch mode (gray dashed arrow) can be scattered out at the interface. The magnitude of the parallel wave vector of light propagating in the Bloch mode (gray dashed arrow) is conserved at the interface of the finite crystal. This leads to emission in a particular direction described by the elevation angle θ and the azimuthal angle φ of emission.

If a PhC is finite, light coupled to a mode can be scattered out of the PhC conserving the magnitude of the parallel wave vector (wavenumber) at the interface (as shown in Fig. 5.5). This leads to emission in a particular direction described by the elevation angle θ and the azimuthal angle φ. The angle θ is related to the wavenumber in the plane of the sample $\theta = \arcsin\left(\frac{k_\parallel}{k}\right)$, while the angle φ is related to the ratio of the magnitude of the in-plane wave vector components, $\varphi = \arctan\left(\frac{k_{\mathrm{x}}}{k_{\mathrm{y}}}\right)$.

Figure 5.6 shows the same photonic band structure for TM-polarized Bloch modes (as in Fig. 5.4(a)) intersected with a plane of constant frequency $\frac{a}{\lambda} = 0.58$ (an isofrequency surface). This frequency corresponds to the wavelength of $\lambda = 880$ nm. The parallel wave vectors associated to the points of intersection (black points in Fig. 5.6) can be directly translated to the directions of far-field emission, (θ, φ).

Figures 5.7(a) and (b) represent the isofrequency surfaces in polar coordinates for $\lambda = 880$ and 960 nm respectively. The radius in these plots denotes the angle of emission θ and the azimuthal angle in the plots is the azimuthal angle of emission φ. The left panel in these figures corresponds to TM modes, while the right panel contains TE modes. We have also indicated in the figure the order of the mode.

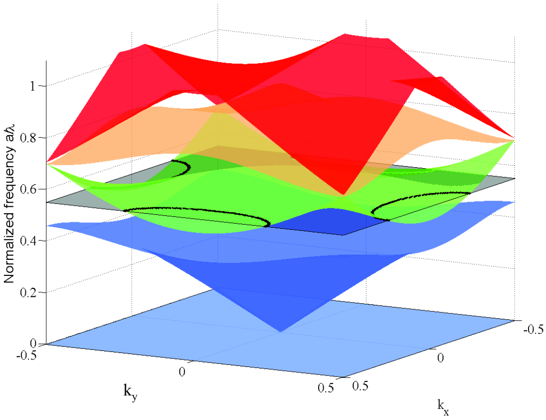

Figure 5.6: Full band structure for TM Bloch modes, as in Fig. 5.4(a) intersected with a plane of constant frequency $\frac{a}{\lambda} = 0.58$ corresponding to the wavelength of $\lambda = 880$ nm. The intersection of this plane with the band structure is marked with black points.

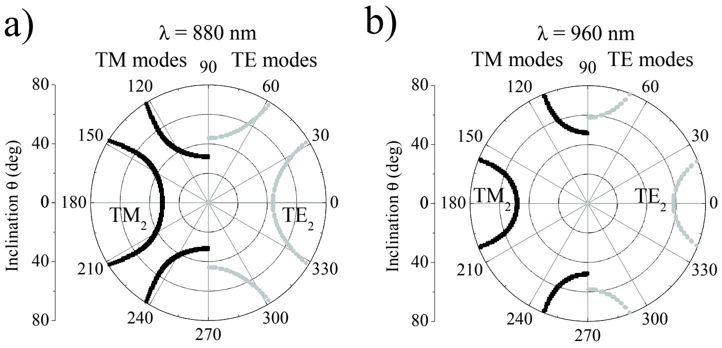

Figure 5.7: (a) Calculated isofrequency surface for $\lambda = 880$ nm. The wavenumbers have been transformed into polar coordinates. The TM modes are displayed on the left, while the TE modes are on the right. The isofrequency surface for $\lambda = 960$ nm is shown in (b). In those plots, the radius represents the angle of emission θ, while the azimuthal angle φ corresponds to the azimuthal angle of the emission.

We must point out that our periodic array of InP nanowires is not truly a 2D-PhC due to the finite length of the nanowires. Nevertheless and as it is shown later, the directional emission of the photoluminescence from the investigated sample is determined by its periodicity and can be associated to the band structure of the infinite crystal. Therefore, we refer to the array as a quasi-2D photonic crystal.

5.5 Directional emission of quasi-2D nanowire photonic crystals

The Fourier image of the InP nanowire emission at λ = 880 nm without polarization selection is displayed in Fig. 5.8(a). This emission pattern strongly differs from a Lambertian emission expected from thin emitting films and flat surfaces. The four-fold rotational symmetry of the Fourier image follows the symmetry of the square array of nanowires. The most salient feature is the emission bands at large angles θ. In order to determine the polarization of the emission in these bands, we have obtained the Fourier image with the polarizer oriented along the vertical direction (azimuthal angle $\varphi = 90°$ and 270°) as it is displayed in Fig. 5.8(b). The emission along $\varphi = 90°$ and 270° corresponds to $p-$polarized emission, while the emission along $\varphi = 0°$ and 180° is $s-$polarized. The absence of the emission bands for $s-$polarization allows concluding that these bands can be attributed to the TM_2 band of the PhC (see Fig. 5.7(a)).

As can be appreciated in Fig. 5.8(b), the emission is formed by two concentric bands. These bands are marked by the arrows in the cut to the Fourier image at $\varphi = 90°$ and 270° displayed on the right inset of the figure and are pointed in the Fourier image with red dashed lines. The double bands are separated by a local minimum that is marked in the vertical profile in Fig. 5.8(b) with a magenta oval. The emission at λ = 880 nm originates from the whole InP nanowire, including the uppermost section, i.e., close to the sample interface, where the optical pump is absorbed [43]. The sample interface plays an important role in the light emission by the InP nanowires: an interface separating a photonic crystal from the homogenous medium where the emission is detected, is present in any experiment. The conservation of the parallel wavenumber to the interface makes it possible to correlate the angular emission with the isofrequency surfaces of the Bloch modes of the PhC. However, the interface breaks the translational invariance of the nanowire array along their elongation and limits the validity of the band structure calculation done for an infinite 2D-PhC. Therefore, it is expected that light emitted by the nanowire layer close to the interface will be affected by the presence of this interface. For angles θ up to $\approx 35°$, there is a relatively strong emission with no particular directional features. We associate this to the emission of the nanowires that is not coupled to the modes of the periodic structure. The origin of the double bands separated by the local minimum might be also attributed to the broken translational invariance in z direction of the sample. As a result, light emitted by nanowires has a possibility to undergo multiple reflections at the interfaces of the sample leading to Fabry-Pérot-like resonances modulating the emission pattern of the Bloch modes.

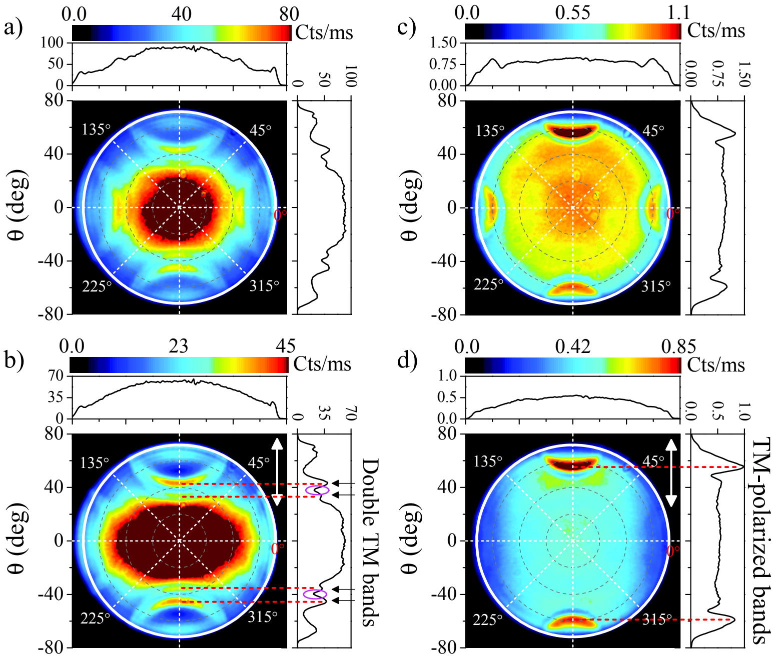

Figure 5.8: Measured Fourier images of the light emission from an InP nanowire array emitting in air. The top images represent the unpolarized emission for $\lambda = 880$ nm (a) and $\lambda = 960$ nm (c) while the bottom ones [(b) and (d)] are taken for the same wavelengths but with a polarizer in front of the Fourier camera. The polarizer's transmission axis is aligned along the vertical direction ($\varphi = 90$ and 270°) and is indicated in the graphs by the white double-arrows. The white circle represents the maximum collection angle of the objective with NA = 0.95, equal to $\theta = 72°$. The graphs on the top and right side of each figure show the profiles of the Fourier images along the horizontal and vertical directions crossing at the center of the images. The magenta oval in the profile plot in (b) indicates the local minimum of the emission discussed in the text. The red dashed lines are guides for the eyes and indicate the TM-polarized bands that correspond to the TM Bloch modes of the photonic crystal. In the Fourier images, the radius represents the angle of emission θ, while the azimuthal angle φ corresponds to the azimuthal angle of the emission.

In order to minimize the influence of the interface in the emission of the nanowire PhC, we consider in Fig. 5.8(c) and (d) the unpolarized and polarized emission from the InAsP heterostructure, located at a depth of 1 μm from the surface. In these measurements we observe a unique set of bands, corresponding to an emission around $\theta \approx 57°$ for $\varphi = 0°, 90°, 180°$ and 270°. Note that there is a small asymmetry in the maximum intensity emitted at $\theta \approx 57°$ for $\varphi = 90°$ and 270°. This asymmetry can be attributed to a non-uniform collection efficiency in our setup. The directional emission of similar arrays of nanowires has been reported and described with finite-difference time-domain (FDTD) simulations in Ref. [18]. The directional emission was explained by its coupling to modes in the periodic structure and Fabry-Pérot resonances in the nanowire layer with finite length.

Generally, the measured polarized emission in Figs. 5.8(b) and (d) matches well with the calculated isofrequency surfaces of the TM_2 mode at λ = 880 nm λ = 960 nm in a 2D photonic crystal (Fig. 5.7 (a) and (b), respectively) with the same pitch and dielectric rod diameter as the nanowire array. This comparison can be directly appreciated in Figs. 5.9(a) and (b) for the respective wavelengths of the emission, where we plot the calculated isofrequency surfaces together with the measurements. The calculated TM Bloch modes are plotted in red, while the calculated TE Bloch modes are plotted in green. The TE-polarized features that could be associated to TE Bloch modes are not observed in the experiment. The small mismatch in the position of the TM bands might be attributed to the uncertainty of the nanowire diameters, lattice pitch, complex refractive index of the nanowires, as well as to the uncertainty of the determination of center and borders of the Fourier images.

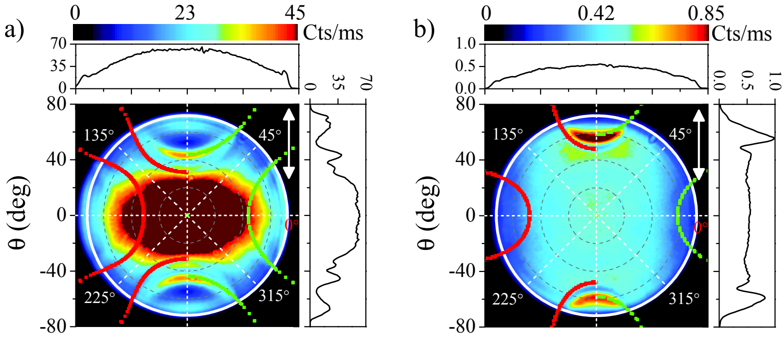

Figure 5.9: Comparison between the measured polarized Fourier images of the light emission from an InP nanowire array emitting in air (the same as in Figs. 5.8(b) and (d)) and the calculated isofrequency surfaces of the dispersion relation for (a) λ = 880 nm and (b) λ = 960 nm emission, respectively (the same as in Figs. 5.7(a) and (b)). The red points represent the TM_2 modes, while the green points show the TE_2 Bloch modes for each wavelength.

The absence of the TE_2 mode emission in the Fourier images can be explained by examining the spatial distribution of the electric field intensity in the unit cell of the photonic crystal. Figure 5.10 illustrates a calculation of this field intensity distribution, using the plane wave expansion method [163], where (a) and (b) correspond to the TM_2 mode and (c) and (d) to the TE_2 mode at the two investigated wavelengths, λ = 880 nm [(a) and (c)] and λ = 960 nm [(b) and (d)]. TM modes are described by the E_z component of the field, while E_y describes the TE modes in $\Gamma-X$ direction of the reciprocal space (see Fig. 5.5

for coordinates and Fig. 5.4 for the directions in the reciprocal space). At $\lambda = 880$ nm, most of the field intensity of the TM_2 mode is concentrated in the cylinder, in contrast to the TE_2 mode at the same wavelength, where the maximum field intensity is located around the cylinder. Similar behavior can be appreciated at $\lambda = 960$ nm, though, the contrast between the field intensity distributions for TM_2 and for TE_2 is lower. Therefore, it is reasonable to expect that light generated by the recombination of photoexcited electron-hole pairs in the nanowire can more easily couple to the TM_2 mode due to the good spatial overlap of this mode with the nanowire.

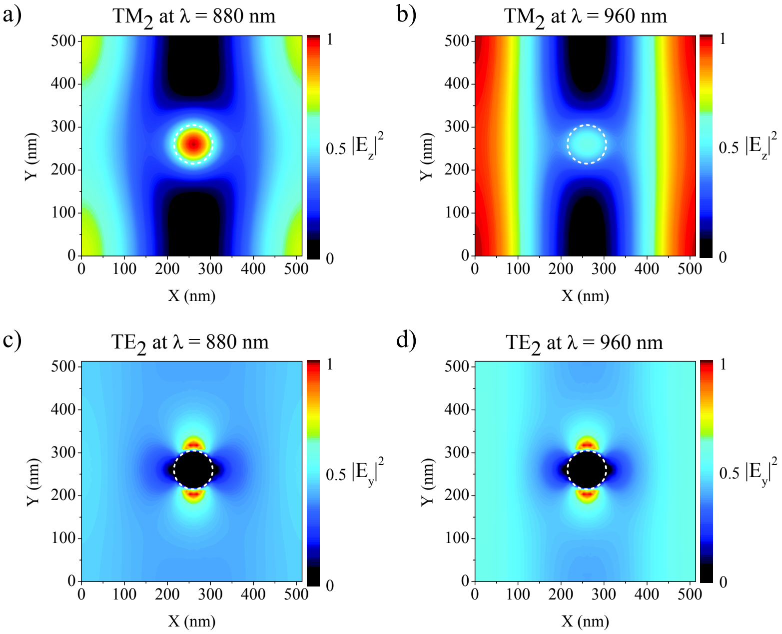

Figure 5.10: Calculated electric field intensity distribution of the photonic modes in a unit cell of a 2D photonic crystal. (a) E_z field intensity distribution of the TM_2 mode at λ = 880 nm and (b) λ = 960 nm. (c) E_y field intensity distribution of the TE_2 mode at λ = 880 nm, and (d) at λ = 960 nm. In all graphs, the field intensity is normalized to the maximum. The white dashed lines mark the position of the dielectric cylinder with a refractive index of $n = 3.37$ embedded in vacuum with a refractive index of $n = 1$. The field intensity distributions are calculated for the mode wave numbers in the $\Gamma - X$ direction in the reciprocal space.

5.6 Effect of the infiltration of the photonic crystal on the directional emission

In the previous section we have shown that the photonic Bloch modes can shape the directional emission of ordered arrays of nanowires. For any practical application it is important to control the directionality of the emission. To demonstrate this control, we need to modify the band structure of the nanowire PhC. The band structure of a PhC depends on the geometrical parameters defining the periodic structure, as well as on the permittivity of its constituents. The geometry of our sample is fixed. Therefore, the emission pattern is expected to change when the refractive index of the medium surrounding the nanowires is varied. Figures 5.11(a) and (b) illustrate this modified emission by plotting the isofrequency surfaces of a 2D PhC of InP nanowire with the same geometry as in Fig. 5.7(c) and (d), but with the voids in between nanowires filled with an oil with a refractive index of 1.52.

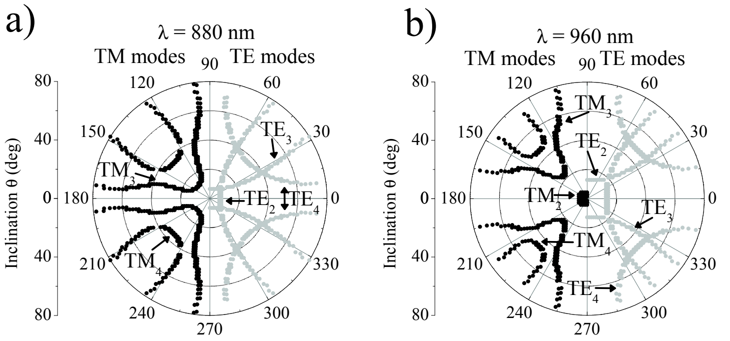

Figure 5.11: Calculated isofrequency surfaces of a 2D photonic crystal formed by infinitely long cylinders embedded in a medium with a refractive index of $n_{\text{Oil}} = 1.52$. The cylinders are made of a dielectric material with a refractive index of $n = 3.37$. (a) represents the isofrequency surface for $\lambda = 880$ nm, while (b) shows the isofrequency surface for $\lambda = 960$ nm. The TM modes are shown on the left side of the graphs and the TE modes are presented on the right side.

Figure 5.11(a) corresponds to the isofrequency surface at $\lambda = 880$ nm, while (b) is the isofrequency surfaces at $\lambda = 960$ nm. The band structure is much more complex and many TE and TM bands are expected to influence the emission of the array.

Figures 5.12 (a) and (b) show the Fourier images measured for the unpolarized emission from the infiltrated sample at these two wavelengths. These Fourier images show a fourfold symmetry but are very different from the case of the uninfiltrated array. The emission at $\lambda = 880$ nm from the InP nanowire (Figs. 7(a) and (c)) is dominated by the nondirectional emission which is not coupled to the modes of the periodic structure. The emission pattern of the heterostructure at $\lambda = 960$ nm (Figs. 5.12(b) and (d)) is much richer in directional features due to the more complicated band structure shown in Fig. 5.11(b). Clearly, changing the refractive index of an embedding medium modifies the dispersion relation of the quasi-2D photonic crystal influencing the directional light emission from embedded nanosources. While the uninfiltrated photonic crystal emission bands manifest mainly along the vertical and horizontal direction in the Fourier image, the infiltrated structure reveals more bands along the intermediate directions. For this reason we took Fourier images with a polarizer's axis oriented along the azimuthal angle of $\varphi = 135^\circ$ and 315°. For both investigated wavelengths, $\lambda = 880$ nm and $\lambda = 960$ nm, the emission bands show polarization dependence (Fig. 5.12(c) and (d)). Unlike before, there is a contribution of $s-$polarized directional emission features in the Fourier images. This contribution might be caused by the coupling of the emission to TE modes of the infiltrated sample or by scattering at the interface of the quasi-2D photonic crystal. The results of this section have demonstrated that we can achieve the control over the directional emission of the nanowire quasi-2D PhC by modifying the refractive index of the medium that surrounds the nanowires.

5.7 Conclusions

In conclusion, we have demonstrated the modified emission of semiconductor nanowire arrays and heterostructures in periodic arrays of nanowires. In particular, we have measured the directional photoluminescence of 2D nanowire array by using Fourier microscopy. This emission has been correlated to Bloch modes in 2D photonic crystals. By filling the voids between the nanowires, it is possible to modify the emission. The use of Fourier microscopy for the study of nanowires will facilitate the design of directional photon sources in quantum information and integrated optics applications.

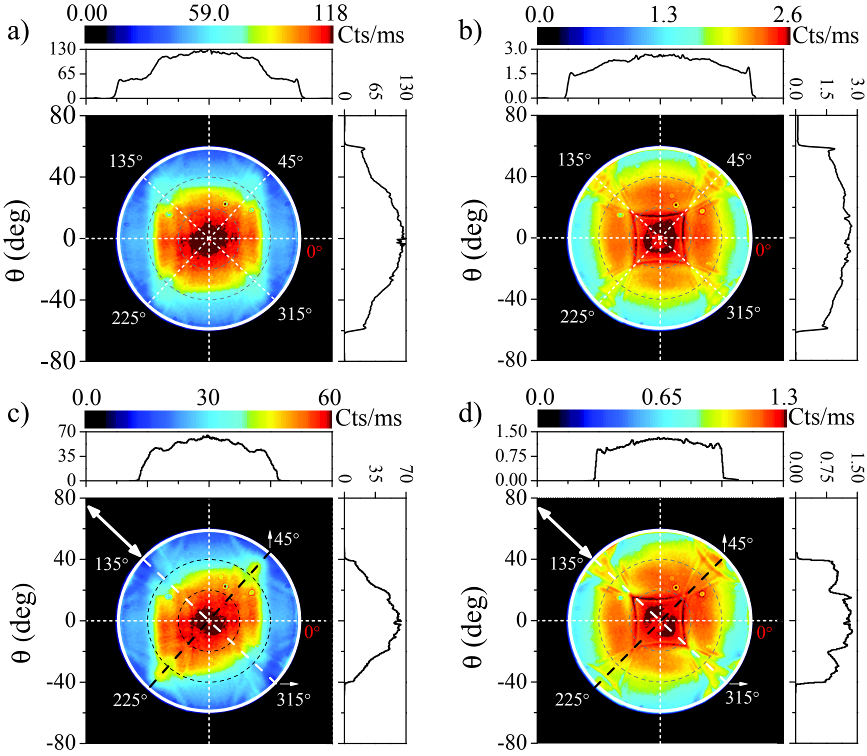

Figure 5.12: Measured Fourier images of the photoluminescence emission from the InP nanowire array embedded in an immersion oil with refractive index of $n_{\text{Oil}} = 1.52$. The top graphs [(a) and (b)] present the images of the unpolarized emission taken with band pass filters with a central wavelength of $\lambda = 880$ nm (a) and $\lambda = 960$ nm (b). The bottom graphs [(c) and (d)] display the emission for the same wavelengths recorded with a polarizer in front of the Fourier camera. The polarizer's transmission axis is oriented at $\varphi = 135$ and 315° and it is indicated by the white double-arrows in both graphs. The white circle represents the maximum collection angle, which for the objective with NA = 1.3 in a medium of $n_{\text{Oil}} = 1.52$ is equal to $\theta = 59°$. The graphs at the top and right side of (a) and (b) show the profiles of the Fourier images along the horizontal and vertical directions crossing at the center of the images. In (c) and (d) the profiles of the Fourier images are plotted along $\varphi = 45$ and 225° (top graph, corresponding to the black dashed line) and along $\varphi = 135$ and 315° (right graph, corresponding to the white dashed line) to illustrate the differences between pure $s-$ and $p-$polarized emission. These diagonal profiles are projected on the horizontal and vertical axes, respectively, appearing narrower than the profiles in (a) and (b).

CHAPTER 6

ANGLE-DEPENDENT LIGHT ABSORPTION OF INDIVIDUAL NANOWIRES

Understanding light absorption in individual semiconductor nanowires is crucial for optimizing the performance of nanowire-based solar cells. Here, we present angle-dependent measurements of light absorption in individual semiconductor nanowires using time-reversed Fourier microscopy. With this technique we are able to illuminate nanowires with a defined angle of incidence and polarization through a microscope objective. The results of the angle-dependent absorption measurements are compared to Mie theory that quantifies the coupling of the incident light into leaky modes in nanowires. This comparison is motivated by the results of dark-field scattering measurements on vertical InP nanowires that reveal Mie behavior. We find that the Mie theory is not sufficient to describe the absorption in finite vertical nanowires over a broad range of angles. Nanowires absorb light efficiently when illuminated parallel to their axes. We demonstrate that the light incident from the direction parallel to the axis of a finite nanowire is efficiently absorbed by the coupling to a guided mode. This constitutes the first demonstration of the relative Mie- and guided-mode absorption efficiency in individual nanowires.

6.1 The relevance of angle-dependent absorption for photovoltaics

Semiconductor nanowires have attracted much of research interest as building blocks for novel photovoltaic devices [30–34, 48, 52]. Due to their small dimensions comparable to the optical wavelengths, nanowires support optical resonances. In this way, these resonant nanostructures have proven to be efficient light absorbers whose absorption can be tuned by modifying the nanowire geometry [42, 43, 45–47]. Additionally, nanowires of expensive materials, such as III/V semiconductors, can be also grown on top of cheap substrates, such as Si or Ge [13–15, 164]. Therefore, the use of nanowires could reduce the material consumption and the cost of the devices. Bottom-up fabrication techniques make it possible to grow nanowires with embedded heterostructures, [21, 22, 66] or p-n junctions in nanowires [7, 48]. Ultimately, several p-n junctions incorporated in individual nanowires are hoped to provide material- and energy-efficient nanowire-based solar cells [51–53]. In order to optimize light absorption in such devices, we need to understand the absorption mechanisms in their individual building blocks, i.e., in semiconductor nanowires.

Despite extensive investigations on light absorption by nanowires and nanowire solar cells [81, 113, 114, 165], the research so far has focused mainly on the spectral and polarization response of these nanostructures. Many studies have considered nanowires of circular cross sections illuminated perpendicularly to their axis as leaky waveguides or Mie scatterers [39–41]. In this case, light absorption is typically studied for light incident perpendicularly to the axis of the nanowire that lies on a substrate. Finite nanowires standing on top of a substrate illuminated from the direction parallel to their axis are referred to as optical nanofibers [44–46], to which the incident light can efficiently couple and be absorbed. Until now, only numerical simulations of angle-dependent absorption in nanowires due to coupling to leaky modes have been discussed [83]. The two limiting cases of light absorption, i.e., parallel and perpendicular nanowires to the incident light, have not been unified so far and their relative influence on the absorptance is yet unknown. To achieve this unification and further optimize nanowire-based photovoltaic devices, the angle-dependent absorption of individual nanowires needs to be experimentally explored.

In this chapter, we present the first measurements of angle-dependent light absorption in individual InP nanowires using time-reversed Fourier microscopy. The nanowires used in the experiment are also examined by measuring the dark-field scattering spectra. Scattering measurements reveal that nanowires behave as individual Mie scatterers. Therefore, we compare the angle-dependent light absorption measurements to the absorption efficiency calculated using Mie theory. We find that the Mie theory fails to describe light absorption in vertical nanowires, for excitation incident from the direction parallel or nearly parallel to the axis of the nanowires. In this case, the absorption in nanowires is much larger than predicted by Mie theory. As the angle of incidence increases, the coupling to guided modes becomes less favorable and the incident light couples preferentially to Mie resonances in the nanowires. These results are important for designing omnidirectional nanowire-based solar cells with optimized efficiency.

6.2 Sample description

Indium phosphide (InP) nanowires used in this work have been grown on top of a (111) InP substrate using the vapor-liquid-solid technique (described in Chapter 1.2) in a metal-organic vapor-phase epitaxy (MOVPE) reactor [1].[1] The nanowires are ordered in arrays of separated nanowires. To achieve this, the positions of the gold catalyst particle have been defined using electron beam lithography. To ensure that the light absorption of individual nanowires is not affected by their neighbors, the distance between the gold catalyst particles was set to 5 μm. The substrate with the gold particles on top was annealed at temperature $T = 660^\circ$ for 10 minutes prior to the growth to remove the native oxide layer and the remaining organic materials from the surface of the sample. Nanowires were grown at $T = 500^\circ$ for 25 minutes under trimethylindium (TMIn) and phosphine (PH_3) flow.

During nanowire growth a small additional flow of hydrogen chloride (HCl) was introduced together with TMIn and PH_3 [140]. The HCl provided an in-situ etching of the nanowire material and reduced tapering that commonly occurs in the growth [66, 69, 155, 166]. As can be appreciated in the scanning electron microscope (SEM) image shown in Figure 6.1, the nanowires have an average diameter of about $d = 100$ nm and a length of about $l = 3.13$ μm. The diameter of different nanowires in array varies between 90 and 110 nm. The nanowires are surrounded by air.

6.3 Dark-field confocal microscopy

Prior to angle-dependent absorption measurements, we investigated dark-field light scattering of vertical InP nanowires to prove the existence of Mie resonances in these nanowires. For these measurements we have used confocal microscopy. A confocal microscope is equipped with a small pinhole in the image plane, called a confocal pinhole. This pinhole transmits light originating only from nearly a diffraction-limited spot area in the sample. In this way, only a small selected area of the sample can be illuminated and only light scattered from this area is analyzed. This capability provides an increased signal-to-noise ratio compared to conventional microscopes. Large signal-to-noise ratio is crucial for measuring very small particles, such as nanowires. Since confocal imaging captures a very small area of the image plane at a time, measuring signals from a larger field of view requires a scanning procedure. This is typically an automated procedure

---

[1] The nanowires were grown by T. Zehender under supervision of E.P.A.M. Bakkers at Philips Research Laboratories in Eindhoven.

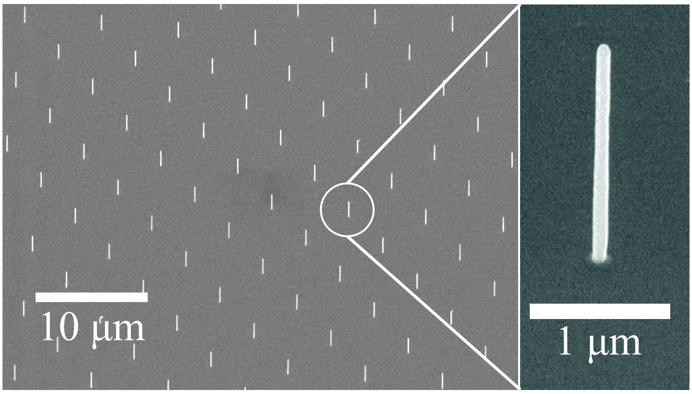

Figure 6.1: Scanning Electron Microscope image taken at an inclination of 30° of InP nanowire array grown on top of an InP substrate. The array of nanowires has a pitch of 5 μm. Individual nanowires in this array are ≈ 3 μm long and have diameters between 90 and 110 nm with nearly no tapering.

where the field of view, exposure time and pinhole size can be defined. Decreasing the size of the pinhole will result in a better spatial resolution at the cost of the signal intensity.

The confocal microscope setup is used in the dark-field configuration. The basic idea of dark-field microscopy is that the specular reflection from the sample is filtered out from the image. The detector only collects light that is scattered from the sample in non-specular directions. The measured signal corresponds to the contrast in scattering efficiency of different species in the sample. The dark-field configuration is achieved by using a dark-field condenser, schematically shown in Figure 6.2. This figure shows the light propagation in case of illumination and collection of the sample. In Figure 6.2(a) the illumination part is shown. A disc in the middle of the beam blocks almost all the incident light except for a small ring on the edge. This ring is guided to the objective by a 50-50 beam splitter. Light incident that way will be focused on the sample with a certain range of incident angles that can be associated with the numerical aperture (NA) of the objective lens. For the ×50 objective used for the scattering measurements, the NA is 0.75, this corresponds to a range of incident angles between 45° and 50°. Figure 6.2(b) shows the scattered light from the sample that goes to the detector. The dark-gray area corresponds to the specular reflection and the light-gray area represents all the higher order scattered light that reaches the objective. After passing through the beam splitter the specular reflection is blocked by a ring. This ring is complementary to the part of the beam that was not blocked by the dark-field disc in the illumination.

The confocal microscope setup used for the dark-field scattering measurements is based on a conventional Leica DM/LM microscope. Attached to this microscope is a Nikon C1 D-eclipse confocal scanning head that consists of the confocal pinhole and a set of piezoelectrically-driven scanning mirrors that scan the illumination and detection area

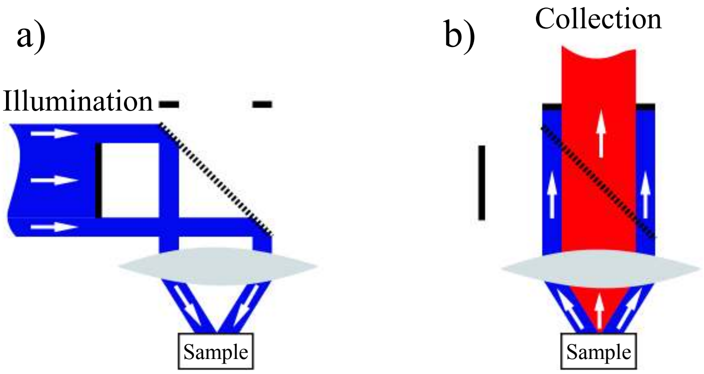

Figure 6.2: Schematics of a dark-field microscope condenser. In (a) the incident light path is shown in dark-gray. In (b), the path of the collection is shown with the specular reflection in dark-gray and the scattered light in light-gray.

over the field of view of the objective. From this confocal scanning head the light is directed to either a sensitive Nikon C1 DUT photomultiplier tube (PMT) or an Andor iDus spectrometer. A schematic of the setup is shown in Figure 6.3. The two detection systems in the setup, the PMT and the spectrometer are used simultaneously. The PMT is used to make an image of the sample from which the current field of view is determined, while the spectrometer is used to analyze the spectrum of the scattered light from the sample. Because of the high sensitivity of the PMT, a beam splitter is used to send 10% of the signal to the PMT and 90% to the spectrometer.

For a good comparison of the measured scattering spectra with the calculated scattering efficiencies, the collected dark-field intensity I_{scat} is divided by the normalized spectrum of the white light source illuminating the sample in a standard, bright field (BF) mode $I_{\text{BF}}^{\text{source}}$. The spectrum of the white light can be obtained by analyzing the reflectance of a mirror placed under the microscope objective. In this way, we correct for any spectral features present in the illumination. The corrected scattered intensity I_{scat} is thus given by

$$I_{\text{scat}} = \frac{I_{\text{DF}}}{I_{BF}^{\text{source}}} \tag{6.1}$$

6.4 Time-reversed Fourier microscopy for measurements of the angle-dependent absorption in nanowires

We have measured angle- and polarization-dependent light absorption of individual nanowires using time-reversed Fourier microscopy described in Chapter 3. In this technique we focus a polarized laser beam at the back focal plane (BFP) of a microscope

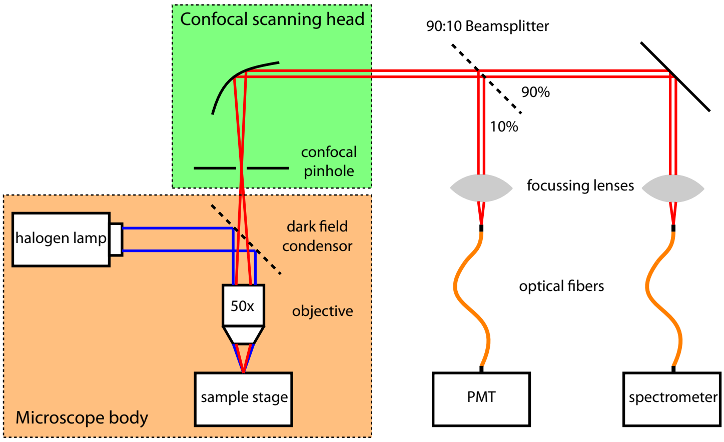

Figure 6.3: Schematics of the confocal microscope used to measure the dark-field scattering spectra of InP nanowires.

objective. This results in a plane wave illumination of the investigated sample placed under a microscope objective. The position of the focused laser spot in the BFP of the objective determines the angle of plane wave incidence on the sample. Scanning the position of this focused spot in the BFP with a motorized stage provides the control of the angle of incidence on the sample. The p- or s-polarized excitation is achieved by scanning the position of the laser spot in the diameter of the BFP along the direction parallel or perpendicular to the polarization vector of the laser beam, respectively.

We have used a ×100 Leica PL APO microscope objective with the numerical aperture (NA) of 0.95. The large numerical aperture of this objective allowed the angles of incidence of up to about 70°. For the excitation of InP nanowires we have chosen to use a diode-pumped solid state laser with a wavelength of $\lambda = 532$ nm. This wavelength is well absorbed in InP. The intrinsic power of the laser beam was about 60 mW. Under the microscope objective the power of illumination at normal incidence was about 0.2 mW. Due to the cylindrical symmetry of nanowires, we do not scan the whole NA of the microscope objective, but only perform a line scan. This line scan corresponds to the angles of incidence in the range of $\theta \in (0^\circ, 90^\circ)$ for a fixed azimuthal angle φ. Here, θ is measured from the direction defined by the long axis of the nanowires. The intensity and angle of the incident light have been calibrated using a flat InP substrate. The exact calibration procedure is described in Chapter 3.4.4

The angle-dependent absorption in individual nanowires is probed by analyzing the intensity of photoluminescence (PL) emission excited as a function of angle of incidence. Since we use low excitation powers, light absorption in the nanowires is a linear process. Therefore, the intensity of the emitted PL is directly proportional to the absorptance of

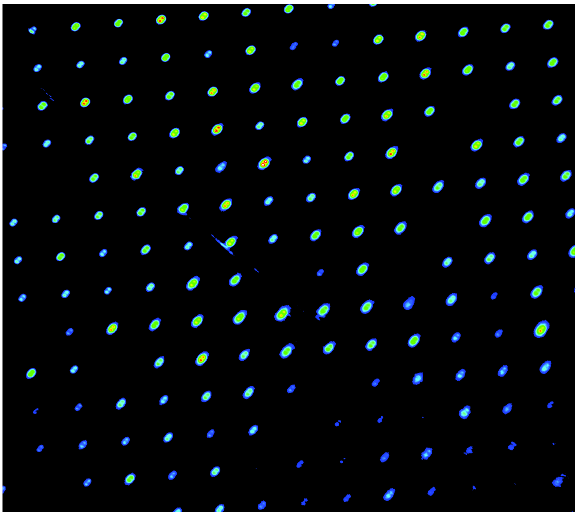

Figure 6.4: PL collected from the InP nanowires arranged in a square array. The image is made with a high resolution Andor Luca R EMCCD camera placed in the image-plane of the microscope.

the nanowires. The PL spectrum is analyzed using Andor Shamrock 303i spectrograph equipped with Andor iDus DU420A BR-DD CCD detector. The excitation wavelength was filtered with a 550 nm long-pass filter.

In the time-reversed Fourier microscope the sample is illuminated with a Gaussian beam. It is not possible to restrict the illumination only to a single wire. Instead, a large area of the nanowire array is illuminated. This illumination can be demonstrated by real-space imaging the PL from the nanowires using a CCD camera. Such image of the PL from excited nanowires can be appreciated in Figure 6.4. Due to the large separation of the nanowires in the array, they are not optically coupled. This means that each nanowire absorbs and emits light individually, independently of the other nanowires. In this way we can study the angle-dependent absorption in individual nanowires.

6.5 Dark-field scattering of vertical InP nanowires

To study the light scattering of vertical InP nanowires we have used the dark-field confocal microscopy described above. We used unpolarized white light from a halogen lamp to illuminate the sample. In dark-field illumination the edge of the objective is used to focus light on the sample. This type of illumination provides a range of the angles θ incident on the sample, regardless of the azimuthal incident angle φ. With the objective of NA = 0.75 used in the measurements, the range of the angles of incidence on the nanowires is estimated to be in the range of 45° to 50°. Due to the cylindrical symmetry of nanowires, only the angle between the wave vector of the incident plane wave and the nanowire axis θ is considered regardless of φ. This is schematically illustrated in Figure 6.5.

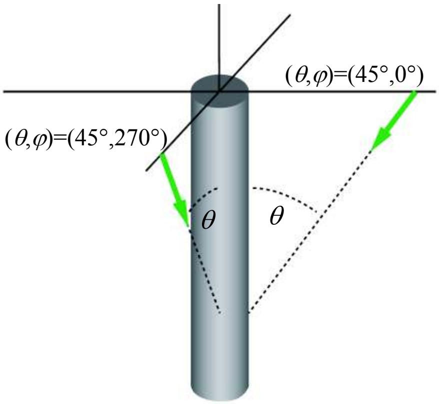

Figure 6.5: Schematic of the experimental geometry in case of a vertical nanowire. Direction of light incidence is defined by two angles, θ and φ. Two cases in terms of the incident angle θ are shown with the wave vector indicated by the green arrow.

To describe the expected scattering properties of InP nanowires, we use Mie theory described in Chapter 2.2 to calculate the scattering efficiency for unpolarized incident light. Calculations take into account the dispersive, complex refractive index of InP given in Ref. [167]. Figure 6.6 shows the scattering efficiency calculated for the limiting angles of dark-field illumination, i.e., $\theta = 45°$ (solid lines) and $\theta = 50°$ (dashed lines) and for the thinnest and thickest nanowires present in the sample, namely d = 90 nm (black lines), and d = 110 nm (red lines). While the scattering efficiency of InP nanowires is similar for the two limiting angles of incidence, the diameter of nanowires greatly influences the scattering properties of nanowires. The peak of the scattering efficiency at $\lambda \approx 520$ nm for d = 90 nm shifts to $\lambda \approx 600$ nm for a 110 nm-thick cylinder. The range of the angles of incidence well as the diameter distribution of nanowires in the sample is taken into account in further analysis of the scattering by nanowires.

Thanks to the high spatial resolution achieved by the confocal microscope, it is possible to limit the field of view to a single nanowire in the 5 μm pitched array. The measured scattered intensity from a single nanowire is shown in Figure 6.7(a). The spectrum, indicated by the black circles, shows one broad peak centered at $\lambda \approx 580$ nm. We compare this measured scattered intensity to the scattering efficiency of an infinitely long InP cylinder surrounded by air, calculated using Mie theory. The scattering efficiency of a 110 nm-thick InP cylinder provided the best fit for the single nanowire measurements. This calculation is represented by the red line in Figure 6.7(a). Remarkably, in spite of the large amount of works investigating light scattering and absorption of horizontal nanowires, this is the first time that the scattering spectra of vertical semiconductor nanowires have

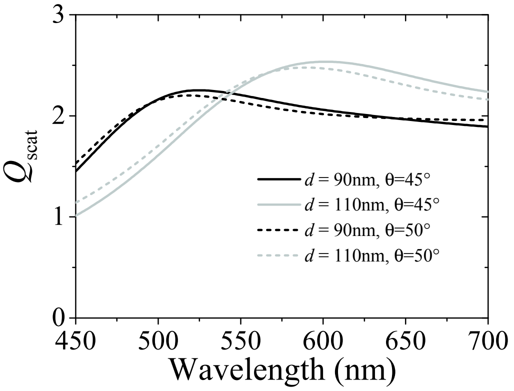

Figure 6.6: Calculation of the scattering efficiency as a function of the wavelength for θ = 45° (solid lines) and θ = 50° (dashed lines) and for diameter of d = 90 nm (black lines) and d = 110 nm (gray lines). These two angles limit the dark-field illumination, while the two different diameters correspond to the thinnest and the thickest nanowires present in the array. The cylinders are assumed to be illuminated with unpolarized light.

been compared to Mie theory.

The scattering measurements on InP nanowires have also been performed for larger areas that contain more nanowires. The field of view of the confocal scan was expanded to fit an array of 6x6 nanowires. The result of this measurement is shown in figure 6.7(b) with the black circles. The measured peak is broader than the peak obtained for a single wire. This broadening can be attributed to the variations in the nanowire diameter. The calculated scattering efficiency, plotted with red line, the diameter of the cylinder is averaged between 90 nm and 110 nm with equal weights. The good agreement between the measured data and the calculated scattering efficiency supports the claim that the diameter is not completely uniform over the sample. Most importantly, these measurements show that the nanowires in the array behave as individual Mie scatterers.

6.6 Angle-dependent absorption in vertical InP nanowires measured with time-reversed Fourier microscopy

The angle-dependent absorption measurements have been performed using the time-reversed Fourier microscope described in Chapter 3. Figure 6.8 displays a schematic representation of the experimental configuration. The incident angle θ is shown in figure 6.8(a) as the angle between the nanowire axis and the incident wave vector. Figures 6.8(b) and (c) show the orientation of the electric and the magnetic fields in case for p- and s-polarized incident light, respectively.

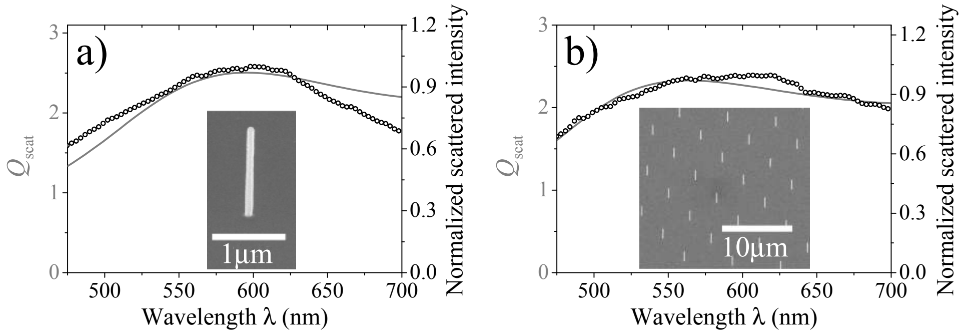

Figure 6.7: Measurements of the scattered intensity from vertical InP nanowires are indicated with the black circles. (a) Scattered intensity for a single wire, (b) scattered intensity for an array of 6x6 nanowires. The calculations of the scattering efficiency obtained from Mie theory are represented by the gray solid lines and correspond to the left vertical scale in each plot. The scattering efficiency in (a) has been calculated for a single cylinder with a diameter of d = 110 nm. The scattering efficiency shown in (b) has been averaged over diameters between 90 nm and 110 nm with equal weights to account for the distribution of nanowire diameters in the sample.

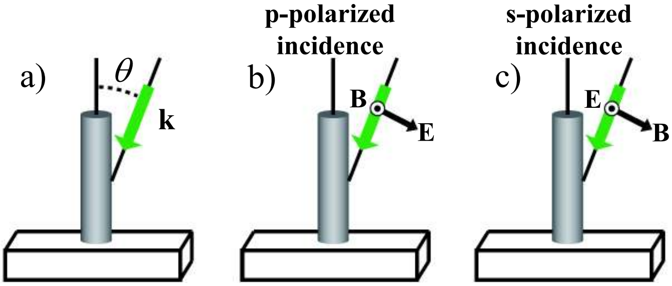

Figure 6.8: Schematic representation of the measurement geometry. (a) The definition of the angle of incidence. In (b) and (c) the electric and magnetic fields orientations are shown for p- and s- polarization, respectively. The green arrow in the plots represents the incident wave vector.

We excited the nanowires using a λ = 532 nm diode-pumped solid state laser. The absorption in nanowires is probed by analyzing the PL intensity that is directly proportional to the absorptance in nanowires. The PL emission spectra of the nanowires have been recorded as a function of the angle of incidence θ for p- and s-polarized excitation. The exemplary spectra taken upon p-polarized excitation of nanowires at θ = 0° and θ = 70° are shown in Figures 6.9(a) and (b), respectively. The corresponding PL spectra of nanowire emission excited with s-polarized light at the same angles of incidence are shown in Figures 6.9(c) and (d). The angle θ = 0° corresponds to the incidence parallel to the nanowire axis, while $\theta = 70°$ is the largest angle of incidence allowed by the numerical aperture of the microscope objective used for the measurements.

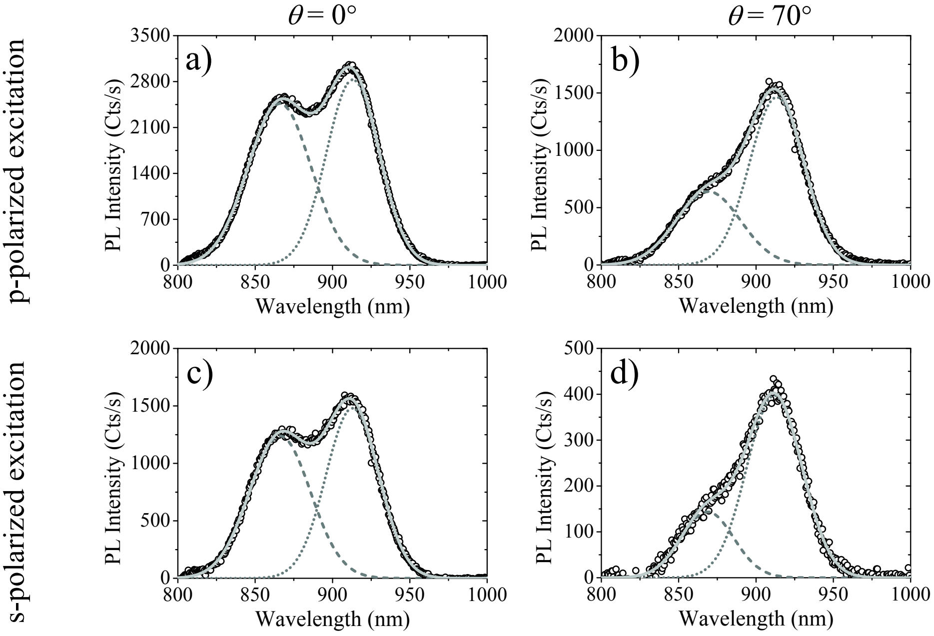

Figure 6.9: PL spectra of the InP nanowire emission. (a) PL spectrum of nanowires excited with p-polarized, normally incident light ($\theta = 0°$). (b) PL spectrum of nanowires excited with p-polarized at $\theta = 70°$. (c) PL spectrum of nanowires excited with s-polarized, normally incident light. (d) PL spectrum of nanowires excited with s-polarized at $\theta = 70°$.

The InP nanowires grow preferentially in the wurtzite crystal structure on top of the zincblende InP substrate [68]. Since the electronic band gap of InP in the wurtzite phase at room temperature is larger by around 50 meV than that of zincblende, the emission peak of wurtzite nanowires is blue-shifted compared to that of the substrate [67]. The maximum emission of the zincblende InP substrate is at $\lambda \approx 911$ nm while the maximum emission of nanowires is at around $\lambda = 870$ nm. Due to the fact that the measurements were performed at room temperature, the emission peaks are broad and show a large mutual overlap. To make a clear distinction between the emission of nanowires and the emission of the substrate, each spectrum has been fitted with a double Gaussian. A Gaussian fit is chosen because it represents the emission in the case of inhomogeneous broadening resulting from the local variations of the semiconductor band structure due to impurities and defects. The measured spectra shown in Figures 6.9 can be accurately fitted with the double Gaussian function represented with the light-gray solid line. The two constituting Gaussians for each fit are shown with the dark-gray dashed lines and dotted lines for the nanowire emission and the substrate emission, respectively. The width, height and peak position have been taken as the fit parameters for the individual Gaussians.

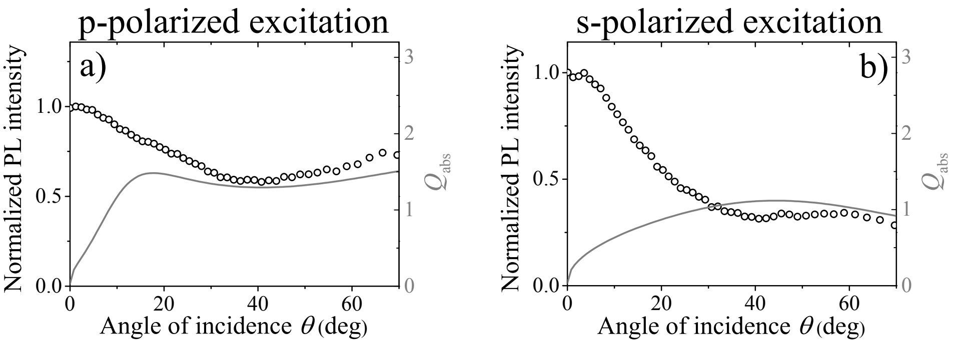

Figure 6.10: The peak PL emission intensity of nanowires excited with p- (a) and s-polarized (b) light as a function of the angle incidence (black circles). The measured PL intensity has been normalized to the values at $\theta = 0°$. The solid lines represent the calculated absorption efficiency using Mie theory for infinitely long InP cylinders. This absorption efficiency has been averaged for cylinder diameters between 90 and 110 nm.

The intensities of the nanowire emission as a function of the excitation angle and polarization have been extracted from the height of the Gaussian peak centered at 870 nm. To account for the response of the setup, the extracted intensities have been multiplied with the correction function (instrumental response function) described in Chapter 3.4.4. The corrected intensity is plotted as a function of the incident angle of illumination in Fig. 6.10.

Figures 6.10(a) and (b) show the normalized peak intensities of nanowire emission as a function of the angle of incidence for p- and s-polarized excitation, respectively. The solid lines in Figures 6.10(a) and (b) show the calculated absorption efficiency from Mie theory for p- and s-polarized incident light, respectively. These absorption efficiencies have been averaged for cylinder diameters between 90 nm and 110 nm with equal weights. The comparison of the measurements and calculations show that Mie theory is not sufficient to describe the absorption of the vertically oriented nanowires. At large incident angles there is an agreement between the trend in the measured PL intensity and the calculated absorption efficiencies. At small angles of incidence ($\theta \lesssim 30°$), the calculated absorption efficiency decreases to zero for both polarizations. The measurements reveal the opposite effect, i.e., the PL intensity has a maximum at normal incidence which is in contradiction to Mie theory. We attribute this effect to the finite character of the nanowires in the experiment.

Mie resonances quantify the coupling of incident plane waves to leaky modes supported in the nanowire. At large angles of incidence the coupling to Mie resonances is the dominant process. However, for small angles, light couples to the nanowire from the top in a different way. Light incident parallel to the axis of a finite nanowire can couple to the fundamental HE_{11} guided mode[44, 45]. The absorption of light coupled to guided modes depends strongly on the diameter of the nanowire [47]. Such coupling is not taken into account in Mie theory due to large phase mismatch between the plane wave illuminating an infinitely long cylinder and guided modes supported by this cylinder (see Chapter 2). To reproduce the angle-dependent light absorption in finite-length nanowires, accurate numerical simulations should be performed.

6.7 Numerical simulations

To explain the origin of the strong light absorption in nanowires at $\theta = 0°$ we use finite-element method (FEM) simulations with COMSOL, as described in Appendix A.[2] The nanowire in the simulations is 3.13 μm long, has a diameter of 100 nm and stands on top of an InP substrate. This wire is illuminated with a plane wave of λ = 532 nm. Figures 6.11(a) and (b) display the amplitude of the simulated electric field around the nanowire when the incident light is polarized in the plane of the plot (polarization along y-direction) and out of this plane (polarization along x-direction), respectively. From these plots of the electric field amplitude it appears that the incident light is coupled to a mode in the nanowire and guided toward the substrate. The amplitude of the simulated electric field components in the cross sections z_1 and z_2 of the nanowire are plotted in Figures 6.11(c), (d) and (e). We compare these patterns of the amplitude of the electric field components with the ones calculated analytically for the fundamental HE_{11} guided mode supported by an infinitely long cylinder of the same diameter with a real component of the refractive index of InP, and for the wavelength of λ = 532 nm (Figures 6.11(f), (g) and (h)). From the comparison of the simulated amplitudes and the analytically calculated electric field profiles of the HE_{11} guided mode it is evident that the light incident parallel to the axis of the finite nanowire couples to the fundamental guided mode supported by the geometry of the nanowire. At larger angles of incidence the coupling of the incident plane wave to guide modes weakens and the excitation of the Mie resonances dominates.

6.8 Conclusions

We have used time-reversed Fourier microscopy to measure the angle-dependent light absorption in individual vertical InP nanowires. These are the first reported measurements of angle-dependent absorption in individual nanowires. Motivated by the dark-field scattering results, we have compared the angle-dependent absorption to Mie theory.

---

[2] The simulations were performed by Ramón Paniagua-Domınguez and José A. Sánchez-Gil from the Institute for Structure of Matter (IEM-CSIC) in Madrid, Spain

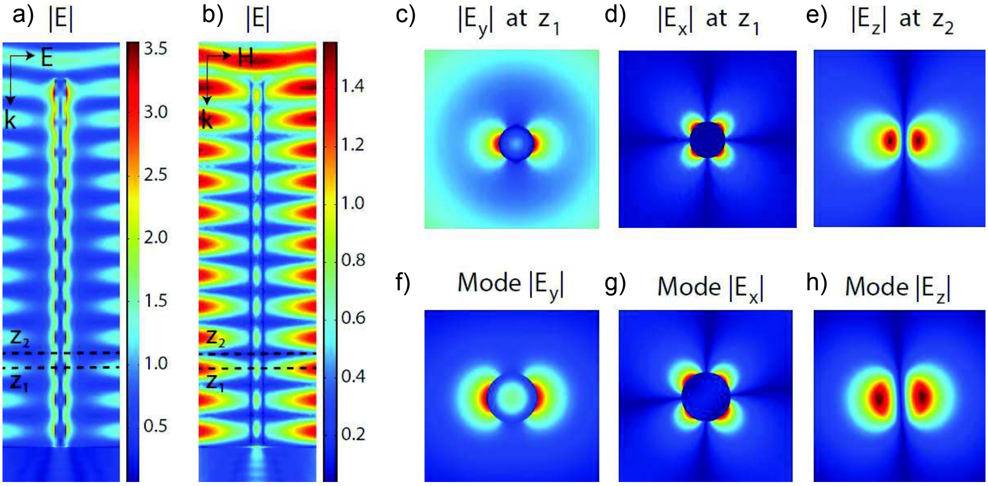

Figure 6.11: Amplitude of the electric field around an InP nanowire standing on top of the InP substrate excited with a plane wave with a wavelength of 532 nm and the polarization vector in plane of the nanowire's cross section, along y-direction (a) and out of plane of this cross section, along the x-direction (b). The nanowire is 3.13 μm-long and has a diameter of 100 nm. (c), (d) and (e) illustrate the magnitude of the electric field components in the horizontal cross sections z_1 and z_2 in (a). (f), (g) and (h) show the electric field components of the HE_{11} mode calculated analytically.

We have found that Mie theory does not describe well the angle-dependent absorption in vertical nanowires, especially at small angles of incidence measured from the nanowire axis. With the help of numerical simulations we demonstrate that, at normal incidence, light efficiently couples to HE_{11} guided mode in finite nanowires. As the angle of incidence increases, the coupling to the HE_{11} guided mode becomes less favorable and the coupling to Mie resonances dominates. Our results are important for designing nanowire-based solar cells, where designing the angle-sensitivity to absorption is important to optimize the performance of such devices.

CHAPTER 7

EFFECTIVE MEDIUM FORMED BY POLYDISPERSE MIE-SCATTERING NANOWIRES

We present an experimental and theoretical study of the angle- and polarization-dependent light extinction in random arrays of polydisperse semiconductor nanowires epitaxially grown on substrates. The specular reflectance is described by averaging the scattering properties of individual nanowires obtained from Mie theory over the diameter distribution. The complex effective refractive index describing the propagation and attenuation of the coherent beam scattered in a forward direction is determined in the independent scattering approximation and used to calculate the angle- and polarization- dependent reflectance. Our measurements demonstrate the highly anisotropic scattering in ensembles of aligned nanowires.

7.1 Introduction

Progress in the growth and doping of semiconductor nanowires has led to an increased interest on these nanostructures. This interest has been driven by the promising perspectives of nanowires in applications such as nano-light-emitting diodes [10], lasers [133, 163], single-photon sources [24] and solar cells [30]. On a more fundamental level, semiconductor nanowires are also being intensively investigated for their unique optical properties. The optical anisotropy in the polarized emission and absorption by individual nanowires, associated to their large geometrical anisotropy, was first reported and described by Wang et al. [168] However, this description was based on the quasistatic approximation, which assumes a uniform electromagnetic field amplitude over the cross section of the nanowire. At optical frequencies, this approximation is valid for nanowires with a diameter smaller than 10 nm [169]. Optical retardation in nanowires with larger diameters requires a more elaborated modeling of their optical properties. Van Weert et al. suggested that the Mie scattering theory for infinitely long circular cylinders could be applied to describe more precisely the absorption and emission anisotropies of semiconductor nanowires [38]. Mie scattering theory has been used by Cao et al. to describe the resonant enhancement of the absorption by individual nanowires [39]. This enhancement has been also proposed to increase the efficiency of nanowire-based thin film solar cells [40]. Most of the suggested applications will rely on periodic and random arrays of nanowires instead of on single nanostructures. Therefore, the description of the light propagation, scattering and absorption in these arrays is becoming increasingly important. Light propagation in ordered arrays of nanowires is usually described by calculating the eigenmodes of periodic structures [19] or by numerical simulations [31, 48, 81], while random ensembles of very thin nanowires are often described by effective medium theories assuming their dipolar optical response. Recent achievements in this direction are the demonstration of giant birefringence in dense arrays of nanowires [153], the demonstration of graded index layers with minimum reflection formed by nanowires grown on top of substrates [170, 171], the proposal of photonic crystal nanowire structures for enhanced absorption in photovoltaic applications [45, 52, 172, 173], and the description of multiple scattering in random mats of semiconductor nanowires [73, 174, 175].

In this chapter, we use the Mie theory in the independent scattering approximation to describe the anisotropic scattering and extinction of light in a random ensemble of epitaxially grown Si nanowires with diameters comparable to the wavelength. This analytical model allows us to determine the effective index of refraction and extinction coefficients, describing the propagation of the beam scattered in the forward direction. This beam is also called the coherent beam in contrast to the diffuse light that results from multiple scattering in the sample [176]. The approach is valid in the low scatter-density limit, which is the case for the investigated sample that consists of nanowires with a volume filling fraction of $\alpha \cong 0.025$. The real component of the effective refractive index is close to unity as expected from the low nanowire filling fraction. The imaginary component, defining the extinction length, is highly anisotropic and wavelength dependent. At long wavelengths and large angles of incidence the extinction length for s-polarization is more than three times larger than for p-polarization and solely determined by scattering in the nanowire layer. The calculated specular reflectance using the effective medium optical constants is in excellent agreement with the measurements. In this way we provide a relatively simple analytical formalism to describe the extinction properties of complex arrays of polydisperse nanowires beyond the dipolar approximation. Development of such formalism facilitates the design of light scattering and absorption in ensembles of nanowires for, e.g., photovoltaic applications.

7.2 Independent scattering approximation for an effective medium composed of Mie-scatterers

Dielectric mixing rules provide the value of the effective medium optical constants, e.g., the complex refractive index, $\tilde{n}_{\text{eff}} = n_{\text{eff}} + ik_{\text{eff}}$, characterizing the electromagnetic response of heterogeneous materials formed by two or more different constituents. These effective medium constants describe the phase and amplitude of an optical beam propagating through the medium as if it was homogeneous with a response that it is given by that of its constituents and their filling fraction. If the medium is formed by particles or scatterers with a size much smaller than the wavelength λ of light, they create a perturbation of the field that in the lowest order is that of a dipole. In this case, the effective refractive index is calculated in the quasistatic approximation. The simplest mixing rule in the quasistatic limit is the well-known Maxwell-Garnett formula, which considers small dipolar spheres embedded in a matrix.

As the size of the particles increases, their optical response cannot be approximated by that of dipolar spheres. To calculate the effective medium response, the multipolar response of individual particles in the ensemble must be considered. The far field radiation scattered by a particle of dimension r in any direction defined by the angles Θ and Φ in spherical coordinates, when illuminated by light of wavelength λ from a direction defined by the angles θ and φ, is described by the amplitude scattering function $S(\Theta, \Phi, r, \theta, \varphi, \lambda)$ of the particle. This complex scattering function contains information about the amplitude (real component) and phase (imaginary component) of the scattered wave. The extinction of light, which is the result of the scattering and absorption, is defined as the decrease of the electric field amplitude in the direction of propagation. Therefore, the optical extinction produced by a scatterer is related to the amplitude scattering function at $\Theta = \pi + \theta$ and $\Phi = \pi + \varphi$, which for simplicity we denote as $S_0(r, \theta, \varphi, \lambda)$.

The optical extinction in an ensemble of finite particles in the independent scattering approximation is given by the sum of the amplitude scattering functions of the individual particles. The independent scattering approximation is valid for scattering samples with a low density of scatterers. This approximation neglects the probability that the scattered light by one particle returns to the particle after being scattered somewhere else in the sample. As we will show later, this condition is fulfilled by our sample with a nanowire volume filling fraction of 0.025. For an ensemble of polydisperse scatterers, it is necessary to weigh the amplitude scattering functions using the normalized particle size distribution function $p(r)$ describing the polydispersity

$$\overline{S_0(\theta,\varphi,\lambda)} = \int_0^\infty p(r) S_0(r,\theta,\varphi,\lambda)\, dr. \tag{7.1}$$

The propagation of the coherent beam is given by the sum of the scattered amplitudes in the forward direction from the individual particles. This propagation can be described as the propagation in a homogeneous medium with an effective complex refractive index given by [85]

$$\tilde{n}_{\mathrm{eff}}(\lambda,\theta) = 1 + i\frac{2\pi\rho_V}{k^3}\overline{S_0(\theta,\varphi,\lambda)}, \tag{7.2}$$

where ρ_V is the density of scatterers and $k = \frac{2\pi}{\lambda}$ is the wave number in vacuum. Therefore, the determination of the effective refractive index for the coherent beam is reduced to the determination of the amplitude scattering function of the scatterers. The real component of this index defines the phase delay or advance in the propagation of the coherent beam through the scattering medium. The imaginary component defines the effective extinction coefficient that describes the attenuation of the amplitude in the forward direction due to absorption and scattering. It is important to note that the spatial dispersion in the heterogeneous medium introduced by the scatterers gives rise to an anisotropic response. This response translates into an angle-dependent effective refractive index.

The scattering properties of nanowires can be calculated using the Mie theory [77] that has been discussed in Chapter 2.2. This theory describes the light scattering by an individual, infinitely long circular cylinder. By expanding the incident and scattered fields into cylindrical harmonics it is possible to calculate the amplitude scattering function for such a scatterer. The amplitude scattering function depends on the radius of the cylinder r, the angles of incidence θ and φ, the wavelength λ and the polarization of the incident light. If the electric field vector of the incident wave oscillates in plane that contains the incident **k**-vector and the axis of the cylinder, the incident light is p-polarized. In case the electric field vector oscillates perpendicular to this plane, the illumination is s-polarized. To distinguish the amplitude scattering function in the forward direction of an infinitely long cylinder from its counterpart of a particle, we denote it as $T_0^{p,s}(r,\theta,\varphi,\lambda)$.

Semiconductor nanowires have a finite length. For nanowire lengths much longer than their diameter, $l \gg 2r$, and at large distances from the nanowire, $z \gg \frac{l^2}{\lambda}$, the amplitude scattering function of nanowires with a finite length be approximated to the Mie amplitude scattering function of infinitely long cylinders. In that case, the amplitude scattering function in the forward direction of finite particles is related to the amplitude scattering function in forward direction of infinite cylinders by [85]

$$\overline{S_0^{\mathrm{p,s}}(\theta,\varphi,\lambda)} \cong \frac{kl}{\pi}\overline{T_0^{\mathrm{p,s}}(\theta,\varphi,\lambda)}, \tag{7.3}$$

where $\overline{T_0^{\mathrm{p,s}}(\theta,\varphi,\lambda)}$ is the weighted Mie scattering function in the forward direction for cylinders. The nonweighted amplitude scattering functions for both polarizations (p, s) are infinite series of the scattering coefficients

$$T_0^{\mathrm{p}}(r,\theta,\varphi,\lambda) = b_0^{\mathrm{p}} + 2\sum_{n=1}^{\infty} b_n^{\mathrm{p}}, \tag{7.4a}$$

$$T_0^{\mathrm{s}}(r,\theta,\varphi,\lambda) = a_0^{\mathrm{s}} + 2\sum_{n=1}^{\infty} a_n^{\mathrm{s}}. \tag{7.4b}$$

The scattering coefficients are functions of the cylinder's radius, angle of incidence, wavelength and material constants. Explicit mathematical expressions of these coefficients can be found in Chapter 2.2 and Ref. [77].

The effective complex refractive index for the p- and s-polarized coherent beam propagating in an ensemble of vertically aligned nanowires is given by

$$\tilde{n}_{\mathrm{eff}}^{\mathrm{p,s}}(\lambda,\theta) = 1 + i\frac{2\pi\rho_V l}{k^2}\overline{T_0^{\mathrm{p,s}}(\theta,\varphi,\lambda)}, \tag{7.5}$$

where the density of scatterers is related to the volume filling fraction α by

$$\rho_V = \frac{N}{V} = \frac{\alpha}{\pi l}\frac{1}{\int_0^{\infty} p(r)r^2 dr}. \tag{7.6}$$

Using this approach, different scatterers can be included in the calculations, such as cylinders with a random and nonvertical orientation. In this way, the additional scatterers have an influence on the real and imaginary components of the effective refractive index. If the polarization-, orientation- and size-averaged amplitude scattering function of nonvertical nanowires is denoted as $\overline{T_0(\lambda)}$, the effective refractive index is given by

$$\tilde{n}_{\mathrm{eff}}^{\mathrm{p,s}}(\lambda,\theta) = 1 + i\frac{\lambda^2}{2\pi^3}\frac{1}{\int_0^{\infty} p(r)r^2 dr}\left(\alpha_{\mathrm{vertical}}\overline{T_0^{\mathrm{p,s}}(\theta,\varphi,\lambda)} + \alpha_{\mathrm{nonvertical}}\overline{T_0(\lambda)}\right), \tag{7.7}$$

where $\alpha_{\mathrm{nonvertical}}$ is the volume filling fraction of nonvertical cylinders. The specular reflectance of the system consisting of the nanowire layer and the semi-infinite Si substrate can be calculated using the transfer matrix method [177]. This method calculates the reflection and transmission coefficients of a multilayered structure. A polarization-independent scattering term can be introduced to account for a reduction of the specular reflection on the interfaces due to surface scattering. The specular reflectance at an interface in the presence of surface roughness scattering R_s is given by [178]

$$R_s = R_0 \mathrm{e}^{-\left(\frac{4\pi\sigma\cos\theta}{\lambda}\right)^2} \tag{7.8}$$

where R_0 is the specular reflectance in the absence of surface scattering and σ is the root mean square height of the surface features causing the roughness.

7.3 Ensemble of silicon nanowires - sample description

We have grown silicon nanowires on top of a silicon substrate using the vapor-liquid-solid (VLS) method, described in Chapter 1.2, in a chemical vapor deposition (CVD) reactor [1].[1] A gold layer with a nominal thickness of 5 nm was evaporated on a single-side polished, n-type silicon (111) substrate. The gold-coated substrate was heated to temperature $T = 650$ °C under vacuum to catalyze the growth of Si nanowires. The nanowires were grown by pyrolyzing silane diluted in 10% H_2 in argon under a gas flow dynamics and a pressure ratio $P_{SiH_4}/P_{H_2} = 33 \times 10^{-3}$. The growth resulted in a random polydisperse ensemble of silicon nanowires. Figure 7.1(a) shows a cross-section scanning electron microscope (SEM) image of a layer of Si nanowires with an average length of 7.3 μm. A SEM image of the tilted sample is shown in Fig. 7.1(b). On top of each nanowire the catalyst particle is clearly visible. The nanowires are aligned preferentially in the (111) direction, with 80% of the wires in the sample in this vertical direction. The overall volume filling fraction of silicon in form of vertical nanowires was estimated to be $\alpha_{\text{vertical}} \cong 0.02$. There is also a small fraction of nonvertical nanowires with a volume fraction $\alpha_{\text{nonvertical}} \cong 0.005$. Also in Fig. 7.1(a) and (b) a significant surface roughness can be observed on the interface between the nanowire layer and the underlying substrate. As we will show later, this roughness leads to additional light scattering and a reduction of the specular reflection.

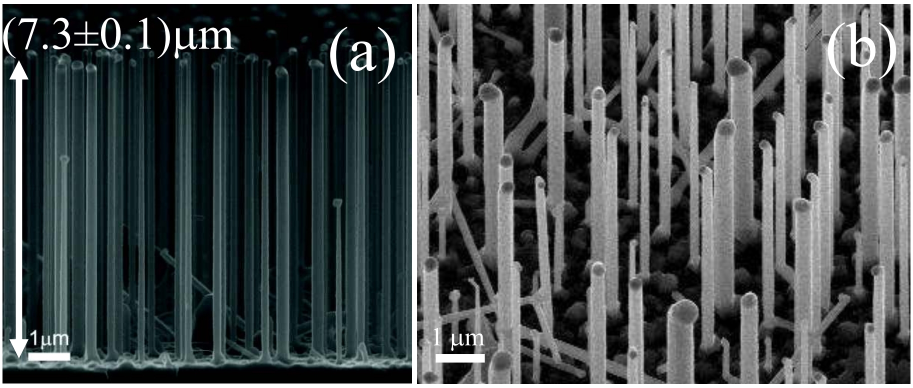

Figure 7.1: Silicon nanowires epitaxially grown on a silicon substrate. (a) SEM image of the cross section of the sample. (b) SEM image of the sample at an inclination of 30°.

The diameter distribution of the nanowires was determined from several SEM images

---

[1] The nanowires were grown by D. Hourlier at the IEMN in Lille (France).

taken on the sample at different places. The histogram displaying this distribution is shown in Fig. 7.2. The diameter distribution can be approximated with a log-normal probability density function with a mean of 182 nm, and standard deviation of 0.4 nm. This probability density function is represented by the black solid line in Fig 7.2. The area under the probability density function was normalized to unity for the calculations. The inset of Fig. 7.2 is a photograph of the sample where the brownish area is occupied by nanowires and the small dark area on the right side of the sample is the silicon wafer, where no nanowires were grown. The region with the nanowires has a matte appearance characteristic of scattering samples.

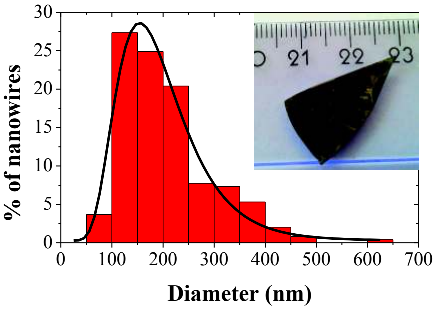

Figure 7.2: Histogram of the percentage distribution of nanowire diameters approximated with a log-normal probability distribution (black solid line). The inset is a photograph of the sample placed on a ruler.

7.4 Reflectance measurements and discussion

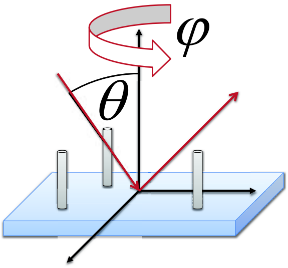

Figure 7.3: Schematic representation of the specular reflectance measurement, where the angles θ and φ are the angle of incidence and the azimuthal angle of the incident beam onto the sample, respectively.

To explore the propagation of the coherent beam through the ensemble of nanowires, the specular reflectance as a function of the wavelength and the angle of incidence was measured for p- and s-polarized light using a coherent supercontinuum light source. This light source provided enough optical power to distinguish with the eye between specularly and diffusively reflected light. A schematic representation of the specular reflectance measurement configuration is displayed in Fig. 7.3. The angle of incidence is defined with respect to the normal of the sample and coincides with the angle θ defining the amplitude scattering function of vertically aligned nanowires. Specular reflection as a function of the wavelength and the angle of incidence is measured by rotating the sample and an optical fiber coupled to a spectrometer. The specular reflectance is the the intensity collected by the detector at different wavelengths and angles of incidence normalized to the wavelength-dependent intensity of light incident directly on the detector. The incident intensity was measured by the spectrometer in the absence of the sample.

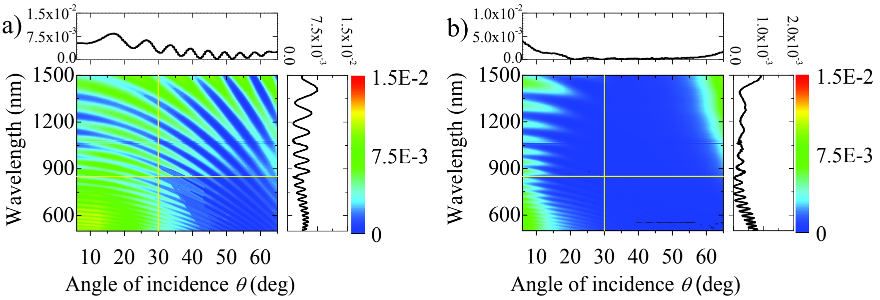

Figure 7.4: Measured specular reflectance as a function of the wavelength and angle of incidence for (a) s-polarized and (b) p-polarized light. The graphs on the top and right sides of each figure are the specular reflectance at $\lambda = 850$ nm and 30°, respectively.

Figures 7.4(a) and (b) show the measurement for s- and p-polarization respectively. Reflection measurements were done to extend the measurement range to higher energies than the band gap of silicon at which absorption in the substrate suppresses the transmission. Fabry-Perót oscillations are visible due to the finite thickness of the nanowire layer and the interference of the light reflected at its upper and lower interfaces. The magnitude of the specular reflectance is very low, below 0.015, which indicates a very large optical extinction in the sample. The reflectance for both polarizations increases for small angles due to the reduction of the optical path length in the scattering layer. At wavelengths longer than the Si band gap wavelength ($\lambda_{\mathrm{Si}} = 1100$ nm) the extinction is caused by scattering out of the beam propagating in the forward direction, while for shorter wavelengths the nanowires can scatter and absorb the intensity of this beam.

To exclude a possible anisotropic response of the sample with respect to the azimuthal angle, φ, we have measured the specular reflectance at $\lambda = 633$ nm at normal incidence as a function of this angle (Fig. 7.5). Because of the cylindrical symmetry of vertical nanowires along their axis, they have an isotropic response when illuminated at normal

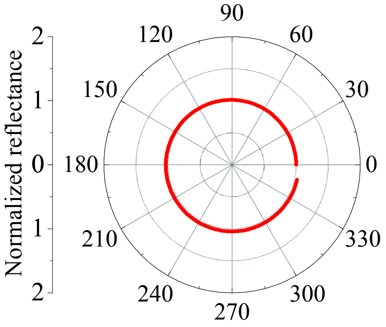

Figure 7.5: Polar plot of the normalized specular reflectance as a function of the azimuthal angle measured at normal incidence with a HeNe laser (λ = 633 nm). The sample was rotated along the axis parallel to the incident beam with steps of 1°. The reflectance is normalized to the value at $\varphi = 0°$.

incidence. Therefore, any possible anisotropic response at this angle of incidence could be attributed to the small fraction of nonvertical nanowires. As can be appreciated in Fig. 7.5, the reflectance does not vary with φ, which indicates that the nonvertical nanowires are not preferentially aligned along any azimuthal angle. Furthermore, we assume that the nonvertical nanowires have a random inclination in order to average the amplitude scattering function over θ and the polarization.

Since the thickness, the fraction of vertical and nonvertical nanowires and the diameter distribution of the nanowires have been determined from the SEM images, we can calculate the effective complex refractive index of the layer describing the propagation and attenuation of the coherent beam by using the Mie model. We consider here two cases: A layer consisting of polydisperse vertical nanowires with a volume filling fraction of $\alpha_{\text{vertical}} \cong 0.02$ and a layer in which there is an additional volume fraction $\alpha_{\text{nonvertical}} \cong 0.005$ of randomly oriented nonvertical nanowires. For determining the angle-, wavelength- and polarization-dependent effective index we use Eq. 7.7, in which the amplitude scattering functions were calculated using the Mie formalism and weighted with the log-normal diameter distribution function shown in Fig. 7.2. As input parameters, we use the radii of the cylinders, angle of incidence, wavelength, and wavelength-dependent refractive index of crystalline silicon obtained from Ref. [167]. Figure 7.6 shows the real and imaginary components of the calculated effective refractive indices for p-polarized (solid and dash-dotted black lines) and s-polarized (dashed and dotted gray lines) light and for three different wavelengths, i.e., λ = 633 nm (a,b), λ = 850 nm (c,d) and λ = 1200 nm (e,f).

The solid and dotted lines represent the calculations for the layer of vertical nanowires, whereas the dashed and dash-dotted lines stand for the ensemble consisting of both

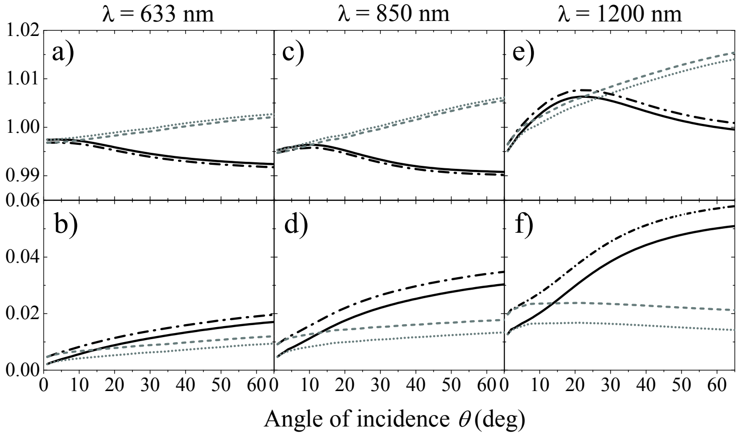

Figure 7.6: Calculated effective (a, c, and e) refractive indices and (b, d, and f) extinction coefficients for the coherent beam in a polydisperse ensemble of silicon nanowires for three wavelengths: (a and b) $\lambda = 633$ nm, (c and d) $\lambda = 850$ nm, and (e and f) $\lambda = 1200$ nm. The calculations for p-polarized (black solid lines) and s-polarized (gray dotted lines) light consider only vertical nanowires with a volume filling fraction $\alpha_{\text{vertical}} \cong 0.02$, whereas the calculations for vertical nanowires with $\alpha_{\text{vertical}} \cong 0.02$ and nonvertical nanowires with $\alpha_{\text{nonvertical}} \cong 0.005$ for p- and s-polarized light are represented by the black dash-dotted lines and the gray dashed lines, respectively.

vertical and nonvertical nanowires. The effective complex refractive index is the same for both polarizations at $\theta = 0°$, where the polarization is indistinguishable because of the cylindrical symmetry of nanowires. The real part of the effective refractive index is close to unity for both polarizations due to the very low volume filling fraction of the nanowires. Such a low refractive index facilitates a broadband and omnidirectional light coupling into the nanowire layer [179]. The resonant behavior of Mie scatterers at wavelengths comparable to their diameter leads to an effective refractive index smaller than unity at short wavelengths and mainly for p-polarized light. The refractive index that is close to, but smaller than, unity means a phase advance of the wave propagating in the forward direction through the low-density medium of resonant scatterers. An elegant description of this phenomenon can be found in Chapter 9 of Ref. [77]. The imaginary component of the effective refractive index, or the effective extinction coefficient, decreases with the angle of incidence because of the reduction of geometrical cross section of the nanowires. Due to larger extinction efficiency of individual nanowires for p-polarized light, the effective extinction coefficients of the ensembles of nanowires are also larger for that polarization compared to s-polarization. This fact, together with the lower Fresnel reflection at the interfaces for p-polarized light, is responsible for the large differences between the intensity of s- and p-polarized light reflected from the sample.

The addition of nonvertical nanowires in the layer modifies the complex effective refractive index. In the case of the real component, the influence of the nonvertical nanowires is small due to low density of the nonvertical nanowires. This influence is much more evident for the effective extinction coefficient.

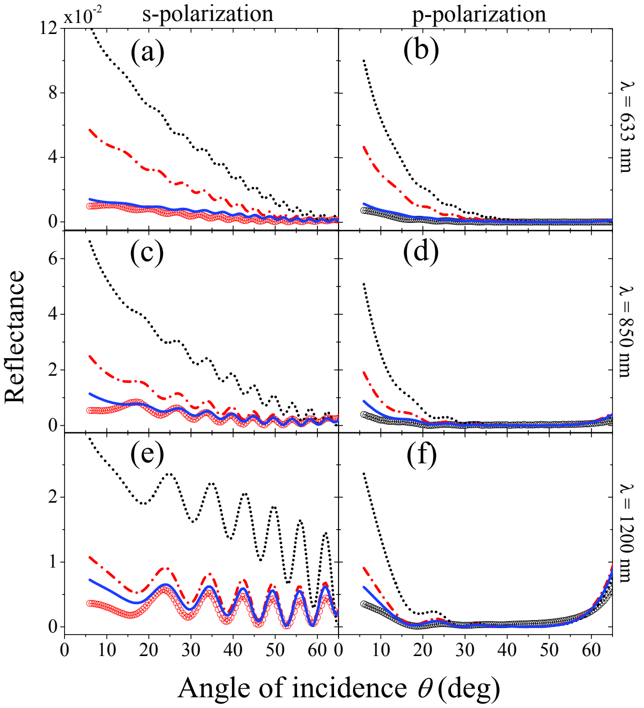

Figure 7.7: Measured and calculated specular reflectance of s- [(a), (c) and (e)] and p-polarized light [(b), (d) and (f)] as a function of the angle of incidence for three wavelengths: (a and b) λ = 633 nm, (c and d) λ = 850 nm, and (e and f) λ = 1200 nm. The measurements are displayed with circles. The dotted lines represent the reflectance calculated for vertical nanowires, the dash-dotted lines show the calculation including nonvertical nanowires, and the solid lines represent the reflectance corrected for the surface scattering according to Eq. 7.8, with a root mean square of the roughness feature height of σ = 60 nm.

The calculated effective refractive index can be used to compute the specular reflectance of the coherent beam in the nanowire layer by applying the transfer matrix method. Three layers are considered for these calculations, namely, a semi-infinite layer of air (n_{air} = 1), from which the light is incident, an effective medium for the coherent beam with a thickness of 7.3 μm describing the layer of nanowires; and a semi-infinite substrate of silicon. In Fig. 7.7 we display the specular reflectance measurements at three different wavelengths: λ = 633, 850 and 1200 nm, and for s- (left column) and p-polarization (right column) together with the transfer matrix calculations.

The measurements are represented by the symbols (red circles for s-polarization and black circles for p-polarization), whereas the calculations are illustrated with the solid lines. If only the vertical nanowires are considered, the calculated specular reflectance (black dotted lines) is significantly higher than the measurement, though there is a qualitative agreement in the Fabry-Perót oscillations. The addition of the isotropic extinction caused by the randomly oriented nonvertical nanowires provides a much better quantitative agreement between the calculated (red dash-dotted lines) and the measured reflectance. In addition, we can correct the calculations to take into account the extinction due to surface roughness scattering by using the Eq. 7.8. The root mean square feature height, σ used to fit the measurements for all the wavelengths and polarizations is 60 nm. This value is reasonable to effectively take into account surface irregularities of the bottom and upper interface of the nanowire layer. Note that the possible light extinction by the gold particles on top of each nanowire is included into the surface roughness scattering. Therefore, the value of σ might overestimate the surface roughness of the sample. As can be appreciated in Fig. 7.7, the correction to the specular reflection introduced by the nonvertical nanowires and the surface roughness results in an excellent agreement between the calculation (blue solid lines) and the measurements.

The Mie scattering effective medium theory presented in this chapter is general and valid for any wavelength and angle of incidence. Figure 7.8 shows the specular reflectance measured as a function of the wavelength and the angle of incidence for s- and p-polarized light ((a) and (b), respectively) compared to the specular reflectance calculated with the effective medium formalism for the respective light polarizations ((c) and (d)). The color scale is kept constant in all plots underlining the good agreement between the experiment and the theory.

To illustrate the extinction anisotropy of an ensemble of vertical nanowires, we have derived the extinction lengths for s- and p-polarized light obtained from the measurements of the extinction coefficient by knowing that $l_{ext} = \frac{\lambda}{4\pi k_{\mathrm{eff}}}$. Figure 7.9 shows the ratio of extinction lengths, $\frac{l^{\mathrm{s}}_{ext}}{l^{\mathrm{p}}_{ext}}$. We present this ratio for the three different wavelengths, that is, $\lambda = 633$ nm (solid line), $\lambda = 850$ nm, (dashed line) and $\lambda = 1200$ nm (dotted line) as a function of the angle of incidence. As expected, the anisotropy vanishes for normally incident light.

Because of the strong polarization dependence of the light scattering and absorption by nanowires [78], the layer consisting of vertical nanowires shows large extinction anisotropy for larger angles of incident light. These measurements represent the first demonstration of anisotropic scattering and absorption in random ensembles of semiconductor nanowires. For the wavelengths in the absorbing range of silicon, such as $\lambda = 633$ nm, the extinction length of s-polarized light can be nearly twice as long as that for p-polarized light in our sample. The ratio of extinction lengths in the near-infrared regime is even larger achieving the value of 3.5 for $\lambda = 1200$ nm and at large angles of incidence. For this wavelength the extinction is solely due to scattering.

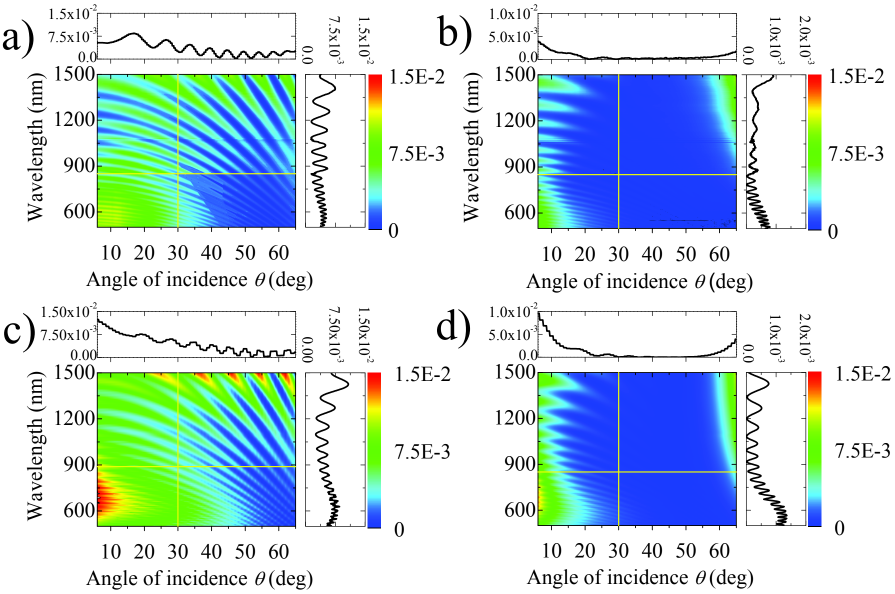

Figure 7.8: Measured specular reflectance as a function of the wavelength and angle of incidence for (a) s-polarized and (b) p-polarized light, the same as in Fig. 7.4. (c) and (d) show the specular reflectance calculated using the Mie-scattering effective medium formalism as a function of the wavelength and the angle of incidence for s- and p-polarized light, respectively. The calculations include the effect of nonvertical nanowires and surface roughness of $\sigma = 60$ nm. The graphs on the top and right sides of each figure are the specular reflectance at $\lambda = 850$ nm and 30°, respectively.

7.5 Conclusions

Layers of nanowires form a medium with an effective complex refractive index that characterizes the propagation and extinction of the coherent beam or the beam propagating in the forward direction. We have derived the polarization-, angle of incidence- and wavelength-dependent refraction and extinction of the coherent beam in the ensembles of polydisperse silicon nanowires from the properties of individual infinite cylinders in the independent scattering approximation. Due to the low effective refractive index of the nanowire layer, the incident light can be easily transmitted into the nanowire layer where it is extinct by scattering and absorption. Our measurements reveal a strongly anisotropic scattering and absorption in the nanowire layer. The description of light propagation and extinction in nanowire layers is of relevance for the design of novel nanowire solar cells in which scattering and absorption need to be optimized.

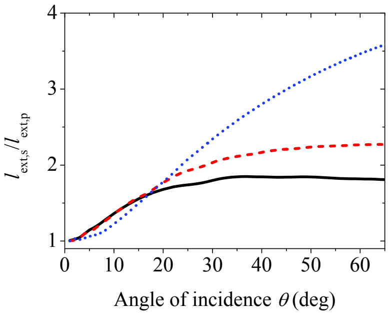

Figure 7.9: Extinction anisotropy of a polydisperse ensemble of vertical nanowires represented as the ratio of the extinction lengths for s- and p-polarized light as a function of the angle of incidence. The extinction anisotropy is plotted for $\lambda = 633$ nm (solid line), $\lambda = 850$ nm (dashed line), and $\lambda = 1200$ nm (dotted line).

APPENDIX A

FINITE ELEMENT OPTICAL SIMULATIONS

Finite-element-method-based numerical simulations in Chapter 4 were performed using commercial software COMSOL Multiphysics v4.2. The simulated space consisted of a circular cylinder of length l and diameter d, representing the nanowire, two concentric spheres of radii $0.7l$ and $0.9l$, respectively, with their centers coinciding with the one of the cylinder and a plane perpendicular to its axis, passing through one of the ends, and splitting the spherical domain and the outer shell into two subdomains. That part of the spherical domain in which the cylinder is located was set to be air, while the other part, simulating the substrate, and the cylinder were set to be InP, with material constants taken from Palik's book. [167] Both parts of the outer shell were defined as perfectly matched layers (PML) to absorb all the outgoing radiation, each one with the same index as the adjacent domain to avoid unphysical reflections. The meshing was done with the program built-in algorithm, which creates a tetrahedral mesh. The mesh maximum element size (MES), which limits the maximum size of the edges of the tetrahedrons, was set to be 20 nm in the domain representing the wire, 60 nm in the one representing the substrate, and 80 nm for the elements separating the air and the PML. All the rest of the meshing was set to have a MES of 120 nm. The maximum element growth rate was set to 1.3 in the wire domain, and 1.35 in all remaining domains. Direct PARDISO solver was used to solve the problem. [180, 181] The package PARDISO is a software for solving large sparse symmetric and unsymmetric linear systems of equations based on fast factorization pivoting methods, that is included within COMSOL Multiphysics. Simulations were highly memory demanding (typically more than 150 GB) and took about one hour per wavelength simulation on a 22 CPUs computing station.

APPENDIX B

TRANSFER MATRIX METHOD

A transfer-matrix method for isotropic layered media is used for modeling the reflectance and transmittance of planar structures. [177] We use this technique in Chapter 7 to calculate the reflectance of an effective medium formed by size-dispersed nanowires supported on a thick wafer.

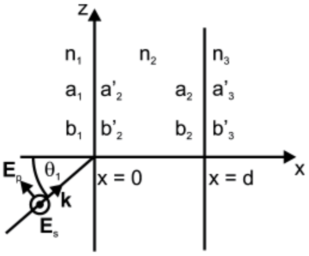

Figure B.1: A three layer system consisting of three materials with refractive indices n_1, n_2, and n_3, respectively. The field amplitudes at the interfaces are given by a_1, a'_2, a_2, a'_3, for the right traveling waves and b_1, b'_2, b_2, b'_3 for the left traveling wave. The incident light beam with the wavevector **k** and the angle of incidence θ_1 is defined in medium 1.

Let us consider a three layer system as the one in Figure B.1. The electric field of an electromagnetic plane wave of angular frequency ω propagating with the z-component of the wave vector k_z in the xz plane is given by

$$\mathbf{E} = \mathbf{E}(x)\mathrm{e}^{\mathrm{i}(\omega \mathrm{t} - \mathrm{k_z z})}. \tag{B.1}$$

For a detailed derivation of each component of the field see Ref. [118]. We assume that the light is linearly polarized, either $s-$polarized, i.e., $\mathbf{E} \parallel \mathrm{y}$ or $E_x = E_z = 0$, or $p-$polarized, i.e., $\mathbf{H} \parallel \mathbf{y}$ or $E_y = 0$. If we assume that light is only incident on the three layer system from medium 1, the electric field in layer 1 and 2 consists of a right- and left-traveling wave and can be written as

$$E(x) = a\mathrm{e}^{-ik_\mathrm{x}\mathrm{x}} + b\mathrm{e}^{ik_\mathrm{x}\mathrm{x}} \equiv a(\mathrm{x}) + b(\mathrm{x}), \tag{B.2}$$

where $\pm k_\mathrm{x}$ are the x-components of the wave vector given by $k_\mathrm{x} = n_\alpha \frac{2\pi}{\lambda} \cos\theta'_\alpha$ in medium α with refractive index n_α and angle inside the medium θ'_α. The amplitudes a and b are constant in each homogeneous layer. The amplitude of the wave traveling to the right is represented by $a(\mathrm{x})$, while the left traveling component is described by $b(\mathrm{x})$. We define the various amplitudes at the interfaces between the different media as

$$\begin{aligned}
a_1 &= a(0^-),\\
b_1 &= b(0^-),\\
a'_2 &= a(0^+),\\
b'_2 &= b(0^+),\\
a_2 &= a(d^-),\\
b_2 &= b(d^-),\\
a'_3 &= a(d^+),\\
b'_3 &= b(d^+) = 0,
\end{aligned} \tag{B.3}$$

where 0^- represents the left side and 0^+ the right side of the interface at $\mathrm{x} = 0$. Similarly, d^- and d^+ represent the left and right side of the interface at $\mathrm{x} = d$ (see Fig. B.1). If we represent the left and right traveling components of the electric field as column vectors, the vectors at each side of the interface are related by

$$\begin{pmatrix} a_1 \\ b_1 \end{pmatrix} = \mathbf{D}_{1,2} \begin{pmatrix} a'_2 \\ b'_2 \end{pmatrix}, \tag{B.4}$$

$$\begin{pmatrix} a'_2 \\ b'_2 \end{pmatrix} = \mathbf{P}_2 \begin{pmatrix} a_2 \\ b_2 \end{pmatrix}, \tag{B.5}$$

$$\begin{pmatrix} a_2 \\ b_2 \end{pmatrix} = \mathbf{D}_{2,3} \begin{pmatrix} a'_3 \\ b'_3 \end{pmatrix} \tag{B.6}$$

where $\mathbf{D}_{1,2}$, and $\mathbf{D}_{2,3}$ are the so-called transmission matrices and $\mathbf{P}_2$ the propagation matrices that accounts for the propagation in the layer. The matrices are defined for layer α as follows:

$$\mathbf{D}_{\alpha,\alpha+1} = \frac{1}{t_{\alpha,\alpha+1}} \begin{pmatrix} 1 & r_{\alpha,\alpha+1} \\ r_{\alpha,\alpha+1} & 1 \end{pmatrix} \tag{B.7}$$

and

$$\mathbf{P}_\alpha = \begin{pmatrix} \mathrm{e}^{\mathrm{i}\phi_\alpha} & 0 \\ 0 & \mathrm{e}^{-\mathrm{i}\phi_\alpha} \end{pmatrix}, \tag{B.8}$$

where $t_{\alpha,\alpha+1}$ and $r_{\alpha,\alpha+1}$ are the Fresnel amplitude reflection and transmission coefficients for the interface and $\phi_\alpha = \frac{2\pi}{\lambda} n_\alpha \cos\theta'_\alpha L$ is the phase change of light traveling through

the layer, with L the thickness of the layer, λ the vacuum wavelength, and n_α and θ'_α the refractive index of the layer and the angle inside the layer, respectively.
From Equations (B.4)-(B.6), the amplitudes a_1, b_1, and a'_3 and b'_3 are related by the multiplication of the transmission matrix and the propagation matrix

$$\begin{aligned}\begin{pmatrix} a_1 \\ b_1 \end{pmatrix} &= \mathbf{D}_{1,2}\mathbf{P}_2\mathbf{D}_{2,3}\begin{pmatrix} a'_3 \\ b'_3 \end{pmatrix} \\ &= \begin{pmatrix} M_{11} & M_{12} \\ M_{21} & M_{22} \end{pmatrix}\begin{pmatrix} a'_3 \\ b'_3 \end{pmatrix} \\ &= \mathbf{M}\begin{pmatrix} a'_3 \\ b'_3 \end{pmatrix}.\end{aligned} \tag{B.9}$$

The multiplication of the matrices can be represented by the matrix **M** consisting of the four elements M_{11}, M_{12}, M_{21}, and M_{22}.
The reflection and transmission of a plane wave through the three layer structure for light coming from layer 1 are defined as

$$r = \left(\frac{b_1}{a_1}\right)_{b'_3=0} \tag{B.10}$$

and

$$t = \left(\frac{a'_3}{a_1}\right)_{b'_3=0}, \tag{B.11}$$

respectively. Using Equation (B.9), the amplitude reflection and transmission coefficients of the layered system are given by

$$r = \frac{M_{21}}{M_{11}} \tag{B.12}$$

and

$$t = \frac{1}{M_{11}}. \tag{B.13}$$

The reflectance R for the case that the medium of layer 1 is lossless is defined as

$$R = |r|^2 = \left|\frac{M_{21}}{M_{11}}\right|^2. \tag{B.14}$$

If the bounding layers, 1 and 3, are both dielectrics, with real n_1 and n_3, the transmission T for a wave incident with an angle θ_1 is given by

$$T = \frac{n_3\cos\theta'_3}{n_1\cos\theta_1}|t|^2 = \frac{n_3\cos\theta'_3}{n_1\cos\theta_1}\left|\frac{1}{M_{11}}\right|^2, \tag{B.15}$$

with θ'_3 the angle the light forms with the x axis in the third layer related to θ_1 by Snell's law.

The transfer-matrix method explained above is not limited for three-layer systems. This formalism can be easily expanded for multi-layer structures by multiplying the transmission and propagation matrices for each layer. For any layer it is possible to input the refractive index as a function of wavelength, angle of incidence and polarization.

REFERENCES

[1] R. S. Wagner and W. C. Ellis, *Vapor-liquid-solid mechanism of single crystal growth,* Appl. Phys. Lett. **4**, 89 (1964).

[2] C. M. Lieber and Z. L. Wang, *Functional nanowires,* MRS Bulletin **32**, 99 (2007).

[3] V. Schmidt, J. V. Wittemann, S. Senz, and U. Gösele, *Silicon nanowires: a review on aspects of their growth and their electrical properties,* Adv. Mater. **21**, 2681 (2009).

[4] A. M. Morales and C. M. Lieber, *A laser ablation method for the synthesis of crystalline semiconductor nanowires,* Science **279**, 208 (1998).

[5] G. Gu, M. Burghard, G. T. Kim, G. S. Dusberg, P. W. Chiu, V. Krstic, S. Roth, and W. Q. Han, *Growth and electrical transport of germanium nanowires,* J. Appl. Phys. **90**, 5747 (2001).

[6] M. H. Huang, S. Mao, H. Feick, H. Yan, Y. Wu, H. Kind, E. Weber, R. Russo, and P. Yang, *Room-temperature ultraviolet nanowire nanolasers,* Science **292**, 1897 (2001).

[7] X. Duan, Y. Huang, R. Agarwal, and C. M. Lieber, *Single-nanowire electrically driven lasers,* Nature **421**, 241 (2003).

[8] J. C. Johnson, H. Yan, P. Yang, and R. J. Saykally, *Optical cavity effects in ZnO nanowire lasers and waveguides,* J. Phys. Chem. B **107**, 8816 (2003).

[9] J. Zhang, A. A. Lutich, A. S. Susha, A. L. Rogach, F. Jäckel, and J. Feldmann, *Single-mode waveguiding in bundles of self-assembled semiconductor nanowires,* Appl. Phys. Lett. **97**, 221915 (2010).

[10] X. Duan, Y. Huang, Y. Cui, J. Wang, and C. M. Lieber, *Indium phosphide nanowires as building blocks for nanoscale electronic and optoelectronic devices,* Nature **409**, 66 (2001).

[11] M. S. Gudiksen, L. J. Lauhon, J. Wang, D. C. Smith, and C. M. Lieber, *Growth of nanowire superlattice structures for nanoscale photonics and electronics,* Nature **415**, 617 (2002).

[12] M. T. Björk, B. J. Ohlsson, T. Sass, A. I. Persson, C. Thelander, M. H. Magnusson, K. Deppert, L. R. Wallenberg, and L. Samuelson, *One-dimensional steeplechase for electrons realized,* Nano Lett. **2**, 87 (2002).

[13] E. P. A. M. Bakkers, J. A. van Dam, S. De Franceschi, L. P. Kouwenhoven, M. Kaiser, M. Verheijen, H. Wondergem, and P. van der Sluis, *Epitaxial growth of InP nanowires on germanium,* Nature Mater. **3**, 769 (2004).

[14] V. Khorenko, I. Regolin, S. Neumann, W. Prost, F.-J. Tegude, and H. Wiggers, *Photoluminescence of GaAs nanowhiskers grown on Si substrate,* Appl. Phys. Lett. **85**, 6407 (2004).

[15] T. Mårtensson, C. P. T. Svensson, B. A. Wacaser, M. W. Larsson, W. Seifert, K. Deppert, A. Gustafsson, L. R. Wallenberg, and L. Samuelson, *Epitaxial III-V nanowires on silicon,* Nano Lett. **4**, 1987 (2004).

[16] L. K. van Vugt, S. Rühle, and D. Vanmaekelbergh, *Phase-correlated nondirectional laser emission from the end facets of a ZnO nanowire,* Nano Lett. **6**, 2707 (2006).

[17] F. Qian, Y. Li, S. Gradečak, H. G. Park, Y. Dong, Y. Ding, Z. L. Wang, and C. M. Lieber, *Multi-quantum-well nanowire heterostructures for wavelength-controlled lasers,* Nature Mater. **7**, 701 (2008).

[18] S. L. Diedenhofen, O. T. A. Janssen, M. Hocevar, A. Pierret, E. P. A. M. Bakkers, H. P. Urbach, and J. Gómez Rivas, *Controlling the Directional Emission of Light by Periodic Arrays of Heterostructured Semiconductor Nanowires,* ACS Nano **5**, 5830 (2011).

[19] Y. Fontana, G. Grzela, E. P. A. M. Bakkers, and J. Gómez Rivas, *Mapping the directional emission of quasi-two-dimensional photonic crystals of semiconductor nanowires using Fourier microscopy,* Phys. Rev. B **86**, 245303 (2012).

[20] A. C. Scofield, S.-H. Kim, J. N. Shapiro, A. Lin, B. Liang, A. Scherer, and D. L. Huffaker, *Bottom-up Photonic Crystal Lasers,* Nano Lett. **11**, 5387 (2011).

[21] N. Panev, A. I. Persson, N. Sköld, and L. Samuelson, *Sharp exciton emission from single InAs quantum dots in GaAs nanowires,* Appl. Phys. Lett. **83**, 2238 (2003).

[22] M. T. Borgström, V. Zwiller, E. Müller, and A. Imamoglu, *Optically bright quantum dots in single nanowires,* Nano Lett. **5**, 1439 (2005).

[23] I. Friedler, C. Sauvan, J. P. Hugonin, P. Lalanne, J. Claudon, and J.-M. Gérard, *Solid-state single photon sources: the nanowire antenna,* Opt. Express **17**, 2095 (2009).

[24] J. Claudon, J. Bleuse, N. S. Malik, M. Bazin, P. Jaffrennou, N. Gregersen, C. Sauvan, P. Lalanne, and J.-M. Gérard, *A highly efficient single-photon source based on a quantum dot in a photonic nanowire,* Nature Photon. **4**, 174 (2010).

[25] J. Bleuse, J. Claudon, M. Creasey, N. S. Malik, J.-M. Gérard, I. Maksymov, J. P. Hugonin, and P. Lalanne, *Inhibition, enhancement, and control of spontaneous emission in photonic nanowires,* Phys. Rev. Lett. **106**, 103601 (2011).

[26] M. Munsch, J. Claudon, J. Bleuse, N. S. Malik, E. Dupuy, J.-M. Gérard, Y. Chen, N. Gregersen, and J. Mørk, *Linearly Polarized, Single-Mode Spontaneous Emission in a Photonic Nanowire,* Phys. Rev. Lett. **108**, 77405 (2012).

[27] M. E. Reimer, G. Bulgarini, N. Akopian, M. Hocevar, M. B. Bavinck, M. A. Verheijen, E. P. A. M. Bakkers, L. P. Kouwenhoven, and V. Zwiller, *Bright single-photon sources in bottom-up tailored nanowires,* Nat. Commun. **3**, 737 (2012).

[28] D. Dalacu, K. Mnaymneh, J. Lapointe, X. Wu, P. J. Poole, G. Bulgarini, V. Zwiller, and M. Reimer, *Ultra-clean emission from InAsP quantum dots in defect-free wurtzite InP nanowires,* Nano Lett. **12**, 5919 (2012).

[29] S. Deshpande, J. Heo, A. Das, and P. Bhattacharya, *Electrically driven polarized single-photon emission from an InGaN quantum dot in a GaN nanowire,* Nature Commun. **4**, 1675 (2013).

[30] B. Tian, X. Zheng, T. J. Kempa, Y. Fang, N. Yu, G. Yu, J. Huang, and C. M. Lieber, *Coaxial silicon nanowires as solar cells and nanoelectronic power sources,* Nature **449**, 885 (2007).

[31] L. Tsakalakos, J. Balch, J. Fronheiser, B. A. Korevaar, O. Sulima, and J. Rand, *Silicon nanowire solar cells,* Appl. Phys. Lett. **91**, 233117 (2007).

[32] M. D. Kelzenberg, D. B. Turner-Evans, B. M. Kayes, A. Michael, M. C. Putnam, N. S. Lewis, and H. A. Atwater, *Photovoltaic measurements in single-nanowire silicon solar cells,* Nano Lett. **8**, 710 (2008).

[33] T. Stelzner, M. Pietsch, G. Andrä, F. Falk, E. Ose, and S. Christiansen, *Silicon nanowire-based solar cells,* Nanotechnology **19**, 295203 (2008).

[34] H. Goto, K. Nosaki, K. Tomioka, S. Hara, K. Hiruma, J. Motohisa, and T. Fukui, *Growth of Core–Shell InP Nanowires for Photovoltaic Application by Selective-Area Metal Organic Vapor Phase Epitaxy,* Appl. Phys. Express **2**, 5004 (2009).

[35] W. U. Huynh, J. J. Dittmer, and A. P. Alivisatos, *Hybrid nanorod-polymer solar cells,* Science **295**, 2425 (2002).

[36] J. B. Baxter and E. S. Aydil, *Nanowire-based dye-sensitized solar cells,* Appl. Phys. Lett. **86**, 053114 (2005).

[37] J. Wang, M. S. Gudiksen, X. Duan, Y. Cui, and C. M. Lieber, *Highly polarized photoluminescence and photodetection from single indium phosphide nanowires,* Science **293**, 1455 (2001).

[38] M. H. M. van Weert, N. Akopian, F. Kelkensberg, U. Perinetti, M. P. van Kouwen, J. Gómez Rivas, M. T. Borgström, R. E. Algra, M. A. Verheijen, and E. P. A. M. Bakkers, *Orientation-Dependent Optical-Polarization Properties of Single Quantum Dots in Nanowires,* Small **5**, 2134 (2009).

[39] L. Cao, J. S. White, J. S. Park, J. A. Schuller, B. M. Clemens, and M. L. Brongersma, *Engineering light absorption in semiconductor nanowire devices,* Nature Mater. **8**, 643 (2009).

[40] L. Cao, P. Fan, A. P. Vasudev, J. S. White, Z. Yu, W. Cai, J. A. Schuller, S. Fan, and M. L. Brongersma, *Semiconductor nanowire optical antenna solar absorbers,* Nano Lett. **10**, 439 (2010).

[41] G. Brönstrup, N. Jahr, C. Leiterer, A. Csáki, W. Fritzsche, and S. Christiansen, *Optical Properties of Individual Silicon Nanowires for Photonic Devices,* ACS Nano **4**, 7113 (2010).

[42] Z. Fan, R. Kapadia, P. W. Leu, X. Zhang, Y.-L. Chueh, K. Takei, K. Yu, A. Jamshidi, A. A. Rathore, D. J. M. W. Ruebusch, and A. Javey, *Ordered arrays of dual-diameter nanopillars for maximized optical absorption,* Nano Lett. **10**, 3823 (2010).

[43] S. L. Diedenhofen, O. T. A. Janssen, G. Grzela, E. P. A. M. Bakkers, and J. Gómez Rivas, *Strong Geometrical Dependence of the Absorption of Light in Arrays of Semiconductor Nanowires,* ACS Nano **5**, 2316 (2011).

[44] K. Seo, M. Wober, P. Steinvurzel, E. Schonbrun, Y. Dan, T. Ellenbogen, and K. B. Crozier, *Multicolored Vertical Silicon Nanowires,* Nano Lett. **11**, 1851 (2011).

[45] P. M. Wu, N. Anttu, H. Q. Xu, L. Samuelson, and M.-E. Pistol, *Colorful InAs Nanowire Arrays: From Strong to Weak Absorption with Geometrical Tuning,* Nano Lett. **12**, 1990 (2012).

[46] N. Anttu, K. L. Namazi, P. M. Wu, P. Yang, H. Xu, H. Q. Xu, and U. Håkanson, *Drastically increased absorption in vertical semiconductor nanowire arrays: A non-absorbing dielectric shell makes the difference,* Nano Res. **5**, 863 (2012).

[47] N. Anttu, *Geometrical optics, electrostatics, and nanophotonic resonances in absorbing nanowire arrays,* Opt. Lett. **38**, 730 (2013).

[48] J. Wallentin, N. Anttu, D. Asoli, M. Huffman, I. Åberg, M. H. Magnusson, G. Siefer, P. Fuss-Kailuweit, F. Dimroth, B. Witzigmann, H. Q. Xu, L. Samuelson, K. Deppert, and M. T. Borgström, *InP Nanowire Array Solar Cells Achieving* 13.8% *Efficiency by Exceeding the Ray Optics Limit,* Science **339**, 1057 (2013).

[49] C. J. Keavney, V. E. Haven, and S. M. Vernon, *Emitter structures in MOCVD InP solar cells,* in *IEEE Conference Record of the Twenty First Photovoltaic Specialists,* pages 141–144, 1990.

[50] M. A. Green, K. Emery, Y. Hishikawa, W. Warta, and E. D. Dunlop, *Solar cell efficiency tables (version 41)*, Prog. Photovolt: Res. Appl. **21**, 1 (2013).

[51] T. J. Kempa, B. Tian, D. R. Kim, J. Hu, X. Zheng, and C. M. Lieber, *Single and tandem axial pin nanowire photovoltaic devices*, Nano Lett. **8**, 3456 (2008).

[52] E. Garnett and P. Yang, *Light trapping in silicon nanowire solar cells*, Nano Lett. **10**, 1082 (2010).

[53] M. Heurlin, P. Wickert, S. Fält, M. T. Borgström, K. Deppert, L. Samuelson, and M. H. Magnusson, *Axial InP nanowire tandem junction grown on a silicon substrate*, Nano Lett. **11**, 2028 (2011).

[54] S.-D. Suk, K. H. Yeo, K. H. Cho, M. Li, Y. young Yeoh, S.-Y. Lee, S.-M. Kim, E. J. Yoon, M. S. Kim, C.-W. Oh, S.-H. Kim, D.-W. Kim, and D. Park, *High-performance twin silicon nanowire MOSFET (TSNWFET) on bulk Si wafer*, IEEE Trans. Nanotechnol. **7**, 181 (2008).

[55] N. Singh, K. D. Buddharaju, S. Manhas, A. Agarwal, S. C. Rustagi, G. Lo, N. Balasubramanian, and D.-L. Kwong, *Si, SiGe nanowire devices by top–down technology and their applications*, IEEE Trans. Electron. Dev. **55**, 3107 (2008).

[56] H. I. Lui, P. K. Biegelsen, N. M. Johnson, F. A. Ponce, and R. F. W. Pease, *Self-Limiting Oxidation of Si Nanowires*, J. Vac. Sci. Technol. B **11**, 2532 (1993).

[57] C.-M. Hsu, S. T. Connor, M. X. Tang, and Y. Cui, *Wafer-scale silicon nanopillars and nanocones by Langmuir–Blodgett assembly and etching*, Appl. Phys. Lett. **93**, 133109 (2008).

[58] K. J. Morton, G. Nieberg, S. Bai, and S. Y. Chou, *Wafer-scale patterning of sub-40 nm diameter and high aspect ratio (> 50: 1) silicon pillar arrays by nanoimprint and etching*, Nanotechnology **19**, 345301 (2008).

[59] H. J. Fan, P. Werner, and M. Zacharias, *Semiconductor Nanowires: From Self-Organization to Patterned Growth*, Small **2**, 700 (2006).

[60] P. Nguyen, H. T. Ng, and M. Meyyappan, *Catalyst metal selection for synthesis of inorganic nanowires*, Adv. Mater. **17**, 1773 (2005).

[61] M. Mattila, T. Hakkarainen, H. Lipsanen, H. Jiang, and E. I. Kauppinen, *Catalyst-free growth of In (As) P nanowires on silicon*, Appl. Phys. Lett. **89**, 063119 (2006).

[62] B. Mandl, J. Stangl, T. Mårtensson, A. Mikkelsen, J. Eriksson, L. S. Karlsson, G. Bauer, L. Samuelson, and W. Seifert, *Au-free epitaxial growth of InAs nanowires*, Nano Lett. **6**, 1817 (2006).

[63] T. Mårtensson, J. B. Wagner, E. Hilner, A. Mikkelsen, C. Thelander, J. Stangl, B. J. Ohlsson, A. Gustafsson, E. Lundgren, L. Samuelson, and W. Seifert, *Epitaxial Growth of Indium Arsenide Nanowires on Silicon Using Nucleation Templates Formed by Self-Assembled Organic Coatings*, Adv. Mater. **19**, 1801 (2007).

[64] K. Tomioka, P. Mohan, J. Noborisaka, S. Hara, J. Motohisa, and T. Fukui, *Growth of highly uniform InAs nanowire arrays by selective-area MOVPE,* J. Cryst. Growth **298**, 644 (2007).

[65] C. Colombo, D. Spirkoska, M. Frimmer, G. Abstreiter, and A. Fontcuberta i Morral, *Ga-assisted catalyst-free growth mechanism of GaAs nanowires by molecular beam epitaxy,* Phys. Rev. B **77**, 155326 (2008).

[66] A. Pierret, M. Hocevar, S. L. Diedenhofen, R. E. Algra, E. Vlieg, E. C. Timmering, M. A. Verschuuren, G. W. G. Immink, M. A. Verheijen, and E. P. A. M. Bakkers, *Generic nano-imprint process for fabrication of nanowire arrays,* Nanotechnology **21**, 065305 (2010).

[67] M. Mattila, T. Hakkarainen, H. Lipsanen, H. Jiang, and E. I. Kauppinen, *Crystal-structure-dependent photoluminescence from InP nanowires,* Nanotechnology **17**, 1580 (2006).

[68] F. Glas, J. C. Harmand, and G. Patriarche, *Why does wurtzite form in nanowires of III-V zinc blende semiconductors?,* Phys. Rev. Lett. **99**, 146101 (2007).

[69] U. Krishnamachari, M. Borgström, B. J. Ohlsson, N. Panev, L. Samuelson, W. Seifert, M. W. Larsson, and L. R. Wallenberg, *Defect-free InP nanowires grown in [001] direction on InP (001),* Appl. Phys. Lett. **85**, 2077 (2004).

[70] J. Wang, S. Plissard, M. Hocevar, T. T. T. Vu, T. Zehender, G. G. W. Immink, M. A. Verheijen, J. Haverkort, and E. P. A. M. Bakkers, *Position-controlled [100] InP nanowire arrays,* Appl. Phys. Lett. **100**, 053107 (2012).

[71] R. Gupta, Q. Xiong, G. D. Mahan, and P. C. Eklund, *Surface optical phonons in gallium phosphide nanowires,* Nano Lett. **3**, 1745 (2003).

[72] O. L. Muskens, S. L. Diedenhofen, M. H. M. van Weert, M. T. Borgström, E. P. A. M. Bakkers, and J. Gómez Rivas, *Epitaxial growth of aligned semiconductor nanowire metamaterials for photonic applications,* Adv. Func. Mat. **18**, 1039 (2008).

[73] O. L. Muskens, J. Gómez Rivas, R. E. Algra, E. P. Bakkers, and A. Lagendijk, *Design of light scattering in nanowire materials for photovoltaic applications,* Nano Lett. **8**, 2638 (2008).

[74] T. Mårtensson, M. Borgström, W. Seifert, B. Ohlsson, and L. Samuelson, *Fabrication of individually seeded nanowire arrays by vapourliquidsolid growth,* Nanotechnology **14**, 1255 (2003).

[75] T. Mårtensson, P. Carlberg, Borgströagnus, L. Montelius, W. Seifert, and L. Samuelson, *Nanowire Arrays Defined by Nanoimprint Lithography,* Nano Lett. **4**, 699 (2004).

[76] M. A. Verschuuren, *PhD Thesis: Substrate conformal imprint lithography for nanophotonics,* Utrecht University (NL), 2010.

[77] C. F. Bohren and D. R. Huffman, *Absorption and scattering of light by small particles,* Wiley, New York, 1983.

[78] L. Cao, P. Fan, E. S. Barnard, A. M. Brown, and M. L. Brongersma, *Tuning the color of silicon nanostructures,* Nano Lett. **10**, 2649 (2010).

[79] J. C. Johnson, H. Yan, R. D. Schaller, L. H. Haber, R. J. Saykally, and P. Yang, *Single nanowire lasers,* J. Phys. Chem. B **105**, 11387 (2001).

[80] A. V. Maslov and C. Z. Ning, *Far-field emission of a semiconductor nanowire laser,* Opt. Lett. **29**, 572 (2004).

[81] J. Kupec and B. Witzigmann, *Dispersion, wave propagation and efficiency analysis of nanowire solar cells,* Opt. Express **17**, 10399 (2009).

[82] G. Grzela, R. Paniagua-Domínguez, T. Barten, Y. Fontana, J. A. Sánchez-Gil, and J. Gómez Rivas, *Nanowire Antenna Emission,* Nano Lett. **12**, 5481 (2012).

[83] B. Wang and P. W. Leu, *Tunable and selective resonant absorption in vertical nanowires,* Opt. Lett. **37**, 3756 (2012).

[84] J. A. Stratton, *Electromagnetic Theory. International Series in Pure and Applied Physics,* McGraw-Hill Book Company, New York, 1941.

[85] H. C. van de Hulst, *Light Scattering by small particles,* Dover Publications, Inc., New York, 1981.

[86] A. García-Etxarri, R. Gómez-Medina, L. S. Froufe-Pérez, C. López, L. Chantada, F. Scheffold, J. Aizpurua, M. Nieto-Vesperinas, and J. J. Sáenz, *Strong magnetic response of submicron silicon particles in the infrared,* Opt. Express **19**, 4815 (2011).

[87] R. Gómez-Medina, B. García-Cámara, I. Suárez-Lacalle, F. González, F. Moreno, M. Nieto-Vesperinas, and J. J. Sáenz, *Electric and magnetic dipolar response of germanium nanospheres: interference effects, scattering anisotropy, and optical forces,* J. Nanophotonics **5**, 053512 (2011).

[88] H. Kallel, A. Arbouet, G. BenAssayag, A. Chehaidar, A. Potié, B. Salem, T. Baron, and V. Paillard, *Tunable enhancement of light absorption and scattering in $Si_{1-x}Ge_x$ nanowires,* Phys. Rev. B **86**, 085318 (2012).

[89] J. Zhang, A. A. Lutich, J. Rodríguez-Fernández, A. S. Susha, A. L. Rogach, F. Jäckel, and J. Feldmann, *Optical anisotropy of semiconductor nanowires beyond the electrostatic limit,* Phys. Rev. B **82**, 155301 (2010).

[90] E. Snitzer, *Cylindrical dielectric waveguide modes,* J. Opt. Soc. Am. **51**, 491 (1961).

[91] J. Bures, *Guided optics,* Wiley-VCH, 2009.

[92] H. Jäckel, *Optoelectronics and Optical Communication, Lecture notes,* http://people.ee.ethz.ch/~fyuriy/oe/oe_optcom_chapters/Optoelectronics_-2007_Appendix03-germ.pdf, 2010.

[93] C. S. Lee, S. W. Lee, and S. L. Chuang, *Plot of modal field distribution in rectangular and circular waveguides,* IEEE Trans. Microw. Theory Tech. **33**, 271 (1985).

[94] C. A. Balanis, *Circular waveguides,* Int. J. Electron. **1996**, 551 (1996).

[95] A. N. Oraevsky, *Whispering-gallery waves,* Quantum Electron. **32**, 377 (2002).

[96] B. J. W. S. Rayleigh, *The theory of sound,* volume 2, Macmillan, 1896.

[97] J. Arnbak, *Leaky waves on a dielectric rod,* Electron. Lett. **5**, 41 (1969).

[98] R. Sammut and A. W. Snyder, *Leaky modes on circular optical waveguides,* Appl. Opt. **15**, 477 (1976).

[99] A. Alù, F. Bilotti, N. Engheta, and L. Vegni, *Theory and simulations of a conformal omni-directional subwavelength metamaterial leaky-wave antenna,* IEEE Trans. Antenn. Propag. **55**, 1698 (2007).

[100] C. Lam, P. T. Leung, and K. Young, *Explicit asymptotic formulas for the positions, widths, and strengths of resonances in Mie scattering,* J. Opt. Soc. Am. B **9**, 1585 (1992).

[101] S.-s. Yi, *Observation of the scattered TE-and TM-mode coupling in active dielectric cylinder,* Opt. Commun. **173**, 211 (2000).

[102] W. F. Liu, J. I. Oh, and W. Z. Shen, *Light trapping in single coaxial nanowires for photovoltaic applications,* IEEE Electr. Device Lett. **32**, 45 (2011).

[103] I. Gryczynski, J. Malicka, Z. Gryczynski, and J. R. Lakowicz, *Radiative decay engineering 4. Experimental studies of surface plasmon-coupled directional emission,* Anal. Biochem. **324**, 170 (2004).

[104] F. B. Leloup, S. Forment, P. Dutré, M. R. Pointer, and P. Hanselaer, *Design of an instrument for measuring the spectral bidirectional scatter distribution function,* Appl. Opt. **47**, 5454 (2008).

[105] N. Yu, J. Fan, Q. J. Wang, C. Pflügl, L. Diehl, T. Edamura, M. Yamanishi, H. Kan, and F. Capasso, *Small-divergence semiconductor lasers by plasmonic collimation,* Nature Photon. **2**, 564 (2008).

[106] M. Yoshita, K. Koyama, M. Baba, and H. Akiyama, *Fourier imaging study of efficient near-field optical coupling in solid immersion fluorescence microscopy,* J. Appl. Phys. **92**, 862 (2002).

[107] J. Gómez Rivas, G. Vecchi, and V. Giannini, *Surface plasmon polariton-mediated enhancement of the emission of dye molecules on metallic gratings,* New J. Phys. **10**, 105007 (2008).

[108] J. Grandidier, S. Massenot, G. C. Des Francs, A. Bouhelier, J.-C. Weeber, L. Markey, A. Dereux, J. Renger, M. González, and R. Quidant, *Dielectric-loaded surface plasmon polariton waveguides: Figures of merit and mode characterization by image and Fourier plane leakage microscopy,* Phys. Rev. B **78**, 245419 (2008).

[109] A. G. Curto, G. Volpe, T. H. Taminiau, M. P. Kreuzer, R. Quidant, and N. F. van Hulst, *Unidirectional emission of a quantum dot coupled to a nanoantenna,* Science **329**, 930 (2010).

[110] T. Shegai, V. D. Miljkovic, K. Bao, H. Xu, P. Nordlander, P. Johansson, and M. Käll, *Unidirectional broadband light emission from supported plasmonic nanowires,* Nano Lett. **11**, 706 (2011).

[111] I. Seršić, C. Tuambilangana, and A. F. Koenderink, *Fourier microscopy of single plasmonic scatterers,* New J. Phys. **13**, 083019 (2011).

[112] E. C. Garnett, M. L. Brongersma, Y. Cui, and M. D. McGehee, *Nanowire solar cells,* Ann. Rev. Mater. Res. **41**, 269 (2011).

[113] J. Giblin, V. Protasenko, and M. Kuno, *Wavelength sensitivity of single nanowire excitation polarization anisotropies explained through a generalized treatment of their linear absorption,* ACS nano **3**, 1979 (2009).

[114] J. Giblin, M. Syed, M. T. Banning, M. Kuno, and G. Hartland, *Experimental determination of single CdSe nanowire absorption cross sections through photothermal imaging,* ACS nano **4**, 358 (2010).

[115] J. Giblin, F. Vietmeyer, M. P. McDonald, and M. Kuno, *Single Nanowire Extinction Spectroscopy,* Nano Lett. **11**, 3307 (2011).

[116] J. W. Goodman, *Introduction to Fourier optics,* McGraw-Hill, New York, 1996.

[117] L. Novotny and B. Hecht, *Principles of nano-optics,* Cambridge University Press, 2006.

[118] M. Born and E. Wolf, *Principles of optics,* Cambridge University Press, 6th edition, 1997.

[119] E. F. Schubert, *Light emitting diodes,* Cambridge University Press, 2nd edition, 2006.

[120] E. Hecht, *Optics,* Addison Wesley, 4th edition, 2002.

[121] F. J. García de Abajo, *Colloquium: Light scattering by particle and hole arrays,* Rev. Mod. Phys. **79**, 1267 (2007).

[122] G. Vecchi, V. Giannini, and J. Gómez Rivas, *Surface modes in plasmonic crystals induced by diffractive coupling of nanoantennas,* Phys. Rev. B **80**, 201401 (2009).

[123] G. Lozano, D. J. Louwers, S. R. K. Rodrigez, S. Murai, O. T. A. Janssen, M. A. Verschuuren, and J. Gómez Rivas, *Plasmonics for solid-state lighting: Enhanced and directional emission of highly efficient light sources,* Light: Sci. Appl. **2**, e66 (2013).

[124] S. Murai, M. Verschuuren, G. Lozano, G. Pirruccio, S. Rodriguez, and J. Gómez Rivas, *Hybrid plasmonic-photonic modes in diffractive arrays of nanoparticles coupled to light-emitting optical waveguides,* Opt. Express **21**, 4250 (2013).

[125] E. D. Minot, F. Kelkensberg, M. van Kouwen, J. A. van Dam, L. P. Kouwenhoven, V. Zwiller, M. T. Borgström, O. Wunnicke, M. A. Verheijen, and E. P. A. M. Bakkers, *Single quantum dot nanowire LEDs,* Nano Lett. **7**, 367 (2007).

[126] P. Fan, C. Colombo, K. C. Huang, P. Krogstrup, J. Nygård, A. Fontcuberta i Morral, and M. L. Brongersma, *An Electrically-Driven GaAs Nanowire Surface Plasmon Source,* Nano Lett. **12**, 4943 (2012).

[127] O. Muskens, J. Treffers, M. Forcales, M. Borgström, E. Bakkers, and J. Gómez Rivas, *Modification of the photoluminescence anisotropy of semiconductor nanowires by coupling to surface plasmon polaritons,* Opt. Lett. **32**, 2097 (2007).

[128] Y. R. Do, Y.-C. Kim, Y.-W. Song, and Y.-H. Lee, *Enhanced light extraction efficiency from organic light emitting diodes by insertion of a two-dimensional photonic crystal structure,* J. Appl. Phys. **96**, 7629 (2004).

[129] A. David, H. Benisty, and C. Weisbuch, *Optimization of light-diffracting photonic-crystals for high extraction efficiency LEDs,* J. Disp. Technol. **3**, 133 (2007).

[130] J. J. Wierer, A. David, and M. M. Megens, *III-nitride photonic-crystal light-emitting diodes with high extraction efficiency,* Nature Photon. **3**, 163 (2009).

[131] B. H. Husken, A. Koenderink, and W. Vos, *Angular redistribution of near-infrared emission from quantum dots in 3D photonic crystals,* J. Phys. Chem. C **117**, 3431 (2013).

[132] L. J. Lauhon, M. S. Gudiksen, D. Wang, and C. M. Lieber, *Epitaxial core-shell and core-multishell nanowire heterostructures,* Nature **420**, 57 (2002).

[133] M. H. Huang, S. Mao, H. Feick, H. Yan, Y. Wu, H. Kind, E. Weber, R. Russo, and P. Yang, *Room-temperature ultraviolet nanowire nanolasers,* Science **292**, 1897 (2001).

[134] H. E. Ruda and A. Shik, *Polarization-sensitive optical phenomena in thick semiconducting nanowires,* J. Appl. Phys. **100**, 024314 (2006).

[135] M. H. M. van Weert, N. Akopian, F. Kelkensberg, U. Perinetti, M. P. van Kouwen, J. Gómez Rivas, M. T. Borgström, R. E. Algra, M. A. Verheijen, and E. P. A. M. Bakkers, *Orientation-Dependent Optical-Polarization Properties of Single Quantum Dots in Nanowires,* Small **5**, 2134 (2009).

[136] T. M. Babinec, B. J. M. Hausmann, M. Khan, Y. Zhang, J. R. Maze, P. R. Hemmer, and M. Lončar, *A diamond nanowire single-photon source,* Nat. Nanotech. **5**, 195 (2010).

[137] A. V. Maslov, M. I. Bakunov, and C. Z. Ning, *Distribution of optical emission between guided modes and free space in a semiconductor nanowire,* J. Appl. Phys. **99**, 024314 (2006).

[138] P. Bharadwaj, B. Deutsch, and L. Novotny, *Optical Antennas,* Adv. Opt. Photon. **1**, 438 (2009).

[139] V. Giannini, A. I. Fernández-Domínguez, S. C. Heck, and S. A. Maier, *Plasmonic Nanoantennas: Fundamentals and Their Use in Controlling the Radiative Properties of Nanoemitters,* Chem. Rev. **111**, 3888 (2011).

[140] M. T. Borgström, J. Wallentin, J. Trägårdh, P. Ramvall, M. Ek, L. R. Wallenberg, L. Samuelson, and K. Deppert, *In situ etching for total control over axial and radial nanowire growth,* Nano Res. **3**, 264 (2010).

[141] M. Kira, F. Jahnke, and S. W. Koch, *Microscopic theory of excitonic signatures in semiconductor photoluminescence,* Phys. Rev. Lett. **81**, 3263 (1998).

[142] S. Ramo, J. Whinnery, and T. Van Duzer, *Fields and waves in communication electronics,* Wiley, New York, 1993.

[143] J. D. Joannopoulos, S. G. Johnson, J. N. Winn, and R. D. Meade, *Photonic crystals: molding the flow of light,* Princeton University Press, 2008.

[144] E. Yablonovitch, *Inhibited spontaneous emission in solid-state physics and electronics,* Phys. Rev. Lett. **58**, 2059 (1987).

[145] M. Leistikow, A. P. Mosk, E. Yeganegi, S. R. Huisman, A. Lagendijk, and W. L. Vos, *Inhibited spontaneous emission of quantum dots observed in a 3D photonic band gap,* Phys. Rev. Lett. **107**, 193903: 1 (2011).

[146] E. Chow, S. Lin, S. Johnson, P. Villeneuve, J. Joannopoulos, J. Wendt, G. Vawter, W. Zubrzycki, H. Hou, and A. Alleman, *Three-dimensional control of light in a two-dimensional photonic crystal slab,* Nature **407**, 983 (2000).

[147] K. Ishizaki and S. Noda, *Manipulation of photons at the surface of three-dimensional photonic crystals,* Nature **460**, 367 (2009).

[148] P. Lodahl, A. F. Van Driel, I. S. Nikolaev, A. Irman, K. Overgaag, D. Vanmaekelbergh, and W. L. Vos, *Controlling the dynamics of spontaneous emission from quantum dots by photonic crystals,* Nature **430**, 654 (2004).

[149] M. Fujita, S. Takahashi, Y. Tanaka, T. Asano, and S. Noda, *Simultaneous inhibition and redistribution of spontaneous light emission in photonic crystals,* Science **308**, 1296 (2005).

[150] Y. Akahane, T. Asano, B. Song, and S. Noda, *High-Q photonic nanocavity in a two-dimensional photonic crystal,* Nature **425**, 944 (2003).

[151] K. McGroddy, A. David, E. Matioli, M. Iza, S. Nakamura, S. DenBaars, J. Speck, C. Weisbuch, and E. Hu, *Directional emission control and increased light extraction in GaN photonic crystal light emitting diodes,* Appl. Phys. Lett. **93**, 103502 (2008).

[152] E. C. Nelson, N. L. Dias, K. P. Bassett, S. N. Dunham, V. Verma, M. Miyake, P. Wiltzius, J. A. Rogers, J. J. Coleman, and X. Li, *Epitaxial growth of three-dimensionally architectured optoelectronic devices,* Nature Mater. **10**, 676 (2011).

[153] O. L. Muskens, M. T. Borgström, E. P. A. M. Bakkers, and J. Gómez Rivas, *Giant optical birefringence in ensembles of semiconductor nanowires,* Appl. Phys. Lett. **89**, 233117 (2006).

[154] A. Mishra, L. V. Titova, T. B. Hoang, H. E. Jackson, L. M. Smith, J. M. Yarrison-Rice, Y. Kim, H. J. Joyce, Q. Gao, H. H. Tan, and C. Jagadish, *Polarization and temperature dependence of photoluminescence from zincblende and wurtzite InP nanowires,* Appl. Phys. Lett. **91**, 263104 (2007).

[155] R. E. Algra, M. A. Verheijen, M. T. Borgström, L. F. Feiner, G. Immink, W. J. P. van Enckevort, E. Vlieg, and E. P. A. M. Bakkers, *Twinning superlattices in indium phosphide nanowires,* Nature **456**, 369 (2008).

[156] T. Ba Hoang, A. F. Moses, L. Ahtapodov, H. Zhou, D. L. Dheeraj, A. T. J. van Helvoort, B.-O. Fimland, and H. Weman, *Engineering Parallel and Perpendicular Polarized Photoluminescence from a Single Semiconductor Nanowire by Crystal Phase Control,* Nano Lett. **10**, 2927 (2010).

[157] N. Akopian, G. Patriarche, L. Liu, J. C. Harmand, and V. Zwiller, *Crystal phase quantum dots,* Nano Lett. **10**, 1198 (2010).

[158] J. J. Wierer, M. R. Krames, J. E. Epler, N. F. Gardner, M. G. Craford, J. R. Wendt, J. A. Simmons, and M. M. Sigalas, *InGaN/GaN quantum-well heterostructure light-emitting diodes employing photonic crystal structures,* Appl. Phys. Lett. **84**, 3885 (2004).

[159] L. Rayleigh, *On the reflection of light from a regularly stratified medium,* Proc. R. Soc. A **93**, 565 (1917).

[160] W. M. Robertson, G. Arjavalingam, R. D. Meade, K. D. Brommer, A. M. Rappe, and J. D. Joannopoulos, *Measurement of photonic band structure in a two-dimensional periodic dielectric array,* Phys. Rev. Lett. **68**, 2023 (1992).

[161] E. Yablonovitch, T. J. Gmitter, and K. M. Leung, *Photonic band structure: The face-centered-cubic case employing nonspherical atoms,* Phys. Rev. Lett. **67**, 2295 (1991).

[162] S. Lin, J. G. Fleming, D. L. Hetherington, B. K. Smith, R. Biswas, K. M. Ho, M. M. Sigalas, W. Zubrzycki, S. R. Kurtz, and J. Bur, *A three-dimensional photonic crystal operating at infrared wavelengths,* Nature **394**, 251 (1998).

[163] S. G. Johnson and J. D. Joannopoulos, *Block-iterative frequency-domain methods for Maxwell's equations in a planewave basis,* Opt. Express **8**, 173 (2001).

[164] W. Wei, X.-Y. Bao, C. Soci, Y. Ding, Z.-L. Wang, and D. Wang, *Direct heteroepitaxy of vertical InAs nanowires on Si substrates for broad band photovoltaics and photodetection,* Nano Lett. **9**, 2926 (2009).

[165] C. Lin and M. L. Povinelli, *Optical absorption enhancement in silicon nanowire arrays with a large lattice constant for photovoltaic applications,* Opt. Express **17**, 19371 (2009).

[166] T. Mårtensson, P. Carlberg, M. Borgström, L. Montelius, W. Seifert, and L. Samuelson, *Nanowire arrays defined by nanoimprint lithography,* Nano Lett. **4**, 699 (2004).

[167] E. D. Palik and G. Ghosh, *Handbook of optical constants of solids,* volume 3, Academic Press, 1998.

[168] J. Wang, M. S. Gudiksen, X. Duan, Y. Cui, and C. M. Lieber, *Highly polarized photoluminescence and photodetection from single indium phosphide nanowires,* Science **293**, 1455 (2001).

[169] J. Gómez Rivas, O. L. Muskens, M. T. Borgström, S. L. Diedenhofen, and E. P. A. M. Bakkers, *One-Dimensional Nanostructures,* volume 3 of *Lecture Notes in Nanoscale Science and Technology,* chapter 6, pages 127–145, Springer, 2008.

[170] S. L. Diedenhofen, G. Vecchi, R. E. Algra, A. Hartsuiker, O. L. Muskens, G. Immink, E. P. A. M. Bakkers, W. L. Vos, and J. Gómez Rivas, *Broad-band and Omnidirectional Antireflection Coatings Based on Semiconductor Nanorods,* Adv. Mater. **21**, 973 (2009).

[171] J. Zhu, C. M. Hsu, Z. Yu, S. Fan, and Y. Cui, *Nanodome solar cells with efficient light management and self-cleaning,* Nano Lett. **10**, 1979 (2009).

[172] A. Chutinan and S. John, *Light trapping and absorption optimization in certain thin-film photonic crystal architectures,* Phys. Rev. A **78**, 023825 (2008).

[173] C. Lin and M. L. Povinelli, *Optical absorption enhancement in silicon nanowire arrays with a large lattice constant for photovoltaic applications,* Opt. Express **17**, 19371 (2009).

[174] G. Brönstrup, F. Garwe, A. Csáki, W. Fritzsche, A. Steinbrück, and S. Christiansen, *Statistical model on the optical properties of silicon nanowire mats,* Phys. Rev. B **84**, 125432 (2011).

[175] M. A. M. Versteegh, R. E. C. van der Wel, and J. I. Dijkhuis, *Measurement of light diffusion in ZnO nanowire forests*, Appl. Phys. Lett. **100**, 101108 (2012).

[176] A. Ishimaru, *Wave propagation and scattering in random media*, Academic Press, New York, 1978.

[177] P. Yeh, *Optical waves in layered media*, Wiley, New York, 1988.

[178] H. Davies, *The reflection of electromagnetic waves from a rough surface*, Proceedings of the IEE-Part IV: Institution Monographs **101**, 209 (1954).

[179] Z. P. Yang, L. Ci, A. James, S. Y. Lin, and P. M. Ajayan, *Experimental observation of an extremely dark material made by a low-density nanotube array*, Nano Lett. **8**, 446 (2008).

[180] O. Schenk and K. Gärtner, *Solving unsymmetric sparse systems of linear equations with PARDISO*, Fut. Gener. Comp. Syst. **20**, 475 (2004).

[181] O. Schenk and K. Gärtner, *On fast factorization pivoting methods for sparse symmetric indefinite systems*, Electron. Trans. Numer. Ana. **23**, 158 (2006).

SUMMARY

The ability to control the light-matter interaction is important for the optimization of novel energy- and material-efficient light-emitting and photovoltaic devices. The control over this interaction for visible and near-infrared light can be achieved by using structures with dimensions comparable to the optical wavelengths. Since these dimensions are of the order of tens of nanometers, the research took the name of nanophotonics. Semiconductor nanowires have become one of the most interesting nanostructures for nanophotonics. Ensembles of semiconductor nanowires have proven to be broadband and omnidirectional antireflection layers and efficient light absorbers in nanowire solar cells. Ordered arrays of nanowires made of a direct band gap semiconductor, such as indium phosphide (InP), have been also studied for achieving directional photoluminescence emission that could improve the performance of light-emitting diodes. Individual nanowires have been demonstrated as optical waveguides, nanolasers, polarization-dependent photodetectors and even single-photon sources. Despite the extensive research on the optical properties of nanowires, typically only the spectral and polarization responses of these strongly-anisotropic nanostructures are investigated, while the directional response is neglected. We believe that the understanding of the directional photonic properties of semiconductor nanowires will provide a useful knowledge to further improve novel nanowire-based photonic and optoelectronic devices. Therefore, this doctoral thesis discusses experiments and theory on the directional photonic properties, i.e., light emission, absorption and extinction, of individual semiconductor nanowires, as well as of their ensembles.

We introduce the research on photonic properties of semiconductor nanowires in Chapter 1 and present the vapor-liquid-solid nanowire-growth method used to fabricate the nanowires investigated in this thesis. This method makes use of a metallic particle to catalyze the vertical growth of nanowires on top of substrates. Chapter 1 also discusses different methods of controlling the diameter and spatial arrangement of the nanowires by defining the positions of the catalyst particles on a substrate prior to the growth.

Chapter 2 gives a description of the two most widely employed analytical formalisms describing the interaction of light with infinitely long isolated cylinders, to which

nanowires are commonly approximated. The first formalism is Mie theory, that quantifies the extinction, scattering and absorption efficiencies of cylinders upon a plane wave excitation. Using this theory we calculate the scattering and absorption efficiencies of an InP cylinder as a function of its diameter, the wavelength, polarization and the angle of the incident light. Besides being scatterers, infinitely long cylinders can also act as cavities that support optical eigenmodes. Such modes can be described using the second formalism: the waveguide theory. In a perfect case of a nonabsorbing cylinder, depending on its diameter and the wavelength of light, these eigenmodes can be bound to the cylinder or leak to free space. The bound modes can guide light coupled to them over large distances and, therefore, are called guided. The eigenmodes with short propagation lengths radiate into free space and are referred to as the leaky modes. Finally, we show the correspondence of the two theories to conclude that the Mie theory actually describes the coupling of a plane wave incident on a cylinder to its leaky modes. Mie and waveguide theories describe the spectral and directional properties of semiconductor nanowires.

Experimental studies of angle-dependent light emission and absorption in individual nanophotonic structures such as direct band gap semiconductor nanowires require the use of microscopy-based techniques. For investigating the directional photoluminescence of single nanowires we employ Fourier microscopy. This technique exploits the properties of lenses to decompose the light-wave into a superposition of plane waves described by unique wave vectors. Each of these plane waves can be associated to one direction of light propagation. The imaging of the back focal plane (BFP) of an objective lens onto a CCD camera results in intensity maps of the directional emission. Chapter 3 discusses the theoretical principles and the experimental details of this technique. The optical path of light in our Fourier microscope can be time-reversed, i.e., instead of imaging the BFP of an objective lens, we can create a point source of light in the BFP and let this light propagate through the lens. This results in a plane wave illumination of a sample placed under the objective lens. The angle of incidence of the incident plane wave is determined by the position of the point source in the BFP. The implementation of this concept into our Fourier microscope setup resulted in obtaining a novel, unique scientific tool for studying the directional light absorption in nanostructures. We conclude Chapter 3 with the description of applications stimulated by the development of the Fourier and time-reversed Fourier microscopy in our group.

In Chapter 4 we show the first measurements of the directional light emission of individual semiconductor nanowires by employing Fourier microscopy. With the help of this method we find that individual InP nanowires are directional light emitters. This behavior is explained by means of coupling of the emission to leaky modes supported by the cylindrical geometry of nanowires. The conservation of parallel momentum of the mode at the nanowire interface provides directional emission into the free space.

Using Fourier microscopy we show in Chapter 5 that ordered arrays of InP nanowires have the properties of two dimensional photonic crystals. Such crystals support Bloch modes originating from the interference of light scattered in a medium with a refractive index that is modulated periodically in two dimensions in space. The photonic properties of the photonic crystals depend on both, the geometry of the lattice and on the refractive index contrast between the constituents of the crystal. Light emitted by the nanowires forming the photonic crystal can couple to Bloch modes. Due to the finite length of the nanowires, these modes can leak to free space in certain directions. In this chapter we also demonstrate that the directional emission of nanowire photonic crystals can be controlled by modifying the refractive index of the medium that surrounds the nanowires.

Nanowires have attracted the interest of photovoltaic research due to their efficient light absorption. Although the optical absorption in individual nanowires has been widely discussed, it has never been demonstrated experimentally as a function of the angle of incidence of the light. By using the time-reversed Fourier microscope, we illuminated individual InP nanowires with a controlled angle of incidence under a microscope objective. Measurements of the photoluminescence intensity emitted by the nanowires excited with different angles of incidence are presented in Chapter 6, where it is demonstrated the directional absorption in individual nanowires. We find that Mie theory can be only applied for large angles of incidence with respect to the nanowire axis. For small angles, the absorption in nanowires is larger than the predictions of Mie theory. We argue that this behavior originates from the finite length of the nanowires that support guided modes. Light incident along the axis of finite nanowires can couple to these guided modes at the end facet and increase the absorption.

Photovoltaic devices based on nanowires will consist of ordered or random ensembles. The description of light propagation in such ensembles will allow to optimize the performance of nanowire solar cells. Light propagation in ordered arrays of nanowires is usually described by calculating the eigenmodes of periodic structures or by numerical simulations, while random ensembles of very thin nanowires are often described by effective medium theories assuming their dipolar optical response. In Chapter 7 we demonstrate wavelength, angle and polarization-dependent light extinction in random ensembles of semiconductor nanowires with diameters comparable to the wavelength. This light extinction is successfully described by the properties of individual nanowires that form a Mie scattering effective medium in the independent scattering approximation. In this way we provide a relatively simple analytical formalism to describe the extinction properties of random ensembles of polydisperse nanowires beyond the dipolar approximation.

SAMENVATTING IN HET NEDERLANDS

De mogelijkheid tot het beheersen van licht-materie interacties is belangrijk voor het optimaliseren van nieuwe energie- en materiaalefficiënte licht uitzendende en fotovoltad'sche apparaten. De controle over deze interacties, voor zichtbaar en nabij-infrarood licht, kan worden afgedwongen door het gebruik van structuren met afmetingen in de ordegrootte van zichtbare golflengtes. Aangezien deze afmetingen van de orde van tientallen nanometers zijn, kreeg het onderzoek hiernaar de naam 'nanofotonica'. Halfgeleider nanodraden worden gerekend tot de meest interessante nanostructuren voor nanofotonica. Er is aangetoond dat ensembles van halfgeleider nanodraden een sterk verminderde reflectie hebben voor een breed hoek- en golflengtebereik en tevens efficiënt licht absorberen in nanodraad zonnecellen. Geordend gerangschikte nanodraden gemaakt van een halfgeleider met directe bandkloof, zoals indiumfosfide (InP), zijn ook onderzocht voor het bereiden van hoekafhankelijke fotoluminescentie-emissie, dat de prestaties van licht uitzendende diodes (LEDs) kan verbeteren. Individuele nanodraden als optische golfgeleiders, nanolasers, polarisatie-afhankelijke lichtdetectors en zelfs éénfotonbronnen zijn aangetoond. Hoewel er uitgebreid onderzoek is verricht naar optische eigenschappen van nanodraden, is eigenaardig genoeg slechts het spectrale en polarisatie-afhankelijke gedrag van deze sterk-anisotropische nanostructuren onderzocht, terwijl het hoekafhankelijke gedrag tot op heden is genegeerd. Wij zijn van mening dat het begrijpen van de hoekafhankelijke lichteigenschappen van halfgeleider nanodraden een nuttige kennis zal verschaffen voor het verder verbeteren van nieuwe fotonische en opto-elektronische apparaten gebaseerd op nanodraden. Daarom behandelt deze doctoraalscriptie experimenten en theorie over de hoekafhankelijke lichteigenschappen - ofwel lichtemissie, -absorptie en -extinctie - van individuele halfgeleider nanodraden, en tevens van ensembles ervan.

We introduceren het onderzoek naar lichteigenschappen van halfgeleider nanodraden in Hoofdstuk 1, en presenteren de gas-vloeistof-vastestof-groeimethode, die wordt gebruikt in de nanodraden die in deze scriptie worden onderzocht. Deze methode maakt gebruik van een metaaldeeltje om de verticale groei van nanodraden op substraten te katalyseren. Hoofdstuk 1 behandelt tevens verschillende methoden voor het beheersen van de diameter en de ordening van de nanodraden door het bepalen van de posities van het katalysedeeltje op het substraat, alvorens de nanodraden te groeien.

Hoofdstuk 2 beschrijft de twee meest algemeen gebruikte analytische methoden die de interactie beschrijven tussen licht en oneindig lange ged'soleerde cilinders, die normaliter worden gebruikt als model voor nanodraden. De eerste methode is Mietheorie, waarmee de extinctie-, verstrooiing- en absorptie-efficiënties van cilinders die beschenen worden met een vlakke golf kunnen worden berekend. Gebruikmakend van deze theorie berekenen we de verstrooiing- en absorptie-efficiënties van een InP cilinder als functie van zijn diameter en de golflengte, polarisatie en invalshoek van het inkomende licht. Oneindig lange cilinders kunnen zich, naast verstrooiiers, ook gedragen als 'holtes' die optische eigenmodes kunnen dragen. Zulke modes kunnen worden beschreven door het gebruik van de tweede methode: de golfgeleidertheorie. In het perfecte geval van een niet-absorberende cilinder, afhankelijk van zijn diameter en de golflengte van het licht, kunnen deze eigenmodes worden gebonden aan de cilinder óf weglekken naar de omgeving. De gebonden modes kunnen licht dat aan de cilinders gebonden is over lange afstanden doen voortplanten, en worden dan ook 'geleide modes' genoemd. De eigenmodes met korte voortplantingslengtes zenden licht uit in de omgeving en worden 'lekkende modes' genoemd. Tot slot laten we de overenkomsten tussen beide theorieën zien om te concluderen dat Mietheorie uiteindelijk de koppeling van een vlakke golf met de lekkende modes van een cilinder beschrijft. Mie- en golfgeleidertheorieën beschrijven dus de golflengte- en hoekafhankelijke eigenschappen van halfgeleider nanodraden.

Experimenteel onderzoek naar hoekafhankelijke lichtuitzending en -absorptie in individuele nanofotonische structuren, zoals directe-bandkloof halfgeleider nanodraden, vereist het gebruik van technieken die op microscopie gebaseerd zijn. Voor het onderzoeken van de hoekafhankelijke fotoluminescentie van enkele nanodraden gebruiken we Fouriermicroscopie. Deze techniek maakt gebruik van de eigenschappen van lenzen om een lichtgolf onder te verdelen in een superpositie van vlakke golven die worden beschreven door unieke golfvectoren. Elk van deze vlakke golven kan één-op-één worden gerelateerd aan een enkele hoek van lichtvoortplanting. De afbeelding van het brandpuntsvlak aan de beeldzijde van het objectief (BPV) op een CCD-camera resulteert in intensiteitsprofielen van de hoekafhankelijke lichtuitzending. Hoofdstuk 3 beschrijft de theoretische principes en de experimentele details van deze techniek. Het optische pad van licht in onze Fouriermicroscoop kan worden omgekeerd; dus in plaats van het afbeelden van het BPV van het objectief, creëren we een puntbron van licht in het BPV en leiden dit licht door het objectief. Dit resulteert in een vlakkegolfverlichting van een object dat onder het objectief is geplaatst. De hoek van inval van de vlakke golf wordt bepaald door de positie van de puntbron in het BPV. Het implementeren van dit concept in onze Fouriermicroscoop heeft geresulteerd in een nieuw, uniek wetenschappelijk apparaat waarmee de hoekafhankelijke lichtabsorptie in nanostructuren kan worden onderzocht. We sluiten Hoofdstuk 3 af met het beschrijven van toepassingen die mogelijk zijn geworden door de ontwikkeling van de Fouriermicroscoop en tijdsomgekeerde

Fouriermicroscopie in onze groep.

In Hoofdstuk 4 laten we de eerste metingen zien van hoekafhankelijke lichtuitzending van individuele halfgeleider nanodraden door het gebruik van Fouriermicroscopie. Met behulp van deze methode constateren we dat individuele InP nanodraden gerichte lichtuitzenders zijn. Dit gedrag kan worden verklaard door de koppeling van de lichtemissie aan lekkende modes die voortkomen uit de cilindrische vorm van de nanodraden. Het behoud van parallelle impuls van de mode op het nanodraadoppervlak zorgt voor gerichte lichtuitzending naar de omgeving.

Gebruikmakend van Fouriermicroscopie laten we in Hoofdstuk 5 zien dat geordend gerangschikte InP nanodraden de eigenschappen hebben van tweedimensionale fotonische kristallen. In zulke kristallen komen Blochmodes voor, die hun oorsprong hebben in interferentie van licht dat is verstrooid in een medium waarvan de brekingsindex periodiek verandert in twee ruimtelijke dimensies. De fotonische eigenschappen van de fotonische kristallen zijn afhankelijk van zowel de geometrie van het patroon als het contrast in brekingsindex tussen de materialen in het kristal. Licht dat is uitgezonden door de nanodraden in het fotonisch kristal, kan koppelen aan Blochmodes. Vanwege de eindige lengte van de nanodraden kunnen deze modes weglekken naar de omgeving in bepaalde richtingen. In dit hoofdstuk laten we ook zien dat de hoekafhankelijke lichtuitzending van de nanodraad fotonische kristallen kan worden gemanipuleerd door het aanpassen van de brekingsindex van het medium dat de nanodraden omgeeft.

Nanodraden zijn interessant voor zonnecelonderzoek door hun efficiënte lichtabsorptie. Hoewel de optische absorptie in individuele nanodraden uitgebreid bediscussieerd is, is het nooit experimenteel bestudeerd als functie van de invalshoek van het licht. Gebruikmakend van de tijdsomgekeerde Fouriermicroscoop beschijnen we individuele InP nanodraden vanuit een bepaalde invalshoek onder een microscoopobjectief. Intensiteitsmetingen van de fotoluminescentie die wordt uitgezonden door de nanodraden die vanuit verschillende invalshoeken worden geëxciteerd, worden gepresenteerd in Hoofdstuk 6, waar de hoekafhankelijke absorptie in individuele nanodraden is aangetoond. We ondervinden dat Mietheorie alleen kan worden toegepast voor grote hoeken van inval ten opzichte van de nanodraadas. Voor kleine hoeken van inval is de absorptie hoger dan is voorspeld door Mietheorie. Wij betogen dat dit gedrag komt door de eindige lengte van de nanodraden die geleide modes kunnen bevatten. Licht dat inkomt langs de as van de eindige nanodraden kan koppelen aan deze geleide modes op het eindfacet van de nanodraad en daardoor de absorptie vergroten.

Fotovoltaïsche apparaten gebaseerd op nanodraden zullen bestaan uit geordend of willekeurig gerangschikte ensembles. De beschrijving van lichtvoortplanting in zulke ensembles maakt het mogelijk om de prestaties van nanodraadzonnecellen te optimaliseren. Lichtvoortplanting in geordend gerangschikte nanodraden wordt typisch beschreven door het berekenen van eigenmodes van periodieke structuren of door numerieke simulaties, terwijl willekeurige ensembles van heel dunne nanodraden vaak worden beschreven door effectiefmediumtheorieën , gebruikmakend van het feit dat ze zich gedragen als een optische dipool. In Hoofdstuk 7 demonstreren we golflengte-, hoek- en polarisatieafhankelijke lichtextinctie in willekeurige ensembles van halfgeleider nanodraden met diameters van de ordegrootte van de golflengte. Deze lichtextinctie wordt succesvol beschreven door de eigenschappen van individuele nanodraden die een Mieverstrooiing effectief medium vormen, in de benadering van onafhankelijke verstrooiing. Op deze manier verschaffen we een relatief simpele analytische methode om de extinctie-eigenschappen te berekenen van willekeurige ensembles van polydisperse nanodraden, zelfs voorbij de dipolaire benadering.

PODSUMOWANIE

Światło jest nieodłącznym elementem wszechświata. Dzięki niemu możemy obserwować świat, komunikować się, wytwarzać energie elektryczną, czy produkować pożywienie. Dlatego nieustannie uczymy się jak wytwarzać, kontrolować, wykrywać i analizować światło. W tych celach używamy materiałów charakteryzujących się właściwościami takimi jak zdolność do transmisji, odbicia, emisji i absorpcji światła. Przykładowo, w oknach używa się materiałów, które dobrze transmitują światło, a w lustrach materiałów, które skutecznie odbijają światło. Właściwości te zależą nie tylko od składu chemicznego materiału, ale również od rozmiaru i kształtu struktur z niego wykonanych. Niektóre struktury potrafią być wydajnymi źródłami światła, a inne mogą pochłaniać (absorbować) światło i przekształcać je w energię elektryczną, przez co mogą służyć jako detektory optyczne lub ogniwa słoneczne. Kiedy zmniejszymy struktury do rozmiarów setek lub tysięcy razy mniejszych niż grubość ludzkiego włosa, właściwości optyczne takich struktur zmienią się dramatycznie. Zmiana ta spowodowana jest silniejszym oddziaływaniem struktury ze światłem dzięki temu, że rozmiary struktury stają się podobne do wielkości, jaką opisujemy światło, czyli długości fali mającej związek z kolorem światła. Takie oddziaływanie możemy podziwiać na co dzień patrząc w niebo, gdyż to właśnie dzięki swojemu rozmiarowi cząsteczki powietrza rozpraszają światło niebieskie nadając niebu tę właśnie barwę. Dzięki rozwojowi nanotechnologii możemy wytwarzać dotychczas niedostępne struktury o całkowicie nowych, niezbadanych właściwościach optycznych. Przykładem takich struktur są półprzewodnikowe nanodruty, których optyczne właściwości są tematem tej rozprawy doktorskiej.

Nanodruty to struktury w kształcie cylindrów, których wysokość jest wielokrotnie większa niż ich średnica, przy czym średnica nanodrutów zwykle zawiera się w przedziale od kilku do kilkuset nanometrów. Nanodruty przedstawione w tej pracy wykonane są z półprzewodników, czyli z materiałów, których przewodność elektryczna jest zwykle wyższa od przewodności izolatorów, lecz niższa od przewodności metali. Niektóre półprzewodniki mogą też pochłaniać światło widzialne i emitować światło o innej długości fali. W ostatnim dziesięcioleciu badania dowiodły, że nanodruty mogą służyć jako powłoki antyodbiciowe usprawniające transmisję światła dla szerokiego zakresu długości fal i kątów padania światła, lub mogą bardzo wydajnie pochłaniać światło.

Regularnie uszeregowane nanodruty okazały się emitować światło w specyficznych kierunkach, co jest interesujące dla usprawnienia codziennych źródeł światła, takich jak diody świecące. Pojedyncze nanodruty mogą działać jak światłowody, nanolasery, detektory optyczne, czy źródła pojedynczych fotonów, czyli cząstek światła. Dzięki swoim nowo odkrytym właściwościom optycznym nanodruty są interesujące dla ogniw słonecznych nowej generacji, w przypadku których bardzo ważna jest wydajna absorpcja światła, czy dla rozwoju nowych źródeł światła dla przyszłych komputerów kwantowych. Dotychczas większość odkryć w sferze optycznych właściwości nanodrutów skupiała się głównie na długości fali i polaryzacji światła z nimi oddziałującego. Zależność właściwości optycznych nanodrutów od kąta, pod jakim pada na nie światło nie była jak dotąd szeroko badana doświadczalnie, podobnie jak wpływ struktury nanodrutów na kierunkowość emitowanego przez nie światła. Poznanie i zrozumienie kierunkowych optycznych właściwości nanodrutów pozwoli na projektowanie sprawniejszych urządzeń optoelektronicznych wykorzystujących emitujące lub pochłaniające światło nanodruty. Prace opisane tej rozprawie doktorskiej skupiają się właśnie na badaniu kierunkowych właściwościach optycznych pojedynczych nanodrutów, jak również struktur zbudowanych z wielu nanodrutów.

Rozdział pierwszy zawiera krótki opis historii nanodrutów z podsumowaniem najważniejszych odkryć w dziedzinie ich właściwości optycznych. Przedstawiamy również metodę wytwarzania nanodrutów użytych w naszych badaniach.

Rozdział drugi przedstawia dwa podstawowe opisy teoretyczne optycznych właściwości nieskończenie długich cylindrów, do których przybliżane są nanodruty. Pierwszym z nich jest rozpraszanie Mie, które pozwala opisać ilościowo transmisję, rozpraszanie i absorpcję wiązki światła padającego na cylinder. Drugi formalizm teoretyczny opisuje nieskończenie długie cylindry jako światłowody, które charakteryzują się posiadaniem specyficznych dozwolonych stanów (modów), w których światło może się rozprzestrzeniać wzdłuż cylindra. Zależnie od współczynnika załamania światła materiału budującego cylinder, średnicy cylindra i długości fali światła, mody, w których podróżuje światło mogą być silnie związane z cylindrem lub stratne, które "wyciekają"do środowiska otaczającego cylinder. Mody związane mogą przesyłać (wodzić) światło na duże odległości i są podstawą działania światłowodów używanych w telekomunikacji. Mody stratne tracą natomiast energię w miarę rozprzestrzeniania się wzdłuż cylindra. Energia ta jest promieniowana na zewnątrz cylindra i owocuje emisją światła w konkretnych kierunkach. Ostatnia część rozdziału opisuje związek pomiędzy rozpraszaniem Mie i teorią światłowodów.

Doświadczalne badanie kierunkowej emisji i absorpcji światła w pojedynczych nanostrukturach, takich jak nanodruty, wymaga użycia technik mikroskopowych. Do pomiarów kierunkowej emisji światła z pojedynczych nanodrutów użyliśmy mikroskopu Fourierowskiego. Technika ta wykorzystuje właściwości optyczne soczewek skupiających, takich jak obiektyw mikroskopu. Światło docierające do soczewki z wielu kierunków na raz jest przez nią rozkładane na zbiór niezależnych kierunków rozprzestrzeniania się światła. W wyniku tego, światło docierające do soczewki z konkretnego kierunku jest przez nią skupiane w konkretnym miejscu w płaszczyźnie ogniskowej soczewki. W przypadku światła docierającego do soczewki z kierunku równoległego do jej osi optycznej, światło to zostanie skupione dokładnie w ognisku soczewki. Natomiast światło pochodzące z innych kierunków, skupiane będzie w różnych miejscach w płaszczyźnie ogniskowej soczewki tworząc w tej płaszczyźnie obraz kierunkowej emisji światła. Płaszczyzna ta jest następnie obrazowana przy użyciu cyfrowej kamery, dzięki czemu otrzymujemy obrazy kierunkowej emisji światła z badanej próbki. Teoretyczne podstawy tej techniki i szczegóły doświadczeń omawiane są w rozdziale trzecim. Badanie kierunkowej absorpcji światła w pojedynczych nanodrutach jest trudne do zrealizowania ze względu na ich rozmiary. Standardowe techniki stosowane w optyce używają wiązek laserowych o średnicach rzędu milimetrów i detektorów odległych od próbki o dziesiątki centymetrów. Wyizolowanie sygnału optycznego pochodzącego od pojedynczych nanostruktur badanych przy użyciu takich technik jest niemalże niemożliwe. Aby dokonać pomiaru kierunkowej absorpcji światła przez pojedyncze nanodruty, stworzyliśmy nową technikę doświadczalną opartą na mikroskopii Fourierowskiej. Kierunek, w jakim światło podróżuje w mikroskopie Fourierowskim może zostać odwrócony. Znaczy to, że zamiast obrazować płaszczyznę ogniskową obiektywu (jak w przypadku pomiaru kierunkowej emisji) możemy umieścić w tej płaszczyźnie punktowe źródło światła poprzez skupienie wiązki lasera. Światło rozchodzące się z jednego punktu w płaszczyźnie ogniskowej soczewki będzie podróżować w jednym kierunku po transmisji przez soczewkę. Kierunek rozchodzenia się światła za soczewką zależy od umiejscowienia punktowego źródła światła w płaszczyźnie ogniskowej soczewki. Dzięki temu, przy użyciu soczewki jaką jest obiektyw mikroskopu możemy oświetlać pojedyncze nanodruty pod żądanymi kątami. Wprowadzenie mikroskopii Fourierowskiego oświetlenia w życie zaowocowało uzyskaniem unikalnego zestawu doświadczalnego do pomiaru kierunkowej absorpcji światła w pojedynczych nanostrukturach. Rozdział trzeci zamykają propozycje badań zainspirowanych przez rozwój wyżej wymienionych technik pomiarowych w naszej grupie badawczej.

W rozdziale czwartym demonstrujemy pierwsze pomiary kierunkowej emisji światła z pojedynczych nanodrutów półprzewodnikowych przeprowadzone przy użyciu mikroskopu Fourierowskiego. Dzięki zastosowaniu tej techniki pomiarowej odkryliśmy, że pojedyncze nanodruty są nanoantenami emitującymi więcej światła w konkretnym kierunku. Kierunkowa emisja nanodrutów okazała się zupełnie inna, niż emisja tego samego półprzewodnika w postaci płaskiej jednorodnej warstwy. Emisja ta jest wynikiem obecności stratnych modów cylindra (opisanych w rozdziale drugim), które przechwytują światło emitowane wewnątrz nanodrutów. Światło w postaci modów stratnych "wycieka"przez powierzchnię nanodruta do jego otoczenia, co w konsekwencji prowadzi do emisji światła w konkretnych kierunkach.

Mikroskopia Fourierowska została przez nas zastosowana również w rozdziale piątym do pomiaru kierunkowej emisji uporządkowanych zespołów nanodrutów. Dzięki temu możemy zademonstrować, że uporządkowane struktury złożone z nanodrutów przejawiają właściwości kryształów fotonicznych. Kryształy fotoniczne to struktury złożone z materiałów o różnych współczynnikach załamania światła uporządkowanych okresowo w przestrzeni. Odległość pomiędzy obiektami o takim samym współczynniku załamania jest w takich strukturach porównywalna z długością fali światła, jakie ma się w nich rozchodzić. Uporządkowanie materiałów wymusza istnienie uporządkowanych stanów, w postaci których światło może się rozprzestrzeniać w krysztale fotonicznym (modów). Mody mogą istnieć dla różnych długości fali w zależności od wielkości obiektów budujących kryształ, odległości pomiędzy nimi, ich uporządkowania i różnicy współczynników załamania materiałów w krysztale. W przypadku nanodrutów otoczonych przez powietrze, emitowane przez nie światło może być częściowo przechwycone przez mody kryształu fotonicznego. Mody te mogą wydostać się na zewnątrz kryształu, co w konsekwencji prowadzi do emisji światła w konkretnych kierunkach uwidocznionych w eksperymencie. Kierunkowość emisji może być kontrolowana poprzez zmianę współczynnika załamania ośrodka, w którym znajdują sie nanodruty. Udało nam się to zademonstrować poprzez pomiar kierunkowej emisji nanodrutów zanurzonych w płynie o współczynniku załamania światła wyższym niż w powietrzu.

Nanodruty wzbudziły zainteresowanie badań nad ogniwami słonecznymi dzięki wydajnej absorpcji światła. Jednak pomimo wielu badań dotyczących absorpcji światła przez pojedyncze nanodruty, zależność absorpcji od kąta padania światła na nanodrut nie była badana doświadczalnie. Dzięki mikroskopii Fourierowskiego oświetlenia, mogliśmy kontrolować kąt oświetlenia pojedynczych półprzewodnikowych nanodrutów umieszczonych pod obiektywem mikroskopu. Rozdział szósty przedstawia pomiar kierunkowej absorpcji światła w pojedynczych nanodrutach przy użyciu tej metody. Aby zmierzyć kierunkową absorpcję dokonywany jest pomiar intensywności światła emitowanego przez nanodruty w zależności od kąta, pod jakim pada na nie światło wzbudzające tę emisję, gdyż intensywność emisji światła z nanodrutów jest wprost proporcjonalna do intensywności światła w nich absorbowanego. Wyniki doświadczeń zostały przez nas porównane z przewidywaniami teorii Mie dla nanodrutów o badanych średnicach i dla użytej długości fali światła wzbudzającego nanodruty. Przewidywania te zgadzały się z doświadczeniem tylko dla dużych kątów oświetlenia nanodrutów. Kiedy nanodruty były oświetlane z kierunku równoległego do swoich osi głównych, absorpcja światła była znacznie większa niż przewidywania teorii Mie. Okazało się, że w tym przypadku światło może zostać przechwycone przez mody związane w nanodrucie (rozdział drugi), co owocuje niespodziewanie wydajną absorpcją.

Ogniwa słoneczne wykorzystujące absorpcję światła w nanodrutach będą musiały składać się nie z pojedynczych nanodrutów, a z ich zespołów. Opis rozprzestrzeniania się światła w zespołach nanodrutów pozwoli więc na usprawnienie takich ogniw słonecznych. Rozprzestrzenianie się światła w uporządkowanych zespołach nanodrutów jest zwykle opisywane poprzez mody kryształów fotonicznych (podobnie jak w rozdziale 5), lub przez wymagające symulacje numeryczne. Nieuporządkowane zespoły nanodrutów są zwykle przybliżane jako jednorodny materiał o efektywnym współczynniku załamania światła, który sprawdza się tylko w przypadku najcieńszych nanodrutów. W rozdziale siódmym wyprowadzamy efektywny współczynnik załamania dla warstwy nieuporządkowanych nanodrutów o dużym zróżnicowaniu ich średnic. Transmisja wiązki światła przez taką warstwę nanodrutów przewidziana przez nasz model teoretyczny bardzo dobrze zgadza się z wynikami naszych doświadczeń. W ten sposób uzyskaliśmy względnie proste narzędzie teoretyczne pozwalające opisać transmisję wiązki światła przez nieuporządkowane zespoły nanodrutów o różnych średnicach.

LIST OF PUBLICATIONS

This thesis is based on the following publications:

1. *The role of leaky modes and Mie resonances in the absorption of semiconducting nanowires*, Ramón Paniagua-Domínguez, Grzegorz Grzela, Jaime Gómez Rivas and José Sánchez-Gil, in preparation. **(Chapter 2)**

2. *Receiving antennas for enhanced absorption: time-reversed Fourier microscope*, Tommy Barten, Gabriel Lozano, Grzegorz Grzela and Jaime Gómez Rivas, in preparation. **(Chapter 3.5.2)**

3. *Nanowire antenna emission*, Grzegorz Grzela, Ramón Paniagua-Domínguez, Tommy Barten, Yannik Fontana, José Sánchez-Gil and Jaime Gómez Rivas, Nano Lett. **12**, 5481 (2012). **(Chapter 4)**

4. *Mapping the directional emission of quasi-two-dimensional photonic crystals of semiconductor nanowires using Fourier microscopy*, Yannik Fontana, Grzegorz Grzela[1], Erik P. A. M. Bakkers and Jaime Gómez Rivas, Phys. Rev. B **86**, 245303 (2012). **(Chapter 5)**

5. *From Mie resonances to guided-mode absorption in individual semiconductor nanowires: angle-dependent absorption of individual nanowires measured with time-reversed Fourier microscopy*, Grzegorz Grzela, Ramón Paniagua-Domínguez, Tommy Barten, José Sánchez-Gil and Jaime Gómez Rivas, in preparation. **(Chapter 6)**

6. *Polarization-dependent light extinction in ensembles of polydisperse vertical semiconductor nanowires: A Mie scattering effective medium*, Grzegorz Grzela, Djamila Hourlier and Jaime Gómez Rivas, Phys. Rev. B **86**, 045305 (2012). **(Chapter 7)**

---

[1] Corresponding author

Other publications by the author:

1. *Enhanced and directional emission of semiconductor nanowires tailored through leaky/guided modes*, Ramón Paniagua-Domínguez, Grzegorz Grzela, Jaime Gómez Rivas and José Sánchez-Gil, submitted.
2. *Strong geometrical dependence of the absorption of light in arrays of semiconductor nanowires*, Silke L. Diedenhofen, Olaf T. A. Janssen, Grzegorz Grzela, Erik P. A. M. Bakkers, Jaime Gómez Rivas, ACS Nano **5**, 2316 (2011).
3. *Broadband and omnidirectional anti-reflection layer for III/V multi-junction solar cells*, Silke L. Diedenhofen, Grzegorz Grzela, Erik Haverkamp, Gerard Bauhuis, John Schermer and Jaime Gómez Rivas, Sol. Energ. Mat. Sol. Cells **101**, 308 (2012).

ACKNOWLEDGMENTS

Although a PhD project is typically a very individual undertaking, it is impossible to accomplish it only on your own. Four years of PhD is a long time that consists of moments of hard work, satisfaction, disappointment and fun. Besides everything I learnt during my PhD, I am very grateful for the people I met. These people have been always very open and helpful providing me with scientific advice, opening my eyes or giving me some good laughs. Here, I would like to thank them for their contributions to what I have become.

The PhD supervisor is typically the one who has the strongest impact on your scientific life. In my case this person was Jaime Gómez Rivas. Jaime, you taught me a lot, not only about Physics, but also about science in general. At the beginning you used to say: 'Optics is easy, because you can see your experiments'. In the end, I must say that optics is not that easy, but thanks to you, a person without any background in optics could find himself in the lab. Additionally, it was interesting to do the fundamental research while working in the applied environment of Philips Research in Eindhoven. Thank you for the opportunity to do my PhD with you and for your help and patience during very numerous iterative processes that have lead to the completion of this thesis.

I would like to thank Albert Polman for becoming my second promotor. I have always been amazed by the very supportive and constructive way in which you gave your criticism as well as by your optimism and calm. I am also grateful to the group leaders of the Center for Nanophotonics, Femius Koenderink and Ad Lagendijk for the tips on theory and Kobus Kuipers for a very positive criticism during the poster sessions and the nanophotonics colloquia.

The first steps in the new lab might be clumsy if you have never worked in similar topics before. Luckily, there was Silke Diedenhofen who helped me to start my work with nanowires in an optical lab and from whom I inherited the rotation stage setup. Silke, it was great to work with you, thanks a lot! I can not forget about Yichen Zhang, who was always ready to share his experience with confocal microscopy.

Although I have not worked at any university during my PhD, I had also a chance to supervise two master students, Yannik Fontana and Tommy Barten. I must say that I felt very good having a small nanowire team. Yannik, I think only me and you really know how much time and effort was to set up the Fourier imaging for measurements shown in Chapter 5, while Fourier microscopy was still new to both of us. Thanks for that! Tommy, the time-reversed Fourier would be a nightmare without your help and Chapter 6 would not exist. Guys, thanks for the great fun in the lab and your hard work that gave the content also to Chapter 3. I learnt a lot with you.

For the past years I have mostly specialized in experiments rather than in theory. Fortunately, Ramón Paniagua-Domínguez and José Sánchez-Gil helped me a lot with the theoretical description of the light-nanowire interaction. I learnt a lot during our collaboration and thanks to you I could also do some calculations on my own. Without you Chapters 2 and 4 would not have existed in the present form.

The experimental work would be impossible if there were no samples to measure. This thesis is dominated by the InP nanowires that were excellent for directional emission and absorption measurements. I would like to thank Moïra Hocevar, Tilman Zehender and Erik Bakkers without whom these samples (and the corresponding chapters of the thesis) would have not existed.

This PhD thesis might seem a bit diverse in the covered topics. Besides the light emission and absorption we also worked on light extinction and scattering in Chapter 7. This chapter would not have appeared in this thesis without the help of Djamila Hourlier. Djamila, thank you for a nice collaboration and the silicon nanowires.

Working in the Philips Research environment was a worthwhile experience. I am happy I could see the applied research from the fundamental perspective during the Philips group meetings. Thanks to Hans van Sprang, the head of the Photonic Materials and Devices group for a nice working atmosphere and the willingness to help with any problem we encountered. Philips also would not be the same without the resourcefulness of Eugene Timmering in solving urgent challenges, experience of Hans Cillessen in solving lab issues, and discussions with Marc Verschuuren. Thank you.

During four years of work I was a part of several ’teams’. It was an excellent opportunity to meet really nice people with different experience and to discuss the scientific results and challenges. Naturally, the Surface Photonics group taught me a lot and my colleagues have been always supportive and glad to share their insights, discuss the problems or simply, to have a nice chat. Silke Diedenhofen, Gabriele Vecchi, Christophe Arnold (thanks for the good time in conferences), Yichen Zhang, Gabriel Lozano Barbero (long evenings at work were actually enjoyable when you accompanied the struggle, thanks for always a thoughtful advice on esthetic issues for the form is as important as the content), Martijn Schaafsma, Yannik Fontana, Tommy Barten, Giuseppe Pirruccio (the 2000-mile roadtrip we had in the US was great), Said Rahimzadeh Kalaleh Rodriguez, Audrey Berrier, Shunsuke Murai, Hemant Kumar Tyagi, Giorgos Georgiou, Arkabrata Bhattacharya, Tom

Steinbusch, Karsten Goede, thank you for all the discussions. I am happy I met you.

At the same time I was also a part of the Nanophotovoltaics team at AMOLF, in which we aimed to employ nanophotonics for photovoltaics. Claire van Lare, Pierpaolo Spinelli, Jorik van de Groep, I was always happy to have a nice chat and a scientific discussion with you. It was wonderful to share the experience of the work as we started at similar times at AMOLF. Claire, thanks for the practical lessons of the nanoimprint in the cleanroom.

Additionally, I could participate in the VLS meetings at the Eindhoven University of Technology. I must say I learnt a lot about the growth, structure and properties of nanowires and I am thankful for numerous discussions.

It is good to leave when you know that your work was meaningful and that there is someone to continue it. Luckily, Dick van Dam is such person. Dick, thanks for the discussions about nanowires and nice cooperation during the last year of my PhD and your help with the summary of this thesis in Dutch. I know that the Fourier microscope remains in good hands. I wish you lots of success with your PhD!

Many thanks to Toon Coenen, who helped me with the directional cathodoluminescence of nanowires. Ivana Seršić was always happy to share her experience with Fourier microscopy, thank you Ivana! I am glad that Daryl Beggs took away some doubts I had about the nanowire photonic crystals. I am also grateful to Patrick Johnson who was very kind to share his experience about light extinction in ensembles of nanoparticles.

The work would not be so pleasant if not my officemates thanks to whom I could enjoy a nice atmosphere and have quite a few interesting discussions and laughs. Because of the industrial partnership between AMOLF and Philips Research I had actually two offices, one at Philips and one at AMOLF. Thanks to Gabriele Vecchi, Silke Diedenhofen, Martijn Schaafsma (3 years in the same office was full of enjoyable time), Shunsuke Murai, Marius Ivan (you made me realize that Romanian and Polish are quite alike, thanks for the vit. D discussions!) and Giuseppe Pirruccio for sharing the office at Philips and to Yichen Zhang, Ramy El-Dardiry, Ernst Jan Vesseur, James Parsons, Paolo Scalia, Benjamin Brenny, Hugo Doeleman, Janika van Moergestel and Beniamino Sciacca for nice chats at our office at AMOLF.

If not for my Physics teacher, Jerzy Szymala, at the secondary school, I think I would not have become a physicist in the first place. I am very happy with the choice I made. This choice was further advocated by the supervisor of my student association at my university, Janusz Przesławski, who always helped me with good advice and made me think what and how to do next.

Life is definitely not only about Physics. I did not forget it thanks to my dear friends who provided me with moments of nice and essential distraction. But most of all, I would like to thank my parents, Lucyna and Paweł Grzela for their love and constant support no matter what I do. Mamo, Tato, dziękuję Wam za to, że zawsze pomagaliście mi podnieść się po każdym potknięciu i wspieraliście mnie bym nigdy nie poddawał się w dążeniu do celu...

Thank you.
Grzegorz

ABOUT THE AUTHOR

Grzegorz Grzela was born in 1984 in Legnica, Poland. After finishing the Stanisław Wyspiański 2nd Comprehensive Secondary School in Legnica in 2003 he studied Experimental Physics at the University of Wrocław in Poland. During his studies he founded the Association of Physics Students 'Migacz' and organized a National Conference for Associations of Physics Students in Wrocław in 2006. He was also a member of the European Physics Students Initiative (EPSI), that closely collaborated with the European Physics Education Network (EUPEN). In 2007 he participated in the Erasmus program and studied at the Umeå University in Sweden. After his return to Poland he worked on his master project at the Institute for Low Temperatures and Structural Research of the Polish Academy of Sciences under the supervision of prof. Vinh Hung Tran. For his performance in studies and extracurricular activities he was awarded with the scholarship of the Minister of Science and Higher Education. In May 2009 he started his PhD project in the Nanowire Photonics/Surface Photonics group of FOM Institute AMOLF in the Netherlands under the supervision of prof. Jaime Gómez Rivas.

In his free time Grzegorz enjoys listening to film scores, plays the guitar and the piano and he always looks forward to hiking and traveling.